

Quantum chemical investigations on the function of  
different metal atoms in transition metal catalyzed  
reactions

Zur Erlangung des akademischen Grades einer  
DOKTORIN DER NATURWISSENSCHAFTEN

(Dr. rer. nat)

von der KIT-Fakultät für Chemie und Biowissenschaften  
des Karlsruher Instituts für Technologie (KIT)

genehmigte

DISSERTATION

von

M.Sc. Elham Barani

1. Referentin: Prof. Dr. Karin Fink

2. Referent: Prof. Dr. Willem Klopper

Tag der mündlichen Prüfung: 16.12.2022

## Contents

ABSTRACT.....	4
ZUSAMMENFASSUNG .....	5
1 INTRODUCTION .....	6
2 THEORETICAL BACKGROUND.....	9
2.1 Single reference methods .....	9
2.1.1 Density functional theory .....	9
2.1.2 GW method .....	16
2.2 Multireference methods.....	17
2.2.1 Complete Active Space Self Consistent Field.....	17
2.2.2 Complete Active Space Spin-Orbit Configuration Interaction.....	21
3 CATALYSIS.....	23
3.1 Introduction to catalysts .....	23
3.1.1 Homogeneous catalysis .....	24
3.1.2 Photocatalysis .....	25
3.1.3 Electrocatalysis.....	26
3.1.4 Redox catalysis.....	27
4 APPLICATIONS .....	29
4.1 Asymmetrically Difunctionalized 1,1'-Ferrocenyl Metalloligands and Their Transition Metal Complexes.....	29
4.1.1 Introduction .....	29
4.1.2 Computational Details .....	30
4.1.3 Results and Discussion.....	31
4.1.4 Conclusion.....	46

4.2 Photocatalytic reduction of CO <sub>2</sub> by highly efficient homogeneous Fe <sup>II</sup> catalyst based on 2,6-bis(1,2,3-triazol-yl-methyl) pyridine. Comparison with analogues.....	48
4.2.1 Introduction .....	48
4.2.2 Computational Details .....	51
4.2.3 Results and Discussion .....	51
4.2.4 Conclusion .....	68
4.3 Cooperativity-driven reactivity of a dinuclear copper dimethylglyoxime complex .....	70
4.3.1 Introduction .....	70
4.3.2 Computational Details .....	71
4.3.3 Results and Discussion .....	72
4.3.4 Conclusion .....	88
5 SUMMARY.....	90
6 ACKNOWLEDGEMENTS.....	92
7 COPYRIGHT PERMISSIONS.....	93
8 LIST OF SCIENTIFIC PUBLICATIONS.....	94
9 LIST OF FIGURES .....	95
10 LIST OF TABLES.....	99
11 LIST OF SCHEMES.....	102
12 BIBLIOGRAPHY .....	103

## ABSTRACT

Homogeneous transition metal-catalyzed reactions have a wide variety of uses in the chemical industry, including oxidation, polymerization, hydrogenation, and CO reactions, to name just a few of these applications.<sup>1</sup> This thesis focuses mostly on photocatalysis, electrocatalysis, and redox catalysis as its three primary areas of investigation. We have examined reactions that are catalyzed by mono- and binuclear transition metal complexes, with a particular emphasis on the interplay between metal centers. In order to analyze the reactivity of catalysts and propose a mechanism for doing so, we began by looking at the electronic structure of each individual catalyst. Calculations on the mononuclear and binuclear transition metal complexes, as well as the intermediates and transition states of processes catalyzed by these complexes, are carried out as part of this work in the field of quantum chemistry. An investigation is being conducted into redox-induced catalysis as well as processes that involve electron transport between metal centers. This covers redox reaction systems as well as photocatalytic systems for the reduction of carbon dioxide. The data support the experimental findings and shed the light on possible mechanism of the reaction.

## ZUSAMMENFASSUNG

Homogene, durch Übergangsmetalle katalysierte Reaktionen werden in der chemischen Industrie vielfältig eingesetzt, z. B. bei der Oxidation, Polymerisation, Hydrierung und CO-Reaktionen, um nur einige dieser Anwendungen zu nennen.<sup>1</sup> Diese Arbeit konzentriert sich vor allem auf die Photokatalyse, die Elektrokatalyse und die Redoxkatalyse als die drei Hauptuntersuchungsbereiche. Wir haben Reaktionen untersucht, die durch ein- und zweikernige Übergangsmetallkomplexe katalysiert werden, wobei der Schwerpunkt auf dem Zusammenspiel der Metallzentren lag. Um die Reaktivität der Katalysatoren zu analysieren und einen Mechanismus dafür vorzuschlagen, haben wir uns zunächst die elektronische Struktur jedes einzelnen Katalysators angesehen. Im Rahmen dieser quantenchemischen Arbeiten werden Berechnungen zu den ein- und zweikernigen Übergangsmetallkomplexen sowie zu den Zwischenstufen und Übergangszuständen der von diesen Komplexen katalysierten Prozesse durchgeführt. Untersucht werden die redox-induzierte Katalyse sowie Prozesse, die den Elektronentransport zwischen Metallzentren beinhalten. Dies umfasst sowohl Redox-Reaktionssysteme als auch photokatalytische Systeme zur Reduktion von Kohlendioxid. Die Daten unterstützen die Ergebnisse der Experimente und geben Aufschluss über den möglichen Mechanismus der Reaktion.

# 1 INTRODUCTION

The concept of homogeneous catalysis with transition metals was developed when it was discovered that the local environment of the metal center affects its electronic structure and also determines the potential interactions with other molecules. The ensuing chemical transformation can then be very selective as only specific molecules can bind to the metal and react primarily in one direction. Although we have a good understanding of a lot of processes, designing novel catalysts is still a difficult task. In the early 1980s, it was predicted that homogeneous catalysis will be well known enough to do so in the following 20 years.<sup>2</sup>

Many specific branches of homogeneous catalysis have been developed in the last hundred years, for example photocatalysis, electrocatalysis, and redox catalysis. All of them play an important role in solving modern problems of the chemical industry, i.e. photocatalysis is actively used in water splitting and hydrocarbon production from CO<sub>2</sub>. The explosion in research into artificial photosynthesis<sup>3</sup> (which frequently includes redox and electrochemical steps) resulted in the establishment of many institutes dedicated to this field, as well as the development of a few industrially relevant practical realizations.

In this regard, quantum chemical calculations can be a tempting substitute for costly experimental trial and error. However, there are a number of difficulties with computational modeling for electrochemical and photocatalysts, starting with the use of excited states.

The structures and reactivities of mono- or bi-nuclear complexes and mixed-valence compounds, which are important particularly in redox or electrochemical processes, are investigated in the current work. The project has been carried out in the framework of the Transregio-Sonderforschungsbereich 88 "Cooperative Effects in Homo- and Heteronuclear Complexes (3MET)". To better understand the characteristics and reactivities of a variety of metal-containing systems, theoretical calculations were made to look at their electronic structures.

The subjects discussed in this work span a wide variety of structural issues (molecular geometry and electronic structure), calculations using spectroscopic data, and the fundamentals of

chemistry—reaction pathways. The latter are used to not only rationally develop new, more efficient, and more selective catalysts but also to explain observed phenomena. Metallic nanoparticles are already being used as catalysts in the homogeneous metallic catalysts, which are complex many-body systems.<sup>4</sup> In order to properly understand these nanosized systems or clusters, we require techniques that offer a balance between accuracy and cost (time of calculations, computer resources needed).

On the one hand, throughout the years, extremely precise procedures have been established, and we are aware of ways to methodically improve our results; but, on the other hand, the size of the systems of interest restricts the applicability of the majority of these methods. Density functional theory (DFT), more specifically in the Kohn-Sham formulation,<sup>5</sup> has been without a shadow of a doubt the most fruitful method for studying these systems over the past two decades. However, Jacob's ladder, as proposed by Perdew,<sup>6</sup> appears to be fairly unstable. Jacob's ladders with higher rungs (functionals that are better by design) may not necessarily produce better outcomes when applied to a property of interest.<sup>7</sup>

Due to the size of the investigated systems, DFT methods are used in the majority of calculations involving homogeneous catalysis with metal complexes.<sup>8,9</sup> However, the unbalanced treatment of static and dynamic correlation makes the transition metal chemistry a difficult test for any functional, as the majority of the popular exchange-correlation functionals were optimized and benchmarked primarily against compounds made up of main group elements. Before drawing any conclusions, many writers emphasize the need to verify a set of DFT functionals.<sup>10</sup> A common strategy in calculations of complex, multimetallic systems is to compare different functionals with known experimental data. However, if experimental data is unavailable or has significant uncertainty, such a strategy will undoubtedly fail. By obtaining reliable wave function-based reference data for each system, this effort attempts to go beyond the typical DFT calculations in order to learn more about the chemical structure or reaction under investigation.

This thesis is organized as follows: Chapter 2 presents the key ideas of the applied techniques. This review concentrates on the principles of a few selected quantum chemistry methods and aims to illustrate the advantages and disadvantages of various approaches. The two subsections that make up this chapter address single and multiple reference approaches. With a focus on homogeneous catalysis, Chapter 3 addresses several types of catalysis, while Chapter 4 goes deeper into three challenging projects involving mono- and bi-complexes. In order to suggest a

mechanism and study the reactivity of catalysts, we first investigated the electronic structure of each catalyst. The collected data can be readily compared with experimental results in all applications. In addition, multireference calculations are utilized in chapter 4.3 to get insight into these kinds of compounds.

## 2 THEORETICAL BACKGROUND

The goal of this chapter is to provide an overview of the approaches used in this work. Theoretical frameworks that are thoroughly developed and documented in textbooks are basically briefly described. The emphasis is placed on procedures that have recently been created as well as ways enabling them to be used in large molecular systems. The chapter is split into two main sections: These two separate sections deal with single reference and multiple reference methods for computing quantum chemical equations.

### 2.1 Single reference methods

#### 2.1.1 Density functional theory

Condensed-matter physics, computational physics, and computational chemistry all use density functional theory (DFT) as one of the most advanced and widely used methods.

From a more fundamental viewpoint, DFT is a "first-principles" electronic structure method to solving the fermionic many electron problem, which forms the basis of the majority of chemistry as well as significant portions of biology and physics. DFT may effectively address a wide range of issues in (bio)chemistry and physics when used in conjunction with a combined quantum-classical approach for the nuclei using molecular dynamics (MD) or harmonic approximations for the potential energy surface (PES).<sup>11</sup>

Comparatively to the alternatives, which include less accurate and robust but faster semi-empirical quantum mechanics<sup>12, 13</sup> (often referred to as SQM) and more accurate and robust but slower wavefunction-theory-based approaches like coupled-cluster, DFT offers an excellent balance between computation time and the quality of the results.

The Schrödinger equation for  $N$  interacting electrons moving in an external potential is approximated using traditional techniques. This traditional method has significant drawbacks. Firstly, the resultant wave function is extremely complex, even for the smallest system with  $N$  electrons. Second, it seems hard to describe larger systems since even for a smaller system, the computing support and expense are very high.

The DFT has therefore suggested a different strategy in an effort to maybe find a solution to the issues mentioned. Instead of taking into account the many-body wave function, DFT technique uses the one-body density as a functional variable. Instead of the  $3N$  coordinate wave-function used in the conventional technique, the density is a function of three spatial coordinates. Hohenberg-Kohn and the Kohn-Sham theorem laid the groundwork for density functional theory; these concepts will be covered in more detail in the sections that follow.

In DFT, the essential quantity is the electron density  $\rho(\mathbf{r})$  which is defined as an integral of the module of a wave function over all space and spin variables of electron  $i$ , multiplied by the number of electrons  $N$ :

$$\rho(\mathbf{r}_1) = N \int |\Psi(\mathbf{r}_1, \mathbf{r}_2, \mathbf{r}_3 \dots, \mathbf{r}_N)|^2 ds_1 d\mathbf{r}_2 d\mathbf{r}_3 \dots d\mathbf{r}_N \quad (1)$$

The number of electrons is determined by integrating the electron density over space, and each molecule's density has cusps where its nuclei are located.

The nuclear charge determines the cusp's slope. According to Hohenberg and Kohn's research,<sup>14</sup> there is only one external potential that can be used to define the interaction between nuclei and electrons  $v(\mathbf{r}_i)$ .

$$v(\mathbf{r}_i) = - \sum_{A=1}^M \frac{Z_A}{r_{iA}} \quad (2)$$

This yields the density  $\rho(\mathbf{r}_i)$ . As a result, the electron density contains all of the information about the molecule, and its function may be used to express the total energy of the system:

$$E[\rho] = V_{en}[\rho] + T[\rho] + V_{ee}[\rho] = \int \rho(\mathbf{r})v(\mathbf{r})d\mathbf{r} + F[\rho] \quad (3)$$

Since there are only one-electron operators in  $\hat{V}_{en}$  and electrons cannot be distinguished, the electron-nucleus interaction in equation (3) can be described by the integral of the density.

The kinetic energy and electron-electron repulsion functionals make up the so-called universal functional, or  $F[\rho]$ . The energy obtained with any trial density  $\tilde{\rho}$ , which defines its own wave function  $\tilde{\Psi}$ , will be higher than or equal to the energy that corresponds to the exact density  $\rho$ , according to this statement:

$$E[\tilde{\rho}] = \langle \tilde{\Psi} | \hat{H} | \tilde{\Psi} \rangle = \int \tilde{\rho}(\mathbf{r})v(\mathbf{r})d\mathbf{r} + F[\tilde{\rho}] \geq E[\rho] \quad (4)$$

Only the exact universal functional with an undetermined form is consistent with relation (4). However, Kohn and Sham suggested a sensible strategy.<sup>5</sup> They proposed that one could create a fictitious system of  $N$  non-interacting electrons moving in the external field  $\hat{v}_0(\mathbf{r})$  matched in such a way that it would produce the electron density of the real system in order to obtain the electron density of  $N$  electrons moving in the external field  $v(\mathbf{r})$  arising from nuclei and interacting with one another through Coulombic forces. The system's total energy can therefore be expressed in the following way:

$$E = \int \rho(\mathbf{r})v(\mathbf{r})d\mathbf{r} + T_s[\rho] + J[\rho] + E_{xc}[\rho] \quad (5)$$

Where  $J[\rho]$  is a standard Coulomb repulsion and  $T_s[\rho]$  is the sum of all electrons' kinetic energy when they are not interacting:

$$J[\rho] = \frac{1}{2} \iint \frac{\rho(\mathbf{r}_1)\rho(\mathbf{r}_2)}{r_{12}} d\mathbf{r}_1 d\mathbf{r}_2 \quad (6)$$

Individual electron Coulomb holes are excluded from this repulsive functional. This is transferred to the exchange-correlation functional  $E_{xc}[\rho]$ , which also includes the correction for a Fermi hole, ensuring that electrons with the same spin do not interact, as well as a tiny kinetic energy correction to account for the actual kinetic energy of electrons. Even while it is clear that the latter is little, it is unknown exactly how this functional is structured. As a result, some exchange-correlation functional that has been predetermined must be used in molecular calculations. The Kohn-Sham method involves the self-consistent solution of the Kohn-Sham equations, which can be compared to HF equations.

$$\left( -\frac{1}{2}\nabla^2 + v(\mathbf{r}) + \frac{\delta J[\rho]}{\delta\rho(\mathbf{r})} + \frac{\delta E_{xc}[\rho]}{\delta\rho(\mathbf{r})} \right) \varphi_i(\mathbf{r}) = \epsilon_i \varphi_i(\mathbf{r}) \quad (7)$$

The total electron density that can be employed in total energy calculations is then built using the Kohn-Sham orbitals, or  $\varphi_i(\mathbf{r})$  (see equation (5)).

The exchange-correlation functional that each DFT method uses is typically used to categorize them. In addition, the functionals are frequently divided into an exchange part and a correlation part, and any combination of these parts can be used to create new functionals.

## Theoretical background

The essential variables utilized to define the exchange-correlation functional can be taken into account to perform a heuristic characterization. J. P. Perdew offered a "Jacob's ladder" approach, where one can anticipate or at least hope for an improvement in the accuracy at each step up the ladder (see Figure 2.1.1).<sup>15, 16</sup> The scheme arranges functionals from the Hartree approximation (earth) to the exact approximation of the XC functional (heaven of chemical accuracy). Additionally, the functionals are divided into empirical and non-empirical categories based on the type of approximations used. Only rules of physics and theories make up the latter group since in the former, functionals are created based on fitting to outcomes of atomic property experiments.



**Figure 2.1. 1** Illustration of Jacob's Ladder of DFT accuracy. Reused from Ref <sup>17</sup> with permission from Springer Nature, copyright 2020.

Local density approximation has become popular for solid-state systems, though it is very inaccurate for molecules. The exchange-correlation energy in the LDA technique is provided by

$$E_{exc}^{LDA}[\rho] = \int d^3r \rho(\mathbf{r}) e_{exc}(\rho(\mathbf{r})) \quad (8)$$

where the exchange-correlation energy of an electron in a uniform electron gas with the same density  $\rho(\mathbf{r})$  is represented by  $e_{exc}(\rho(\mathbf{r}))$ . Additionally, LDA can be extended to polarized systems, in which case it is known as the local spin density approximation (LSDA). Although for actual electronic systems, this need is rarely reached. However, LDA has demonstrated to be incredibly accurate for a wide range of systems where the densities are slowly fluctuating.

The main benefits of this approximation in DFT over other approaches like Hartree-Fock are that it performs well and allows for highly accurate determination of a large number of empirically known physical parameters. These errors are magnified when bond lengths are too short in poorly bonded systems. The issue is whether LDA is relevant. For instance, LDA is effective with group IV semiconductors, but it was uncertain how well this approximation would perform.

Due to the use of a homogeneous electron gas, LDA is incredibly accurate for tiny molecules where density variations are minimal. For covering of this drawback, a functional that incorporates the density gradient was created (in order to account for density gradient  $\nabla\rho(\mathbf{r})$ ). This was a Generalized gradient approximations (GGA).

The GGA approximation yields the exchange-correlation energy as follows:

$$E_{exc}^{GGA}[\rho] = \int d^3r f(\rho(\mathbf{r}), \nabla\rho(\mathbf{r})) \quad (9)$$

In LDA  $e_{exc}(\rho(\mathbf{r}))$  was unique but not in GGA; as a result, several different techniques are available depending on the system of interest. The qualities that are intended to be incorporated into the restricted functional approximation utilizing the accurate functional should be kept in mind when one builds the GGA. Particularly in chemistry, GGA has become very popular and has proven to be quite accurate in quantum calculations. It is also less computationally expensive.

The Perdew-Burke-Ernzerhof (PBE) functional is one of the most often used GGA approximations.<sup>18</sup> It is generated using a specific presumption that is true for the exact functional that can be approximated in form. As a result, it is empty of fitted parameters, which is true for many different systems. Their applicability is restricted by the use of fits to the reference data in GGA functional.

GGA has undergone additional development to become a new class of "meta-GGA" functionals (e.g. TPSS and TPSSH)<sup>19, 20</sup> in recent years. In addition to the GGA and LDA functional, the Kohn-Sham orbitals' kinetic energy, which is determined by:

$$\tau(\mathbf{r}) = \frac{1}{2} \sum_i^{\text{occupied}} |\nabla\phi_i(\mathbf{r})| \quad (10)$$

The following provides the "meta-GGA" functional:

$$E_{exc}^{mGGA}[\rho] = \int d^3r f(\rho(\mathbf{r}), \nabla\rho(\mathbf{r}), \tau(\mathbf{r})) \quad (11)$$

By introducing a new variable, the mGGA functional has greater flexibility, which is used to incorporate more exact features into the approximation. mGGA also explicitly relies on the Kohn-Sham orbitals, unlike LDA and GGA.

Despite advancements in LDA and GGA, self-interaction errors affect both functionals. The Pauli exclusion principle, which states that interactions with other electrons with the same spin cannot be excluded from energy contributions, was not successfully applied by either party. This may cause the band gap to be underestimated and the electron to be artificially delocalized. The energy is integral over the density function at a particular place in the system and is also independent of all other spatial locations, making LDA and GGA functionals local. Gradient information introduces some non-locality, but it cannot account for the interaction across longer distances. In contrast, the Hartree-Fock theory (HF) method's exchange term specifically cancels the self-interaction, but it is non-local, – i.e., it is calculated as an integral over two spatial coordinates. The exact exchange and the GGA exchange are combined to form the hybrid functional, which is determined by:

$$E_{exc}^{HYB}[\rho] = \alpha E_{exc}^{HF}[\rho] + (1 - \alpha) E_{exc}^{GGA}[\rho] \quad (12)$$

where  $\alpha$  is a variable that governs HF exchange, various values of  $\alpha$  are used for various functions, which can further enhance the system's performance. B3LYP (with 20% HF exchange)<sup>21, 22</sup> and PBE0 (with 25% HF exchange)<sup>23</sup> are examples of hybrid functionals, which make up the fourth generation of XC functionals.

In addition, the r<sup>2</sup>SCAN-3c composite approach<sup>24</sup> has demonstrated in preliminary investigations consistent performance for both open and closed shell transition metal complexes and is available

as a reliable "Swiss army knife" electronic structure method for thermochemistry, geometries, and non-covalent interactions. The  $r^2$ SCAN meta-GGA paired with the D4 dispersion correction<sup>25</sup> and the geometrical counter poise-correction<sup>26</sup> form the basis of this method.

The modified triple-basis set, def2-mTZVPP, is almost as computationally efficient as the def2-mTZVP basis set of B97-3c. It is larger and more consistent for the light main-group elements.  $r^2$ SCAN-3c has a somewhat higher computational cost than B97-3c.

The effectiveness of  $r^2$ SCAN-3c was thoroughly evaluated for thousands of energy data points, including molecular thermochemistry, non-covalent interactions in small and large intermolecular complexes, organometallic reaction energies, organic molecule lattice energies, ice polymorphs, and the adsorption of small molecules on coinage metals and polar surfaces.<sup>24</sup> It was even show that  $r^2$ SCAN-3c is more accurate than  $r^2$ SCAN-D4/QZ4P, being simultaneously 6 times faster.<sup>27</sup>

### 2.1.1.1 Time-dependent density functional theory (TDDFT)

Time-dependent Schrödinger equation is provided by:

$$i \frac{\partial}{\partial t} \psi(\mathbf{r}, t) = \hat{H}(t) \psi(\mathbf{r}, t) \quad (13)$$

where  $\psi$  is the many-body wave-function of  $N$  interacting electrons, with  $\mathbf{r} = (\mathbf{r}_1, \mathbf{r}_2, \dots, \mathbf{r}_N)$  coordinates, and  $\hat{H}(t)$  time-dependent external potential. When a system meets the provided initial condition, this equation defines the system's time evolution:

$$\psi(\mathbf{r}, t = t_0) = \psi(\mathbf{r}) \quad (14)$$

According to the Runge-Gross theorem,<sup>28</sup> the time-dependent density  $\rho(\mathbf{r}, t)$  and the external time-dependent potential,  $v(\mathbf{r}, t)$ , which eventually contribute to the time evolution of  $\rho(\mathbf{r}, t)$ , have a one-to-one connection. The system's observables can all be expressed as functions of density. Kohn-Sham scheme provided the Runge-Gross theorem's operational framework.

Let us define a non-interacting electron system using the Schrödinger equation:

$$i \frac{\partial}{\partial t} \phi(\mathbf{r}, t) = \left[ -\frac{\nabla^2}{2} + v_{ks}(\mathbf{r}, t) \right] \phi_i(\mathbf{r}, t) \quad (15)$$

Kohn-Sham potential is similarly determined by

$$v_{ks}[\rho](\mathbf{r}, t) = v(\mathbf{r}, t) + \int d^3r' \frac{\rho(\mathbf{r}', t)}{|\mathbf{r} - \mathbf{r}'|} + v_{exc}[\rho](\mathbf{r}, t) \quad (16)$$

where  $v(\mathbf{r}, t)$  stands for the nuclei's Coulombic potential as well as the external electromagnetic field's time-dependent contribution. Additionally, the function for the time-dependent exchange correlation potential is selected so that the density of the electrons in the Kohn-Sham orbital is equivalent to the density of the electrons in the interacting system.

$$\rho(\mathbf{r}, t) = \sum_i^{\text{occupied}} |\phi(\mathbf{r}, t)|^2 \quad (17)$$

Exchange-correlation potential  $v_{exc}$  must be roughly calculated because it is a complex quantity. The most popular approximation is referred to as the adiabatic local density approximation (ALDA). It is assumed in the ALDA approximation that the exchange-correlation potential at time  $t$  equals the ground-state LDA potential, which is denoted by:

$$E_{exc}^{ALDA}[\rho](\mathbf{r}, t) = E_{exc}[\rho](\mathbf{r}, t) \quad (18)$$

Calculating the energy of excited states in isolated systems and, less frequently, solids, is the most prominent use of TDDFT. These calculations are based on the observation that a system's exact excitation energies coincide with the poles of the linear response function, which describes how the electron density varies as the external potential changes. The exchange-correlation kernel, which is the functional derivative of the exchange-correlation potential with respect to the density, is also necessary for these calculations.<sup>29, 30</sup>

### 2.1.2 GW method

The *GW*-method is a well-established method for correcting errors in DFT-estimates of the ionization potentials and electron affinities found in single particle excitation spectra for electronic band structure calculations in solids. The Green's function  $G$  serves as its main focus, and its poles characterize the energies and lifetimes of single-particle excitations. The *Hedin equations*, which are a power series of the screened Coulomb interaction  $W$ , serve as the foundation for the *GW*-approach.<sup>31</sup> The screened Coulomb interaction  $W$  is estimated in the *GW*-equations as an approximation to the Hedin-equations while excluding the so-called *vertex corrections*.<sup>32, 33</sup>

In general, one could claim that the *GW*-approach, like other one electron Green's function approaches, substitutes a *self-energy*  $\Sigma$ , for the problematic unknown XC-potential in the DFT

calculation. In this procedure, the KS-equations are converted into a collection of *quasi-particle* equations that are self-consistent. Since  $\Sigma[G]$  is a functional of  $G$ , much like the XC-potentials of DFT are functionals of the electron density, it frequently needs to be changed throughout the iteration cycle that resolves the quasi-particle equations. Unlike XC-potentials, it is not Hermitian and is energy-dependent. Additionally,  $\Sigma$  is nonlocal in space, like the Fock-operator and unlike (semi) local XC-potentials.<sup>34</sup>

The fact that the poles of Green's functions are built to determine the single-particle (or quasi-particle) excitation energies is one of its important characteristics. Particularly, the primary vertical ionization energies correspond to the *GW*-quasi-particle energies up to the highest occupied molecular orbital (HOMO). We have access to the ionization energies important for core-level spectroscopies when employing a basis that tracks core states explicitly.

The ability to calculate other physical quantities is also made possible by understanding the entire quasi-particle spectrum and quasi-particle states. Molecular transport is one example, while another is the Bethe-Salpeter equation-based calculation of optical excitation spectra (BSE).<sup>35</sup> Additionally, using knowledge of  $G$  and  $W$ , total energy estimations for structure relaxations can be made.<sup>36</sup>

## 2.2 Multireference methods

### 2.2.1 Complete Active Space Self Consistent Field

The Hartree-Fock technique can be viewed of as being extended by the CASSCF method, a special type of multiconfigurational SCF method.<sup>37</sup> It provides a strong foundation for multireference configuration interaction (MR-CI) treatment as well as a very effective tool for studying static correlation effects. It can be used to calculate averages of both the ground state and exciting states. For a specified CASSCF state, the wavefunction is expressed as:

$$|\Psi_I^S\rangle = \sum_k C_{kI} |\Phi_k^S\rangle \quad (19)$$

The CASSCF  $N$ -electron wavefunction for state  $I$  with total spin  $S$  is given here as  $|\Psi_I^S\rangle$ . The set of  $|\Phi_k^S\rangle$  is a collection of configuration state functions, each adapted to a particular total spin  $S$  (for

instance, a linear combination of Slater determinants). The first set of variational parameters are represented by the expansion coefficients  $C_{kl}$ . A common set of orthonormal molecular orbitals,  $\psi_i(\mathbf{r})$ , which are enlarged in basis functions,  $\psi_i(\mathbf{r}) = \sum_{\mu} c_{\mu i} \phi_{\mu}(\mathbf{r})$ , serve as the building blocks for each configuration state functions (CSF). The second set of variational parameters consists of the MO coefficients  $c_{\mu i}$ .

The Rayleigh quotient<sup>38</sup> determines the energy of the CASSCF wavefunction

$$E(\mathbf{c}, \mathbf{C}) = \frac{\langle \Psi_I^S | \hat{H}_{\text{BO}} | \Psi_I^S \rangle}{\langle \Psi_I^S | \Psi_I^S \rangle}, \quad (20)$$

which serves as an upper limit on the true total energy. The CASSCF calculations, however, are not intended to produce total energy estimates that are near to the exact energy. One of the causes of this is CASSCF's inability to appropriately treat the dynamic electron correlation. This can be achieved with higher methods, i.e. CASPT2, NEVPT2, SOCI.

The CASSCF approach makes the energy stationary with regard to changes in both sets of MO and CI coefficients, making it fully variational. The gradient of the energy with respect to the MO and CI coefficients vanishes at convergence.

$$\frac{\partial E(\mathbf{c}, \mathbf{C})}{\partial c_{\mu i}} = 0, \quad (21)$$

$$\frac{\partial E(\mathbf{c}, \mathbf{C})}{\partial C_{kl}} = 0 \quad (22)$$

In CASSCF calculations, the MO space is partitioned into three subspaces: The "inactive orbitals" are the orbitals which are doubly occupied in all configuration state functions (labels  $i, j, k, l$ ); the orbitals with variable occupation numbers in the different CSFs (labels  $t, u, v, w$ ) are referred to as "active orbitals", and the "external orbitals" (labels  $a, b, c, d$ ).<sup>39</sup>

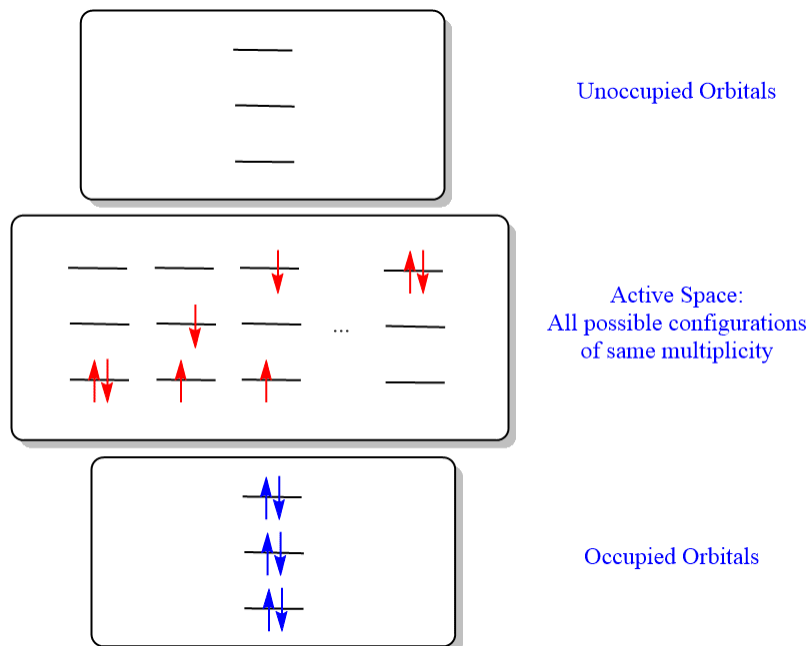


**Figure 2.2. 1** CASSCF orbitals, where inactive orbitals are doubly occupied, and full CI calculations are carried out in active space.

Regarding unitary transformations within the three subspaces, the wavefunction and energy are invariant. The unique characteristic of a CASSCF wavefunction is that each subspace is given a set number of electrons.

It naturally follows that the internal subspace is entirely filled, whereas the CSFs in the active space represent a full-CI of  $n$ -electrons in  $m$ -orbitals. However, the CSF list is designed in a way that yields a wavefunction with well-defined total spin (and potential space) symmetry. A CASSCF( $n,m$ ) wavefunction is the name given to such a wavefunction. With the number of active orbitals and the number of active electrons, the CSF list expands incredibly quickly. Depending on the system, one million CSFs in the active space or around 14 active orbitals represent the limit of viability.

In many cases, it is preferable to optimize the orbitals for the average of multiple states rather than a single state. The energy for state  $I$  is rewritten as follows:

$$E_I(\mathbf{c}, \mathbf{C}) = \sum_{pq} \Gamma_q^{p(I)} h_{pq} + \sum_{pqrs} \Gamma_{qs}^{pr(I)} (pq | rs) \quad (23)$$

The one- and two-particle reduced electron density matrices for this state are shown here as  $\Gamma_q^{p(I)}$  and  $\Gamma_{qs}^{pr(I)}$  (labels  $p, q, r$ , and  $s$  span the internal and active subspaces):

$$\Gamma_q^{p(I)} = \langle \Psi_I^S | E_q^p | \Psi_I^S \rangle \quad (24)$$

$$\Gamma_{qs}^{pr(I)} = \frac{1}{2} \langle \Psi_I^S | E_q^p E_s^r - \delta_{qr} E_s^p | \Psi_I^S \rangle \quad (25)$$

Simply averaging the density matrices with arbitrary weights  $w_I$  that must total to one yields the average energy.

$$\Gamma_q^{p(av)} = \sum_I w_I \Gamma_q^{p(I)} \quad (26)$$

$$\Gamma_{qs}^{pr(av)} = \sum_I w_I \Gamma_{qs}^{pr(I)} \quad (27)$$

$$\sum_I w_I = 1 \quad (28)$$

In general, CASSCF wavefunctions are far more challenging to optimize than RHF (or UHF) wavefunctions, with the exception of simple instances. The energy functional may have numerous local minima in  $(\mathbf{c}, \mathbf{C})$  space and fluctuations in  $\mathbf{c}$  and  $\mathbf{C}$  may be closely linked, which is the underlying cause. As a result, the choice of starting orbitals and the choice of which orbitals and electrons are included in the active space have a significant impact on whether a CASSCF investigation is successful.

Exchange couplings in multinuclear transition metal complexes are poorly described by CASSCF. Many times, by a factor of 2-3,<sup>40, 41</sup> antiferromagnetic couplings—commonly referred to as superexchange<sup>42</sup>—are massively underestimated. This is particularly true if only a limited number

of metal-centered active orbitals—five active orbitals per d-block center and seven active orbitals for each f-block center—is used. For multinuclear complexes, extending such an active space is not a possibility because one would relatively quick reach computational limits. Dynamic correlation must typically be included to improve CASSCF, whether through perturbation theory or methods of the configuration interaction (CI) kind. However, it is typically quite expensive to add dynamic correlation on top of a large active space CASSCF calculations.<sup>43</sup> It has been shown that one of the primary causes for the underestimation of superexchange in CASSCF-type calculations is the inflexibility of the CAS ground state wave functions to describe charge-transfer (CT) configurations. As a result, T. Bodenstein implement a practical and economical approach to improve CASSCF exchange couplings.<sup>44</sup> The modified complete active space configuration interaction techniques (MCASCI)<sup>45</sup> can be used to describe huge exchange coupled systems that are inaccessible with conventional multi reference methods by adjusting the weight of the CT configurations in the wave functions.

### 2.2.2 Complete Active Space Spin-Orbit Configuration Interaction

In many applications, spin-orbit coupling must be present. For instance, without spin-orbit coupling, g-matrix anisotropy or zero-field splitting would not exist (or be very minimal). When spin-orbit coupling is activated in systems where the ground state is quasi-degenerate (i.e., there are multiple spin multiplets with energies that are not much larger than the strength of the spin-orbit interaction), these close-lying states are strongly mixed, possibly requiring consideration of the entire quasidegenerate manifold in order to obtain a qualitatively accurate description of the electronic and magnetic properties.<sup>46</sup>

However, the Hamiltonian's symmetry is reduced, and the computations become significantly more complex if spin-orbit coupling is taken into account. Due to this, the computation for the common spin-orbit configuration interaction ansatz (SOCI) begins without spin-orbit coupling and includes it later. To achieve this, the Hamiltonian is divided into a spin-orbit component and a nonrelativistic (or scalar-relativistic) part, designated as  $\hat{H}_{sc}$  and  $\hat{H}_{SOC}$ , respectively, starting from CI-type wave functions that diagonalize  $\hat{H}_{sc}$ :

$$\langle \Psi_I | \hat{H}_{sc} + \hat{H}_{soc} | \Psi_J \rangle = \delta_{IJ} E_I + \langle \Psi_I | \hat{H}_{soc} | \Psi_J \rangle \quad (29)$$

If the wave functions  $\Psi_I$  cover at least the entire quasi-degenerate set of scalar Hamiltonian eigenstates, then this approach is particularly well adapted to handle quasi-degeneracies. This is the method's primary weakness since, for oligonuclear transition metal complexes, this number can grow to be quite big (it scales exponentially with the number of spin centres).<sup>47</sup>

A different approach (CASOCI)<sup>47</sup> is to diagonalize both operators simultaneously in the same space and incorporate  $\hat{H}_{soc}$  directly in the Hamiltonian,  $\hat{H} = \hat{H}_{sc} + \hat{H}_{soc}$ . As a result, spin-orbit interaction, which couples all microstates in the CAS, is directly included into the diagonalization. This process eliminates the need to compute a large number of scalar quasi-degenerate states prior to the SOCI using the standard two-step procedure. The modified complete active space configuration interaction (MCASCI)<sup>45</sup> ansatz is used in conjunction with this approach to effectively tackle heavily exchange coupled systems.

## 3 CATALYSIS

### 3.1 Introduction to catalysts

A substance that speeds up a chemical reaction is called a catalyst. In the majority of cases, the catalyst actually creates a new, quicker reaction pathway (Figure 3.1.1). A catalyst is an agent that speeds up a reaction without being consumed itself. We only require a minimal amount of catalyst in comparison to the substrate since the catalyst is not consumed during the reaction and each catalyst molecule can take part in numerous multiple cycles. The ratio of substrate to catalyst shows how well the catalyst works, which is turnover number (TON) or turnover frequency (TOF).<sup>48, 49</sup>

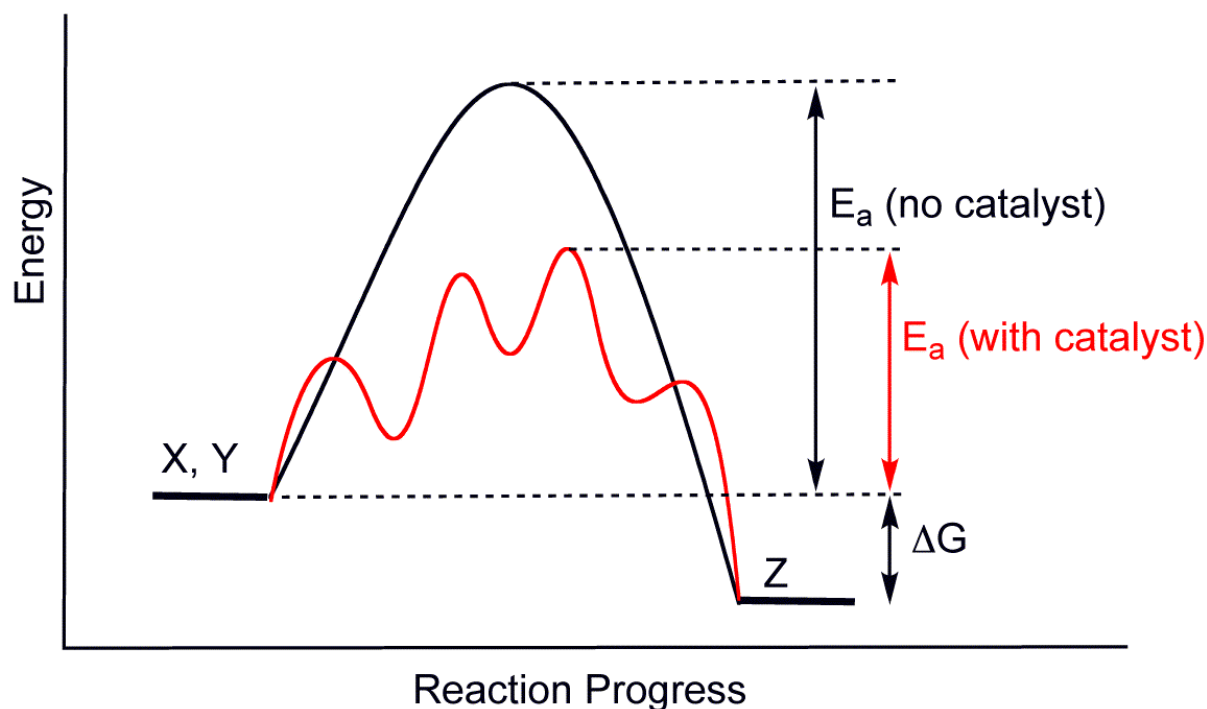


**Figure 3.1. 1** Generic potential energy diagram showing the effect of a catalyst in a hypothetical exothermic chemical reaction  $X + Y$  to give  $Z$ . The presence of the catalyst opens a different reaction pathway (shown in red) with a lower activation energy. The final result and the overall thermodynamics are the same.

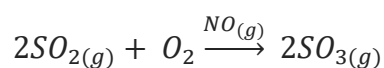
Applications for catalysis in daily life include electronics, polymers (plastics, adhesives), medicines, fine chemicals, agrochemicals, petroleum, and reducing the emission of hazardous gases from stationary sources, such as removing CO. Moreover, a variety of catalytic reactions were used in the 16th and 17th centuries, including ethanol oxidation to produce vinegar, fermentation to produce alcoholic beverages, and fat hydrolysis to produce soap. Jöns Jakob Berzelius, a Swedish chemist at the Stockholm Academy of Science, worked on this project for many years. Berzelius wrote that by the term catalysis he meant “the property of exerting on other bodies an action which is very different from chemical affinity. By means of this action, they produce decomposition in bodies, and form new compounds into the composition of which they do not enter”.<sup>50</sup>

Ostwald (1895)<sup>51</sup> is to be credited with another definition that is still relevant today: "a catalyst is a material that accelerates a chemical reaction without affecting the position of the equilibrium and thermodynamics of the reaction." Ostwald placed the idea of catalysis as a complete dynamic process that could be explained in terms of physical chemistry laws. His breakthrough research was honoured in 1909 with the Chemistry Nobel Prize.

Generally speaking, there are three subdisciplines in catalysis: Homogeneous catalysis, heterogeneous (solid-state catalyst), and biocatalysis. Since homogeneous catalysis was the main subject of the current thesis, it will be the sole subject of this chapter.

### 3.1.1 Homogeneous catalysis

Homogeneous catalysis refers to reactions in which the catalyst, reactants, and products are all in the same phase,<sup>52</sup> while heterogeneous catalysis refers to those reactions in which the catalyst, reactants, and substrate are all in distinct phases. The oxidation of SO<sub>2</sub> to SO<sub>3</sub> using the homogeneous catalyst provided by the NO molecule, which takes place in the gaseous phase, was the first industrially significant catalysed process, carried out in 1750. It's employed in the production of sulfuric acid.<sup>53</sup>



Nowadays, coordination or organometallic complexes are frequently referred to as homogeneous

catalysts. These catalysts suffer from drawbacks including low thermal stability and high catalytic recovery costs, although they have certain benefits like great selectivity and single active sites.

Homogeneous catalysis is becoming increasingly significant, even though heterogeneous catalysis is still the more cost-effective option for most industrial processes. Estimates show that homogeneous catalysis is only used in about 10–15% of all catalytic reactions.<sup>1</sup>

Oxidation, polymerization, hydrogenation, and CO reactions are only a few examples of the many chemical industry applications of homogeneous transition metal-catalyzed reactions.<sup>1</sup> Most recent developments in industrial homogeneous catalysis can be attributed to the discovery of new organometallic catalysts. The oxidation of hydrocarbons by oxygen molecules or peroxides is a common industrial application for homogeneous catalysts.

### 3.1.2 Photocatalysis

Huge efforts have been made to generate and produce clean, renewable energy to global energy and environmental crises. Solar energy is a clean, abundant, and sustainable natural resource. However, it is challenging to convert and store solar energy due to its inconsistent availability. Promising fuels can be produced via photocatalysis and/or electrocatalysis, like H<sub>2</sub> from water splitting and hydrocarbons from CO<sub>2</sub> reduction.<sup>54, 55</sup>

Photocatalysis is the reaction that takes place when a light source interacts with the surface of a substance (i.e., semiconductor materials). It is essential that at least two reactions occur simultaneously during this activity: an oxidation reaction using photogenerated holes and a reduction reaction using photogenerated electrons. The photocatalyst species should not vary at all during the procedure, hence the two aforementioned processes must be precisely synchronized to occur simultaneously.

Compared to traditional catalytic processes that require time-consuming procedures, high temperatures and pressures, and the use of transition metal catalysts, photocatalysis offers a number of significant advantages.<sup>56</sup>

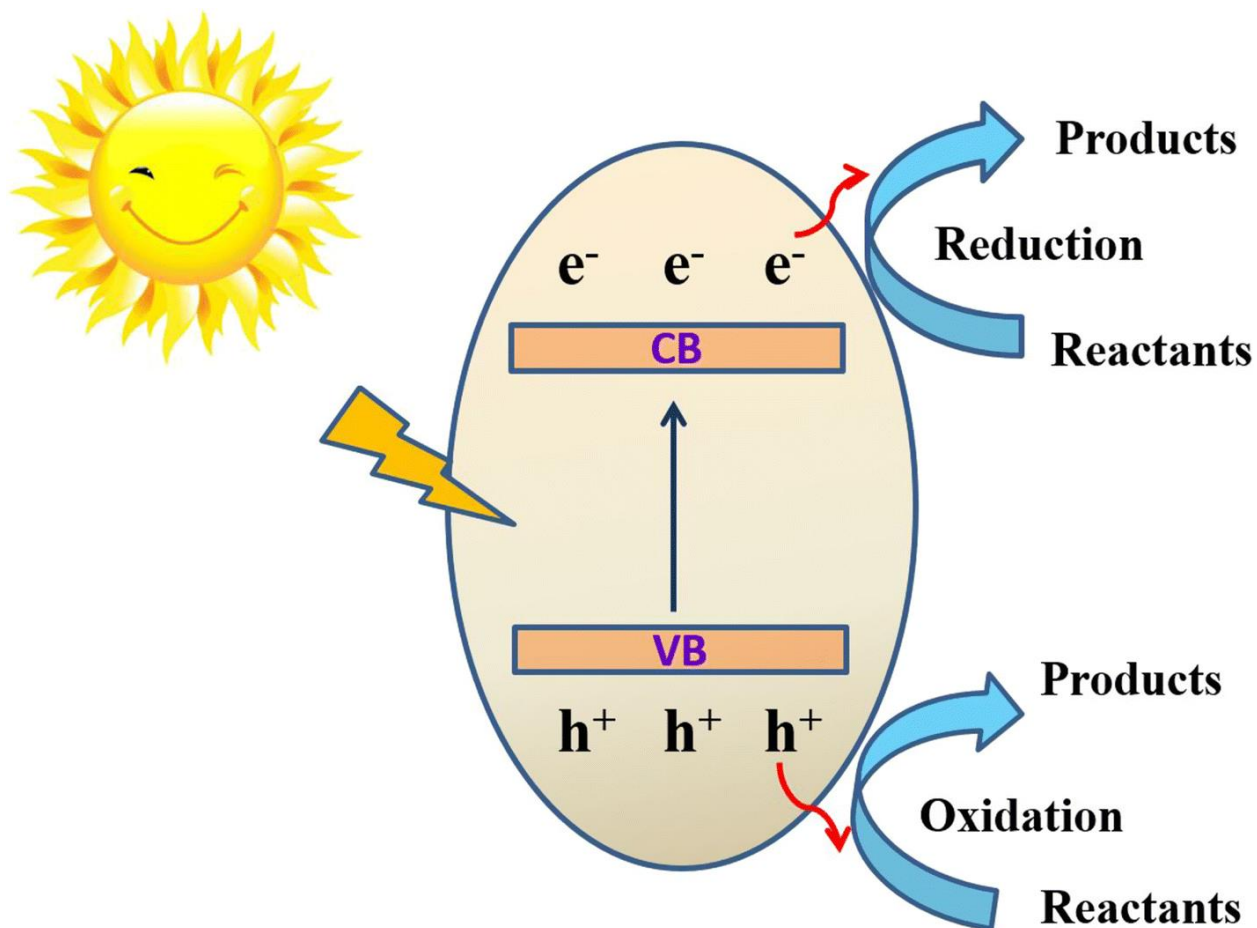


**Figure 3.1. 2** The mechanism of photocatalysis. VB corresponds to Valence Bands (Occupied Orbitals) and CB to Conduction Band (Unoccupied orbitals). (Reused from<sup>57</sup> with permission)

We looked into a photocatalysis for  $\text{CO}_2$  reduction, which is discussed in chapter 4.2.

### 3.1.3 Electrocatalysis

A catalyst that takes part in electrochemical reactions is known as an electrocatalyst. An exclusive class of catalysts known as electrocatalysts works at electrode surfaces or, more frequently, can be the electrode surface itself.

Activity, selectivity, and stability are the three metrics that electrocatalysts can be judged on. In order to quantify the activity of electrocatalysts, one must know how much current density is produced for a given applied potential and, consequently, how quickly a reaction is occurring. The

selectivity of electrocatalysts refers to their singular product production and preferential interaction with specific substrates. The ability of catalysts to tolerate the potentials at which transformations are taking place is critical in determining the stability of electrocatalysts.

Electrocatalysts can be divided into two groups: heterogeneous and homogeneous. Heterogeneous electrocatalysts, like platinized electrodes, are possible.<sup>58</sup> A water-soluble coordination complex that is catalyzing an electrochemical reaction in solution is an example of a homogeneous electrocatalyst because it is present in the same phase of matter as the reactants.<sup>59, 60</sup> Soluble homogeneous electrocatalysts aid in the transmission of electrons between the electrode and the reactants and/or enable a chemical transformation that is intermediate and is represented by an overall half reaction.<sup>61</sup>

### 3.1.4 Redox catalysis

Since there are no significant electronic interactions between the catalyst and substrate during redox catalysis, the electron transfer can be explained by the Marcus-Hush-Levich (MHL) model, which describes outer-sphere electron transfers<sup>62</sup> (although at an electrode surface in inner sphere (IS) processes, where a related expression of the electron transfer rate constant has recently been reported<sup>63</sup>). The redox catalyst (or redox mediator) is merely a shuttle for charges from the electrode surface to the substrate in the case of outer sphere (OS) electron transfer, interfering with the electrochemical (E) stages of the electrocatalytic cycle (Figure 3.1.3a). Notably, a redox catalyst does not affect the electrocatalytic cycle's the chemical (C) steps' transition states or the substrate's activation via an adduct.

A bonding contact between the catalyst and the substrate is associated with an electron transfer that takes place as an inner-sphere process (chemical catalysis). In contrast, an electronically activated chemical catalyst follows this action pattern, which deviates from the MHL model for OS electron transport.<sup>62</sup> By extending the historical meaning at the electrode surface, we use the word "electrocatalyst" in this perspective to refer to molecular homogeneous catalysts that proceed via IS electron transfers.

Inner-sphere electron transfers can be further divided into different categories. On the one hand, the electrocatalyst only speeds up the electron transfer E steps if bonding is present at the electron transfer transition state (Figure 3.1.3b). On the other hand, the contact may be closer and involve

the creation of an intermediate, such as a substrate-catalyst adduct, by the coordination of the substrate to a transition metal complex catalyst, as is frequently seen in the catalytic transformation of organic compounds. Here, the electrocatalyst not only speeds up the electron transfers (E steps) but is also made to play a crucial part in the activation of the substrate and the processes that result in the production of elementary bonds, which are governed by the C steps (Figure 3.1.3c).

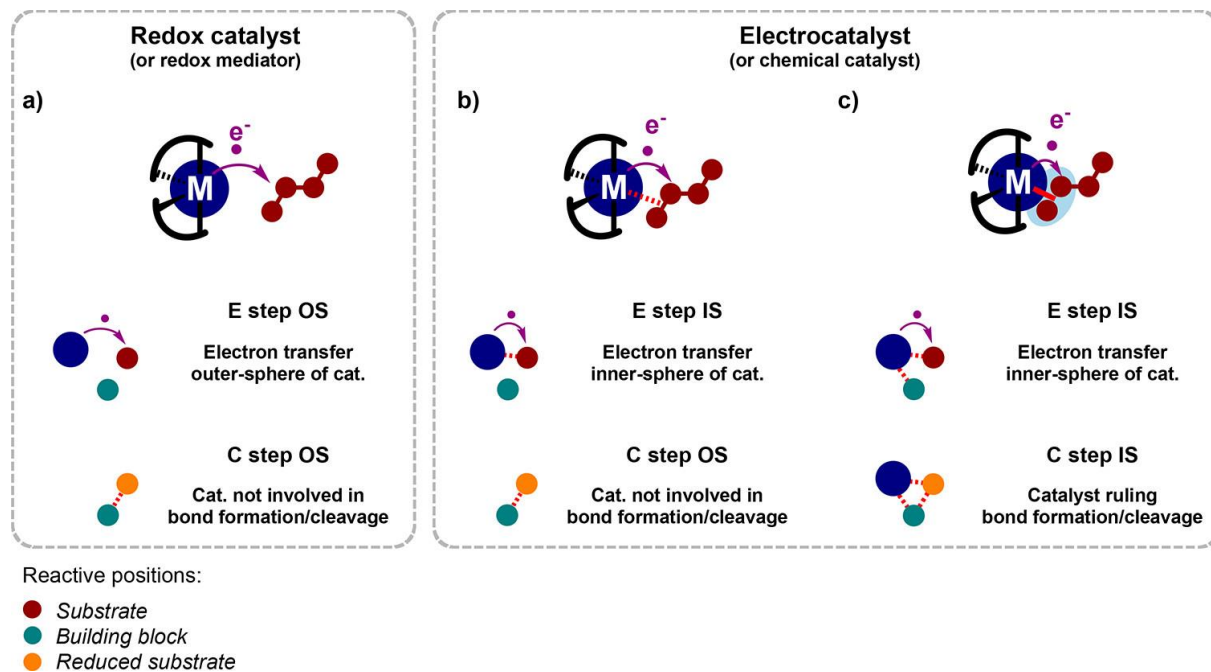


**Figure 3.1. 3** Redox catalyst (a) versus electrocatalyst (b, c): schematic representation of electron transfer modes and involvement in the electrochemical (E) and chemical (C) steps. Cat., catalyst; IS, inner sphere; OS, outer sphere (Reused from <sup>64</sup> with permission (CC BY 4.0))

## 4 APPLICATIONS

### 4.1 Asymmetrically Difunctionalized 1,1'-Ferrocenyl Metalloligands and Their Transition Metal Complexes

#### 4.1.1 Introduction

In recent years, the primary focus of the attention of more than a few research groups has been on the development of stimuli-responsive ligands as well as analyses of the transition metal complexes associated with these ligands.<sup>65, 66</sup> Alterations in the ligand's ligating capabilities that are ideally reversible can be caused by the application of external stimuli such as irradiation with light, protonation, or redox-switching.<sup>67, 68</sup> Many other redox-active ligands and (catalytically active) multimetallic complexes have been developed, the majority of which are based on ferrocenyl (Fc)-containing mono- or multidentate ligands.<sup>69-71</sup> These developments were inspired by the pioneering work that Wrighton and co-workers did on cobaltocene-based redox-switchable catalysts.<sup>72</sup> Within this framework, Breher et al. decorated Ferrocene with phosphines, N-heterocyclic carbenes (NHCs), and mesoionic carbenes (MICs).

In most instances, the cyclopentadienyl (Cp) rings of the ferrocenyl entities that make up ferrocene-based ligands are either monofunctionalized at one ring or symmetrically difunctionalized at both Cp rings. This is one characteristic that is shared by ferrocene-based ligands.<sup>70, 71</sup> Despite the fact that derivatives with a donor group only at one of the Cp rings are predestined for further functionalization on the other Cp ring (1,1'-difunctionalization), there are almost no examples known in the literature of such systems being targeted to be investigated in the field of redox-switchable catalysis. If the Cp entities had additional functional groups, then fine-tuning of the catalytic system would be much simpler. It is possible that a lack of acceptable synthesis techniques is to blame for the fact that the literature only describes a handful of examples of asymmetrically 1,1'-difunctionalized ferrocene derivatives.<sup>73-75</sup> The majority of them have issues such as low yields, side reactions, and low tolerance of functional groups.<sup>76-78</sup>

In this work,<sup>79</sup> Breher et al. proposed a straightforward synthetic method that may be utilized to generate asymmetrically 1,1'-difunctionalized ferrocene derivatives through the incorporation of

extra functional groups. With the assistance of cyclic voltammetry, the influence of the extra groups is investigated using a collection of transition metal complexes as a test subject.

In this thesis the accompanying DFT calculations are presented and discussed in comparison with the experimental results. The calculations on the proposed reaction path have been carried out on model complexes by Nils Frank in his bachelor thesis.<sup>80</sup> My contribution was the structure optimizations for the full clusters and the investigation of the ionization potentials.

### 4.1.2 Computational Details

All density functional theory (DFT) calculations were performed with the program package TURBOMOLE applying different types of density functionals.<sup>81</sup>

The vertical Ionization Potentials (IPs) were approximated on three different levels: (a) by Kohn-Sham orbital energies, (b) by  $\Delta$ DFT, i.e. the difference of the DFT energies of the neutral ground state and ground state of the cation (structure of the neutral molecule), and (c) quasi-particle energies from eigenvalue only quasi-particle self-consistent GW (evGW) calculations.<sup>34</sup> The adiabatic ionization potential was obtained as in (b) but taking the energy of the optimized structure for the cation. With (b) only the first IP can be obtained, while (a) and (c) allow us to distinguish between ionization at Ni and Fe by a Mulliken population analysis of the ionized orbital.

Reaction paths were obtained from calculations on model complexes, which are shown in Figure 4.1.1, where the Fe in the ferrocenyl unit was inactivated in a fixed oxidation state Fe(II) and Fe(III), respectively, by substituting it with a large core pseudopotential with the correct charge state.

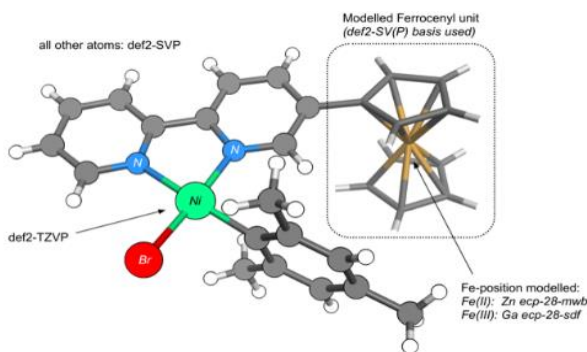


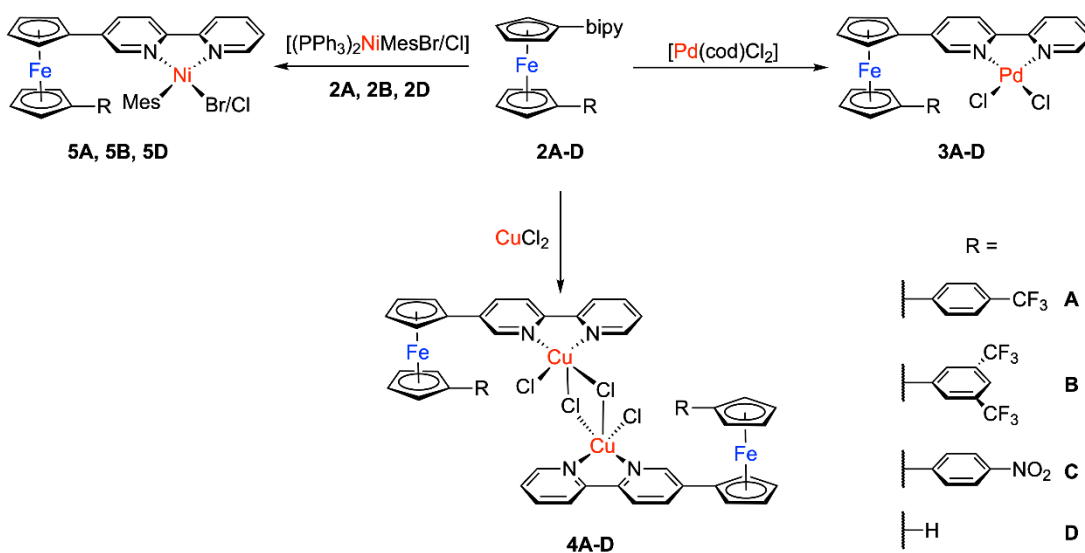
**Figure 4.1. 1** Overview about the employed catalyst models for 5D, proposed by Nils Frank.

Transition states were preoptimized by a reaction path search from Plessow<sup>82</sup> and then determined by trust region image optimizations.<sup>83</sup>

Within the here used model, the Fe(II) centre inside the ferrocenyl unit was replaced with the effective core potential ecp-28-mwb for Zn<sup>84</sup> and for modelling a Fe (III) centre with the effective core potential ecp-28-sdf for Ga<sup>85</sup> – both without basis sets and auxiliary basis sets to mimic the ionic character. A def2-TZVP basis set was used for the Ni atom, a def2-SV(P) basis was used for the rest of the ferrocenyl unit. A def2-SVP basis set was employed for all other atoms.<sup>86, 87</sup> Dispersion corrections to DFT energies were taken into account using Grimme's D3 empirical method with Becke-Johnson damping D3(BJ).<sup>88, 89</sup> The structures for the calculation of the IPs were searched and calculated with the B3LYP functional.<sup>90</sup> The energetic reaction pathways were explored with the BP86 functional.<sup>91</sup> All calculations were carried out in the gas phase.

#### 4.1.3 Results and Discussion

The complexes with metalloligands **2A-D** shown in Scheme 4.1.1. were synthesized in the Breher group. These complexes contain the metals Pd, Cu, and Ni, respectively.



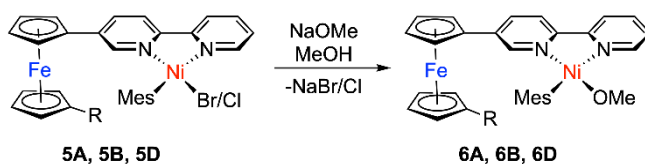
**Scheme 4.1. 1** Synthesis of the Pd, Cu and Ni complexes of the metalloligands **2A-D**.

## Application (I)

Motivated by the hypothesis that square-planar compounds containing aryl and alkoxide groups exhibited reductive elimination reactions when the nickel was oxidized, the synthesized ligands were reacted with a nickel precursor containing a mesityl group called  $[(PPh_3)_2Ni(Mes)Br/Cl]$ . As shown in scheme 4.1.1, this reaction was carried out in order to produce the desired product.

As we mentioned, after oxidation of the nickel atom from Ni (II) to Ni (III), it is well known that nickel complexes containing aryl and alkoxide groups undergo reductive elimination reactions. Breher and coworkers have also synthesized the analogue methoxides **6A**, **6B**, and **6D**, which are shown in scheme 4.1.2.

Since the Ni complexes are the primary focus of our calculation, we will discuss these complexes, which are referred to as **5A**, **5D**, and **6D** respectively.



**Scheme 4.1. 2** Synthesis of the methoxides **6A**, **6B** and **6D**.

Cyclic voltammetry was employed by MacMillan and his colleagues in their study of nickel-catalyzed cross-coupling reactions to analyze the reductive elimination step.<sup>92</sup> They used compounds that were quite similar to those used in the study. The goal of this work, which was inspired by previous research, is to impact and optimize catalytic activities such as reductive eliminations by fine-tuning ligands with the assistance of functional groups that have been introduced. We used DFT methods to analyze the various steps for mechanistic plausibility based on the suggested catalytic cycle that is displayed in Figure 4.1.2.

## Application (I)

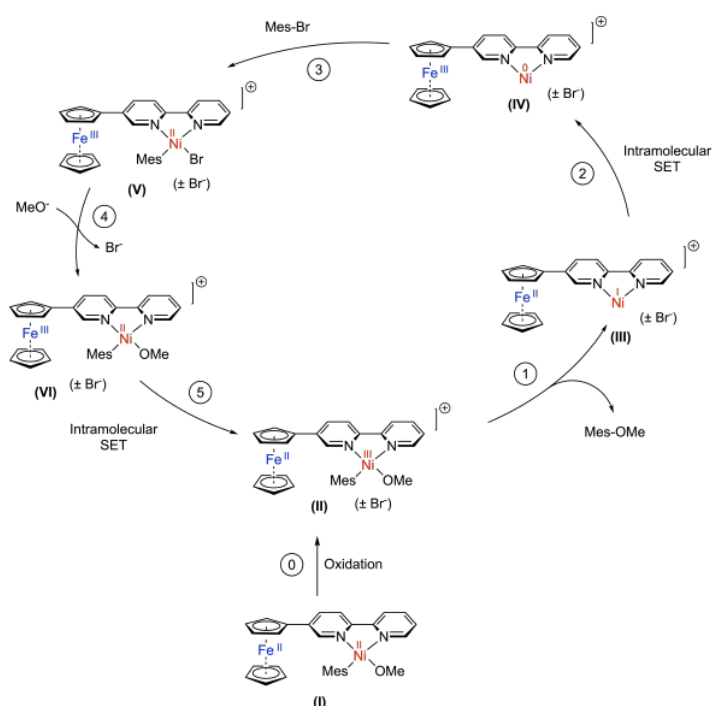


**Figure 4.1. 2** Proposed mechanism by Breher et al.,  $\pm \text{Br}^-$  indicates the possibility binding of a bromide to the cationic complex. (Reused from <sup>80</sup> with permission)

Complexes **6A**, **6B**, and **6D** were employed to investigate the possibility of a bimetallic cooperative catalysis. As we previously discussed, these complexes were inspired by MacMillan's nickel-catalyzed cross-coupling processes. In a first step, the reductive elimination was confirmed experimentally by chemical oxidation of the compounds on a preparative scale and following Gas chromatography–mass spectrometry (GC-MS) measurements where the formation of the generated aryl ether 2,4,6-trimethylanisole was verified. However, it quickly turned out that under the conditions used for a catalytic system (12h, room temperature), no turnover can be observed.

To further support the electrochemical findings on the one side, and to find an explanation of the inactivity of the bimetallic complexes in catalytic cross-coupling on the other, quantum chemical calculations were performed on **5A**, **5D**, and **6D**. Initially, we aimed to obtain information about the differences in the ionization potential of Ni(II) and Fe(II). To this end, the gas phase ionization

## Application (I)

---

potentials (IP) of **5D** and **6D** were calculated and the site of ionization within the molecule was located. The results were compared to calculations on model systems **5D\*** and **6D\***. In these model systems, Fe was substituted by an all electron pseudopotential so that ionization could only take place at Ni. For further comparison, a Ni fragment of **5D** where ferrocenyl was substituted by hydrogen was used and all ionization potentials were compared to ferrocene. The results are summarized in Figure 4.1.3.

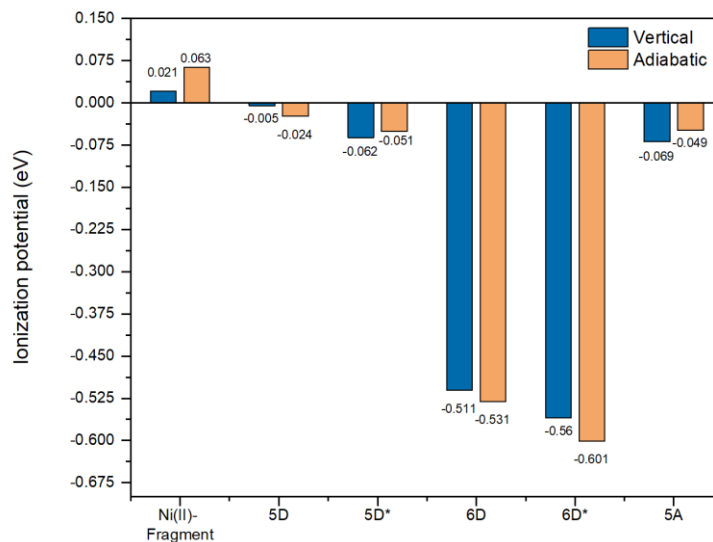


**Figure 4.1. 3** Ionization potential (B3LYP) with respect to the calculated values for ferrocene (6.363 eV vertical and 6.228 eV adiabatic)

The calculated ionization potentials of **5D** and **5A** were very similar and close to the value of ferrocene. Only slightly more negative values were found for **5A** (-0.069 eV vertical; -0.049 eV adiabatic) as compared to **5D** (-0.005 eV vertical; -0.024 eV adiabatic), which show the same tendency although much less pronounced as expected from the electrochemical findings in solution ( $\Delta E^0_{1/2}(\mathbf{5A}/\mathbf{5D}) = 106$  mV). The same holds for a Ni(II) fragment of the complex. Interestingly, according to the spin density which is shown in Figure 4.1.4, ionization takes mainly place at Ni(II).

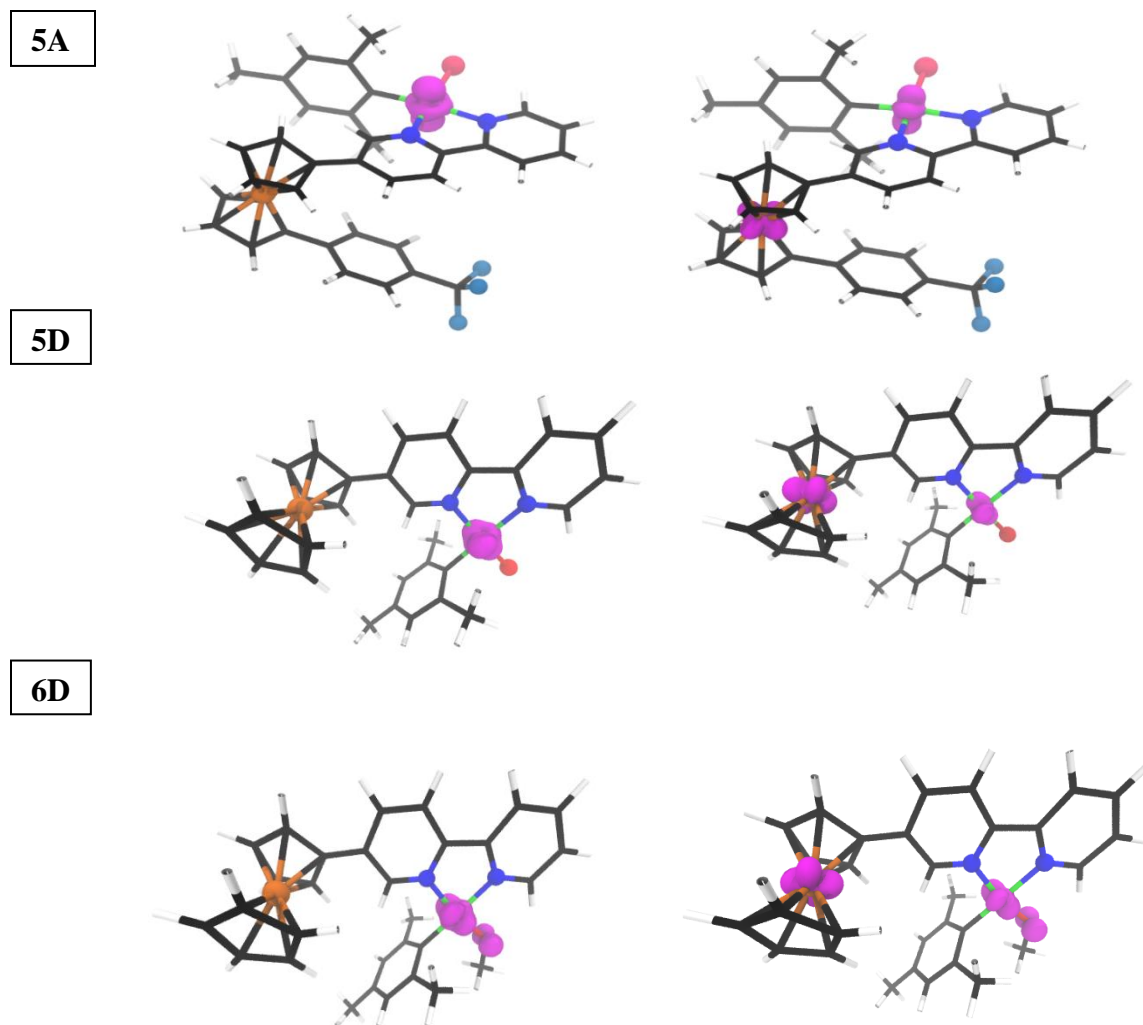


**Figure 4.1. 4** Spin density of vertical ionized **5A**, **5D**, and **6D**, basis set: def2-TZVP , isovalue= 0.01. lhs: B3LYP; rhs: BP86. Other hybrid functionals behave similar to B3LYP, other GGAs similar to BP86.

Similar trends have already been observed by Breher et al. for related complexes of ferrocenyl-functionalized *N*-donor ligands.<sup>93</sup> For hybrid functionals, the spin density is completely localized on Ni. In the case of GGA (general gradient approximation) functionals, there is a significant contribution on Fe. In **6D**, the ionization is favored by about 0.5 eV compared to ferrocene and the spin density shows contributions on the oxygen of OMe. These results are supported by quasi particle energies obtained by GW calculations, which allow to differentiate between the lowest ionization from a Ni and a Fe orbital, the results are summarized in Table 4.1.1- 4.1.5.

## Application (I)

**Table 4.1. 1** Comparison of the vertical ionization potential and quasi particle energies of the highest Ni and Fe dominated orbital, respectively, for **5D** (**5A** for comparison) and **6D** (def2-TZVP basis set). The Mulliken populations refer to the Ni and Fe contributions in the respective orbitals.

System	Functional	Vertical ionization potential / eV	Ni / Fe (Mulliken population)	Ni / Fe (orbital energy / eV)	Ni / Fe (quasiparticle energy / eV)
<b>5D</b>	B3LYP	6.358	0.8 / 0.8	5.530 / 5.714	6.420 / 6.234
	PBE0	6.269	0.7 / 0.8	5.956 / 6.256	6.498 / 6.341
	TPSS	6.208	0.9 / 0.6	4.315 / 4.675	6.541 / 6.412
	TPSSH	6.358	0.9 / 0.7	4.935 / 5.245	6.401 / 6.364
<b>5A</b>	B3LYP	6.294	0.8 / 0.8	5.589 / 5.917	6.477 / 6.367
	PBE0	6.310	0.7 / 0.8	5.998 / 6.415	6.560 / 6.502
<b>6D</b>	B3LYP	5.852	0.4 / 0.8	4.802 / 5.616	5.997 / 6.140
	PBE0	5.951	0.4 / 0.6	5.162 / 6.153	6.084 / 6.596
	TPSS	5.744	0.5 / 0.4	3.907 / 4.525	5.982 / 6.376
	TPSSH	5.845	0.5 / 0.7	4.373 / 5.118	5.928 / 6.258

Ionization potentials (IPs) for each of the various density functionals are compared to one another in Table 4.1.1. For **6D**, the IP is significantly lower. In addition, the results of the Mulliken populations demonstrate that the spin density can be found primarily on Ni for all hybrid functionals; however, for GGA functionals, it is shown to be more dispersed.

The findings of GW quasiparticle energies<sup>34, 94</sup> are summarized in Tables 4.1.2-4.1.5. Comparisons are made between the energies of orbitals and the energies of GW quasiparticles for the most highly occupied orbitals, including those with considerable metal occupation.

## Application (I)

---

**Table 4.1. 2** Vertical and adiabatic IPs for different complexes and density functionals. Mulliken contributions of Ni and Fe to the spin density. Basis set: def2-TZVP

Systems	Vertical IP (eV)	Adiabatic IP (eV)	Mulliken population
<b>5D</b>			
<b>B3LYP</b>	6.358	6.204	1.17(Ni)
<b>PBE0</b>	6.269	6.149	1.33(Ni)
<b>M06</b>	6.806	6.493	1.16(Ni)
<b>PBE</b>	6.199	6.124	0.45(Ni) 0.45(Fe)
<b>BP86</b>	6.356	6.202	0.43(Ni) 0.45(Fe)
<b>6D</b>			
<b>B3LYP</b>	5.852	5.697	0.89(Ni)
<b>PBE0</b>	5.951	5.739	0.98(Ni)
<b>M06</b>	6.306	6.008	0.87(Ni)
<b>BP86</b>	5.933	5.798	0.32(Fe) 0.49(Ni)
<b>5A</b>			
<b>B3LYP</b>	6.294	6.179	1.16(Ni)
<b>PBE0</b>	6.310	6.138	1.33(Ni)
<b>BP86</b>	6.330	6.156	0.46(Ni) 0.50(Fe)

---

## Application (I)

---

**Table 4.1. 3** IPs based on KS orbital energies and evGW quasi partical energies as well as Mulliken populations for the lowest orbitals of **5D**.

<b>5D</b>	<b>IP (orbitals) (eV)</b>	<b>IP (evGW) (eV)</b>	<b>Mulliken populations</b>
<b>B3LYP</b>	6.122	6.656	0.908 (Ni)
	5.900	7.666	0.008 (Ni) 0.008 (Fe) 0.15 (C) 0.25 (C)
	5.768	7.150	0.324 (Ni) 0.456 (Fe) 0.5 (Br)
	5.759	6.345	0.015 (Ni) 0.796 (Fe)
	5.714	<b>6.234</b>	0.814 (Fe)
	5.530	6.420	0.837 (Ni) 0.083 (Br)
	5.469	6.592	0.497(Ni) 0.42 (Br)
	5.363	6.992	0.063 (Ni) 0.22 (C) 0.15 (Br)

## Application (I)

---

**Table 4.1. 4** IPs based on KS orbital energies and evGW quasi partical energies as well as Mulliken populations for the lowest orbitals of **6D**.

<b>6D</b>	<b>IP (orbitals) (eV)</b>	<b>IP (evGW) (eV)</b>	<b>Mulliken population</b>
B3LYP	5.851	6.559	0.78 (Ni)
	5.813	7.370	0.13 (Ni) 0.20 (C)
	5.659	6.197	0.83 (Fe)
	5.616	6.140	0.81 (Fe)
	5.348	6.829	0.16 (Ni) 0.24 (C)
	5.217	6.086	0.88 (Ni) 0.05 (O)
	4.802	<b>5.997</b>	0.40 (Ni) 0.42 (O)

---

## Application (I)

---

**Table 4.1. 5** IPs based on KS orbital energies and evGW quasi partical energies as well as Mulliken populations for the lowest orbitals of **5A**.

<b>5A</b>	<b>IP (orbitals) (eV)</b>	<b>IP (evGW) (eV)</b>	<b>Mulliken population</b>
<b>B3LYP</b>	6.172	6.742	0.88 (Ni)
	6.051	7.781	0.01 (Fe) 0.24 (C)
	5.948	6.386	0.81 (Fe)
	5.917	6.367	0.79 (Fe)
	5.811	7.188	0.36 (Ni) 0.48 (Br)
	5.589	6.477	0.81 (Ni) 0.05 (Br)
	5.531	6.807	0.38 (Ni) 0.41 (Br)
	5.430	6.887	0.20 (Ni) 0.25 (Br) 0.16 (C)

---

## Application (I)

Although they were treated by a slightly different basis set, the IPs of the model complexes **5D\*** and **6D\*** were similar to the results for **5D** and **6D** indicating that they are appropriate for the investigation of the transition states and barriers for the reductive elimination and the oxidative addition. A second limitation of the model is that solvent effects are neglected, which can stabilize various species to different extents. The following combinations of oxidation states were probed: Ni(II)/Fe(II) and Ni(II)/Fe(III) as illustrated in Figure 4.1.5 as well as Ni(III)/Fe(II) and Ni(III)/Fe(II) with additional Br<sup>-</sup> coordinating the Ni site which is shown in Figure 4.1.6. Several conclusions can be drawn from the reaction profiles depicted in Figure 4.1.5 and Figure 4.1.6:

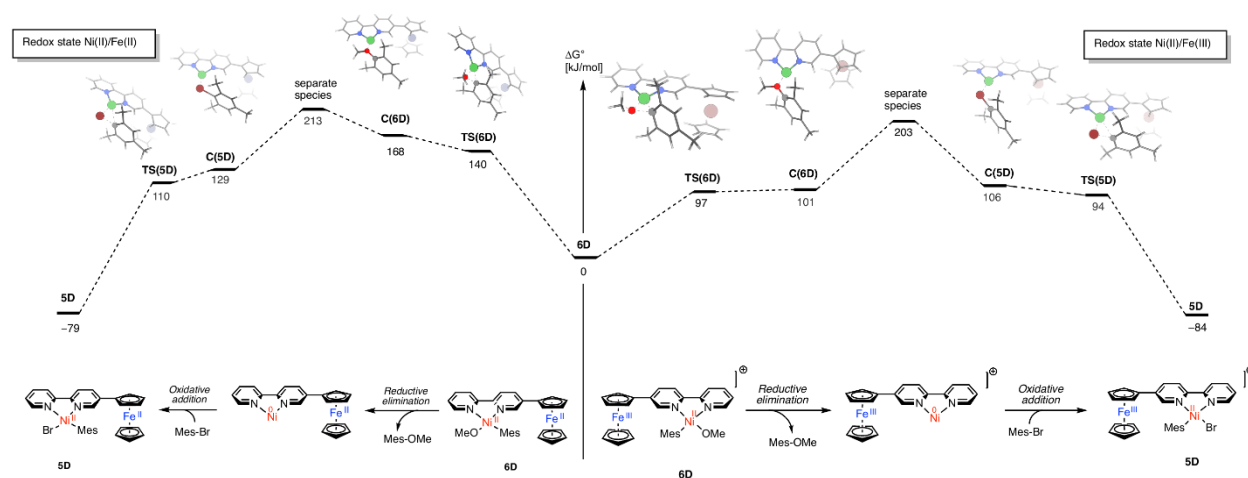


**Figure 4.1. 5** Gibbs free energy profile for a catalyst in oxidation states Ni(II)/Fe(II) and Ni(II)/Fe(III). All potentials include the energy of Mes-OMe and Mes-Br (one interacting with the catalyst, the other one infinitely separated) in order to limit changes in the interaction energy between substrate and catalyst. Separate species means that Mes-OMe and Mes-Br are both at infinite distance.

## Application (I)

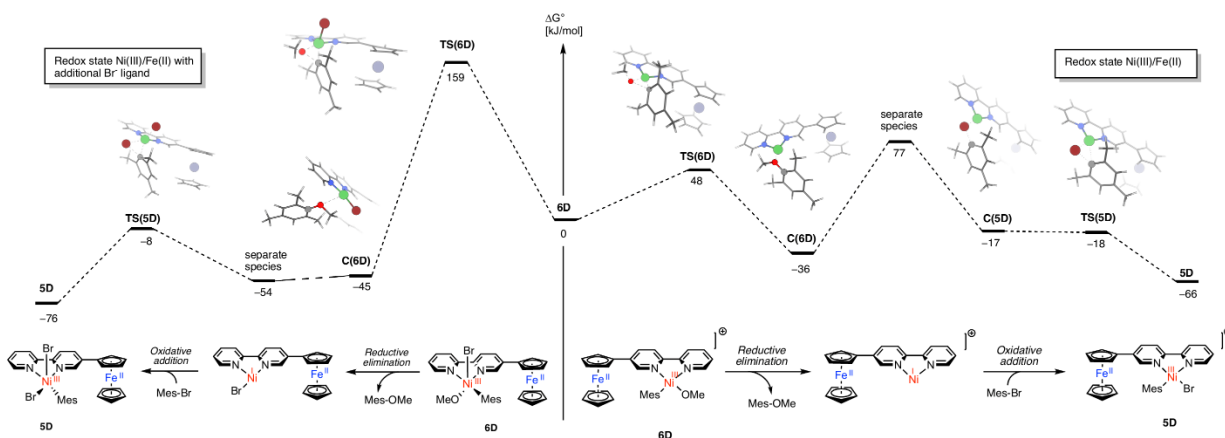


**Figure 4.1. 6** Gibbs free energy profile for a catalyst in oxidation states Ni(III)/Fe(II) with and without an additional Br<sup>-</sup> anion coordinating at the Ni site. All potentials include the energy of Mes-OMe and Mes-Br (one interacting with the catalyst, the other one infinitely separated) in order to limit changes in the interaction energy between substrate and catalyst. Separate species means that Mes-OMe and Mes-Br are both at infinite distance.

Tables 4.1.6 - 4.1.8 provide a summary of the electronic energies and all thermodynamic parameters for the reductive elimination and oxidative additions taking into account various oxidation states of Ni and Fe, with and without Br anion.

# Application (I)

**Table 4.1. 6** Electronic energies and thermodynamic properties for reductive elimination.

Redox state	Species	Electronic energy [H <sub>e</sub> ]	Energy Correction [kJ/mol]	Entropy [kJ/(K·mol)]	Enthalpy [kJ/mol]	Gibbs Free energy [kJ/mol]	Gibbs free energy difference [kJ/mol]
Ni(III)/Fe(II)	<b>6D1</b>	-2854.526534	1122.51	3.99584	-7493434.42588547	-7494625.79	
	TS( <b>6D</b> )	-2854.506099	1121.06	4.00998	-7493382.22314709	-7494577.80	47.99
	C( <b>6D</b> )	-2854.534989	1130.02	4.06834	-7493449.11444858	-7494662.09	-84.29
	Separate species <sup>2</sup>	-2390.032924	548.84	3.77503	-6274480.12306151	-6275605.65	113.21
	Total Gibbs free energy difference						76.91
Ni(II)/Fe(III)	<b>6D</b>	-2855.536814	1126.80	4.00444	-7496082.6256894	-7497276.55	
	TS( <b>6D</b> )	-2855.485795	1123.52	4.11687	-7495951.95687233	-7497179.40	97.15
	C( <b>6D</b> )	-2855.490136	1128.77	4.08367	-7495958.10239299	-7497175.65	3.75
	Separate species <sup>2</sup>	-2390.997102	545.20	3.74063	-6277015.21225348	-6278130.48	101.94
	Total Gibbs free energy difference						202.84
Ni(II)/Fe(II)	<b>6D</b>	-2854.743965	1125.56	4.03123	-7494002.24183450	-7495204.15	
	TS( <b>6D</b> ) <sup>1</sup>	-2854.691266	1116.60	3.99557	-7493872.84099595	-7495064.12	140.03
	C( <b>6D</b> ) <sup>1</sup>	-2854.684081	1118.14	3.96844	-7493852.43715127	-7495035.63	28.49
	Separate species <sup>2</sup>	-2390.201159	543.24	3.75725	-6274927.42480490	-6276047.65	44.75
	Total Gibbs free energy difference						213.27
Ni(III)/Fe(II) with additional Br ligand	<b>6D</b>	-5428.898292	1134.67	4.09414	-14252435.3161443	-14253655.98	
	TS( <b>6D</b> )	-5428.841775	1123.47	4.0223	-14252298.1307266	-14253497.38	158.60
	C( <b>6D</b> )	-5428.911401	1138.50	4.14485	-14252465.9036741	-14253701.69	-204.31
	Separate species <sup>2</sup>	-4964.457792	554.76	3.82477	-13033626.6941399	-13034767.05	-8.59
	Total Gibbs free energy difference						-54.29

<sup>1</sup> A small residual imaginary frequency < 15 cm<sup>-1</sup> remained

<sup>2</sup> Not including 2-methoxy-1,3,5-trimethylbenzene (see below). Gibbs free energy of 2-methoxy-1,3,5-trimethylbenzene was only included in the calculation of the Gibbs free reaction energy in the last column.

## Application (I)

**Table 4.1. 7** Electronic energies and thermodynamic properties for oxidative addition.

Redox state	Species	Electronic energy [H <sub>e</sub> ]	Energy Correction [kJ/mol]	Entropy S [kJ/(K·mol)]	Enthalpy H [kJ/mol]	Gibbs Free energy G° [kJ/mol]	Gibbs free energy difference Δ <sub>r</sub> G° [kJ/mol]
Ni(III)/Fe(II)	Separate species <sup>3,1</sup>	-2390.032924	548.84	3.77503	-6274480.12306151	-6275605.65	
	<b>C(5D)</b>	-5313.620726	1022.22	4.04499	-13949886.5185699	-13951092.53	-93.56
	<b>TS(5D)</b>	-5313.626524	1016.47	3.97749	-13949907.4895228	-13951093.38	-0.85
	<b>5D</b>	-5313.642254	1022.45	4.01997	-13949942.8081285	-13951141.36	-47.98
	Total Gibbs free energy difference	-206.061606					-142.39
Ni(II)/Fe(III)	Separate species <sup>2</sup>	-2390.997102	545.2	3.74063	-6277015.21225348	-6278130.48	
	<b>C(5D)</b>	-5314.588584	1016.42	3.98143	-13952433.4272625	-13953620.49	-96.69
	<b>TS(5D)</b>	-5314.592727	1012.65	3.97347	-13952448.0754704	-13953632.77	-12.27
	<b>5D</b>	-5314.659830	1020.35	4.00626	-13952616.5535673	-13953811.02	-178.25
	Total Gibbs free energy difference	-346.257853					-287.21
Ni(II)/Fe(II)	Separate species <sup>2</sup>	-2390.201159	543.24	3.75725	-6274927.4248049	-6276047.65	
	Van-der-Waals Adduct <sup>1</sup>	-5313.786907	1012.21	3.99963	-13950332.8361343	-13951525.33	-84.35
	<b>TS<sup>1</sup></b>	-5313.792017	1010.54	4.01141	-13950347.9220953	-13951543.92	-18.60
	<b>5D<sup>1</sup></b>	-5313.874846	1016.22	3.93022	-13950559.7102439	-13951731.51	-187.58
	Total Gibbs free energy difference	-375.031978					-290.53
Ni(III)/Fe(II) with additional Br ligand	Separate species <sup>2</sup>	-4964.457792	554.76	3.82477	-13033626.6941399	-13034767.05	
	Van-der-Waals Adduct	-7887.881939	1012.63	4.03973	-20708618.9219414	-20709823.37	337.01
	<b>TS<sup>1</sup></b>	-7888.000911	1017.87	3.98404	-20708926.0433842	-20710113.88	-290.52
	<b>5D</b>	-7888.021047	1028.38	4.07067	-20708968.3989767	-20710182.07	-68.18
	Total Gibbs free energy difference	-85.091376					-21.70

<sup>3</sup> Not including bromo-1,3,5-trimethylbenzene (see below). Gibbs free energy of bromo-1,3,5-trimethylbenzene was only included in the calculation of the Gibbs free reaction energy in the last column.

**Table 4.1. 8** Electronic energies and thermodynamic properties for single species (used in calculation of the Gibbs free reaction energy above).

Species (for all redox states)	Electronic energy [H <sub>e</sub> ]	Energy Correction [kJ/mol]	Entropy [kJ/(K·mol)]	Enthalpy [kJ/mol]	Gibbs Free energy [kJ/mol]	Gibbs free energy difference [kJ/mol]
2-methoxy-1,3,5-trimethylbenzene	-464.435301	575.17	0.48967	-1218797.23444501	-1218943.23	-1218943.23
2-bromo-1,3,5-trimethylbenzene	-2923.530845	465.64	0.44008	-7675262.11464176	-7675393.32	-6456450.09

The reductive elimination seems only feasible on a Ni(III) center, as already shown in the literature.<sup>92</sup> Nevertheless, the envisioned bimetallic cooperative catalysis through the electrostatically modelled ferrocenyl-unit does not significantly lower the activation barrier (Figure 4.1.5), at least for this catalytic model system.<sup>95</sup>

In contrast to what is the existing literature,<sup>96</sup> our investigations show that an oxidative addition on a Ni(I) center is kinetically as well as thermodynamically achievable. This finding could motivate the development of cross-coupling cycles relying solely on the Ni(III)/Ni(I) redox couple. Furthermore, the additional coordination of a solution state Br<sup>-</sup> anion to the nickel unit raises the activation energies of the reductive elimination and oxidative addition dramatically (Figure 4.1.6). This self-poisoning of the active catalytic site gives a possible explanation as to why only stoichiometric and no catalytic turnover was observed experimentally. This result could stimulate the use of moderately coordinating pseudohalides, like aryl triflates, as coupling partners.<sup>97</sup>

Additionally, highly exergonic binding of the substrate Mes-Br and product Mes-OMe to a low-coordinate Ni atom could be interpreted as thermodynamic resting states limiting the turnover frequency.

#### 4.1.4 Conclusion

As a conclusion, Breher et. al. has developed a more straightforward synthetic method that can produce 1,1'-difunctionalized ferrocene derivatives with very high yields and the potential for a wide range of alternative substrates. This method opens up new possibilities for customizing redox-active ligand complexes. Additionally, different coordination compounds derived from the new pro-ligands and various palladium, copper, and nickel precursors complete the studies of this novel synthetic approach. In order to see the slight but notable differences caused by the

## Application (I)

---

application of various electron withdrawing groups, the electrochemical characteristics of the compounds under study were examined and thoroughly compared to one another. Afterward, the reductive elimination reaction of an aryl ether caused by oxidation of the matching methoxides proved the influence of the latter on the nickel complexes. Details regarding the reductive elimination and oxidative addition occurring on the Ni site (which are heavily dependent on the oxidation state and the complicated coordination) are revealed by our quantum chemical calculations. The failure to transfer the experimentally observed reductive elimination into a bimetallic catalytic system could be attributed to a number of factors.

### 4.2 Photocatalytic reduction of CO<sub>2</sub> by highly efficient homogeneous Fe<sup>II</sup> catalyst based on 2,6-bis(1,2,3-triazol-yl-methyl) pyridine. Comparison with analogues.

#### 4.2.1 Introduction

Solar light is the most abundant sustainable energy source on the planet, capable of converting carbon dioxide from the atmosphere into biomass through a process known as natural photosynthesis. However, due to human activity, the stability of the carbon cycle is disturbed, mainly due to climate alternations and global warming. Synthetic photosynthesis is another way to store energy. It uses a simple device to collect energy from the sun and turn it into the electrochemical potential for making gas.<sup>57, 98</sup>

Synthetic photosynthesis consists of many reactions, such as water splitting and carbon dioxide reduction. However, the frequent focal point lies in a critical step: the photoinduced electron transfer process.<sup>99-101</sup> We need a photosensitizer (PS) for harvesting solar light and a catalyst (CAT) for reducing carbon dioxide in synthetic photosynthesis; they can exist in homogeneous or heterogeneous. To close the catalytic cycle and regenerate the photosensitizer's ground state, we need an electron donor (e-D). In most cases, PS and CAT in homogeneous systems are transition metal-based, rather than organic-based.<sup>102, 103</sup> Because they can change their oxidation state, transition metals are powerful tools for the multi-electron reduction of carbon dioxide.<sup>60, 104</sup>

The photocatalytic reduction of carbon dioxide permits the use of a waste product as a starting material for organic chemical production. Used on a massive scale, this should re-balance the disturbed carbon cycle. Almost forty years of investigation have been dedicated to discovering new and environmentally friendly structures for accomplishing this aim. Only recently, efforts have been made to use this approach in an eco-friendlier way with the aid of using earth-abundant rather than noble-metal substances.<sup>105-107</sup> Transition metals from the 3d row like Mn, Fe, Co, and Ni can be used instead of rare and pricey metals such as Ru, Ir, and Re.<sup>108-110</sup> Even though the noble metal has great photochemical and electrochemical properties, 3d metals are becoming more and more popular.

Typically, 3d metals reveal two possible oxidation states, forming two-electron reduction products such as carbon monoxide, formaldehyde, or formic acid. In most cases, molecular hydrogen is a coproduct, and the selectivity varies.

A combination of CO and H<sub>2</sub> as products, additionally recognized as syngas, constitutes a chance to generate fuels in a more extraordinary ecological way,<sup>111</sup> both used as such (for fuel gas turbines)<sup>112</sup> or producing, for example, methanol through further reaction.<sup>113</sup> Efficient earth-abundant systems take advantage of catalysts based especially on iron and cobalt porphyrins<sup>114, 115</sup> and multi-pyridine-based ligands,<sup>116</sup> even though rare metal complexes are predominantly used as PS.

For example, photo-driven CO<sub>2</sub> reduction can happen with an entire noble-metal-free system, which was presented using iron catalysts with a combination of copper-based photosensitizers.<sup>117</sup> Especially, the known complex [Fe<sup>II</sup>(dmp)<sub>2</sub>(NCS)<sub>2</sub>] (where dmp is 2,9-dimethyl 1,10-phenanthroline) as a catalyst was effectively used with several heteroleptic Cu<sup>I</sup> complexes as photosensitizers.

Among all the transition metals of the first row, iron is the most inexpensive and the most plentiful in the earth's crust (56,300 ppm).<sup>118</sup> It is also a fascinating metal to construct environmentally friendly catalysts with, as its cost-effectiveness makes it attractive for massive-scale applications. Thus, we aim to use Fe<sup>II</sup> complexes that can be used as CAT in photo-driven CO<sub>2</sub> reduction.

Bizzarri and coworkers examined two of Fe<sup>II</sup> complexes with different ligands. They created a new heteroleptic iron complex using a tridentate 2,6-bis-(4-phenyl-1,2,3-triazol-1-yl-methyl) pyridine ligand, two isothiocyanates, and pyridine (py) (**1**, Figure 4.2.1). Furthermore, they prepared the corresponding cobalt<sup>II</sup>-based heteroleptic (CoL<sub>2</sub>(NCS)<sub>2</sub>py, **2**) complex and the two homoleptic complexes ML<sub>2</sub> (where M= Fe, Co) and compared their activities as catalysts in photocatalytic carbon dioxide reduction.

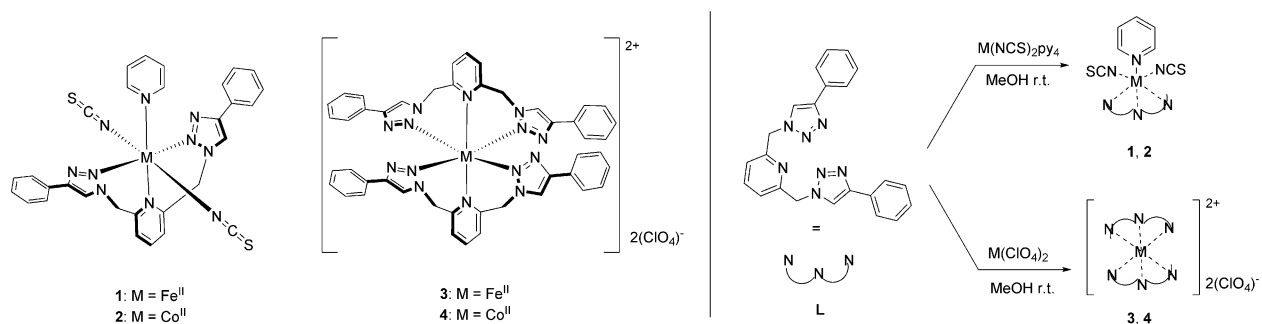


**Figure 4.2. 1** (Left) Chemical structures of the Fe<sup>II</sup> and Co<sup>II</sup> complexes investigated as CO<sub>2</sub> reduction CAT. (Right) Synthetic pathways of the heteroleptic (**1** and **2**) and homoleptic (**3** and **4**) complexes in methanol at room temperature.

They also tested the performance in a noble-metal-free system by employing them with a Cu<sup>I</sup> complexes (Cu(dmp)(DPEPhos), DPEPhos = bis[(2-diphenylphosphino)phenyl] ether)<sup>119</sup> as photosensitizers and 1,3-dimethyl-2-phenylbenzimidazoline (BIH) as an electron donor. The highly efficient FeL(NCS)<sub>2</sub>py CAT **1** for CO<sub>2</sub>-to-CO conversion showed a high selectivity, up to 70% for CO production over H<sub>2</sub>.

In particular, the photocatalytic system with the heteroleptic Fe-based CAT **1** produced CO with a turnover number of 576 after only 4 hours of irradiation at 420 nm, and the calculated quantum yields are satisfactory at 7.1%. These values are comparable to some of the best-reported approaches using fully earth-abundant systems with Fe-based catalysts. All of the other Fe- and Co-based complexes (**2**, **3** and **4**) also show thermodynamically feasible CO<sub>2</sub>-to-CO conversion as proved by electrochemistry and experiments.

Therefore, in this work, we focus on complex **1** to gain further insight into the mechanism of CO<sub>2</sub> reduction by **1**. We also studied iron-based homoleptic analogue **3** for comparison.

### 4.2.2 Computational Details

The calculations of the CO<sub>2</sub> binding energies were performed with the program package Turbomole<sup>81</sup> using density functional theory (DFT) with the B3LYP functional<sup>120</sup> and a high quality, triple- $\zeta$  basis set, def2-TZVP, with tightened SCF convergence ( $10^{-7}$ ) and enlarged grid size (3).

For the determination of reaction mechanisms and geometry optimizations of all energy minima and transition states, the r<sup>2</sup>SCAN-3c method,<sup>24</sup> which includes D4-dispersion<sup>121</sup> as well as the geometrical Counterpoise Correction (gCP),<sup>26</sup> and a modified version of the def2-TZVP basis set is used.<sup>122</sup> The r<sup>2</sup>SCAN calculations were performed with ORCA 5.0.2.<sup>123, 124</sup>

In order to obtain zero-point, enthalpy, and entropy corrections at 298.15 K, each structure was submitted to frequency calculations at the same level of theory. The energy minima possessed only positive normal modes, while transition states had exactly one imaginary frequency, which was carefully checked to be the one connected with the reaction path.

All calculations were carried out without considering solvents (isolated molecules in the gas phase).

### 4.2.3 Results and Discussion

Computational studies were conducted on CAT **1** to get insight into the catalytic cycle for CO<sub>2</sub> reduction. For comparison, calculations were also performed on the iron-based homoleptic analogue **3**, as they are the complexes that produced mainly CO from CO<sub>2</sub>.

To confirm that the thiocyanate ligands are binding the metal through the nitrogen, different linkage isomerisms (due to ambidentate ligand) were investigated with different spin states<sup>125</sup> for complex **1**, and the results are summarized in Table 4.2.1. As expected from the precursor NH<sub>4</sub>NCS employed, independently from the spin state, the N-bonded thiocyanate complex is energetically preferred to the S-bonded. The lowest energy was found for the triplet state, with a quintet state only slightly higher in energy.

**Table 4.2. 1** Calculation of electronic energy (a.u.) and relative energy (kJ/mol) of linkage isomerism concerning spin states in complex **1** using r<sup>2</sup>SCAN-3c method. The initial structure is the dianion A<sup>2-</sup>

Electronic energy (a.u.)				Relative energy (kJ/mol)			
-NCS		-SCN		-NCS		-SCN	
<b>N-Singlet</b>	-3054,62558	<b>S-Singlet</b>	-3054,60504	<b>N-Singlet</b>	61.38	<b>S-Singlet</b>	115.31
<b>N-Triplet</b>	-3054,64896	<b>S-Triplet</b>	-3054,63141	<b>N-Triplet</b>	<b>0.00</b>	<b>S-Triplet</b>	46.07
<b>N-Quintet</b>	-3054,64889	<b>S-Quintet</b>	-3054,62510	<b>N-Quintet</b>	0.17	<b>S-Quintet</b>	62.63

Moreover, the Mulliken spin populations for different multiplicities are given in Figure 4.2.2. This figure demonstrates that the spin density is concentrated primarily on the Fe atom, with some spreading to the ligand's 6-ring. In the case of the quintet state, the spin density reveals that there are 3.529 unpaired electrons on the Fe atom, with the remainder mostly located on the 6 ring of the ligand, whereas in the case of the triplet state, there are 3.348 unpaired electrons on the Fe atom and spins in opposite directions localized on the ligand's center. One unpaired electron on the Fe center and another, moving in the opposite direction, dispersed among the ligands characterize the singlet state.

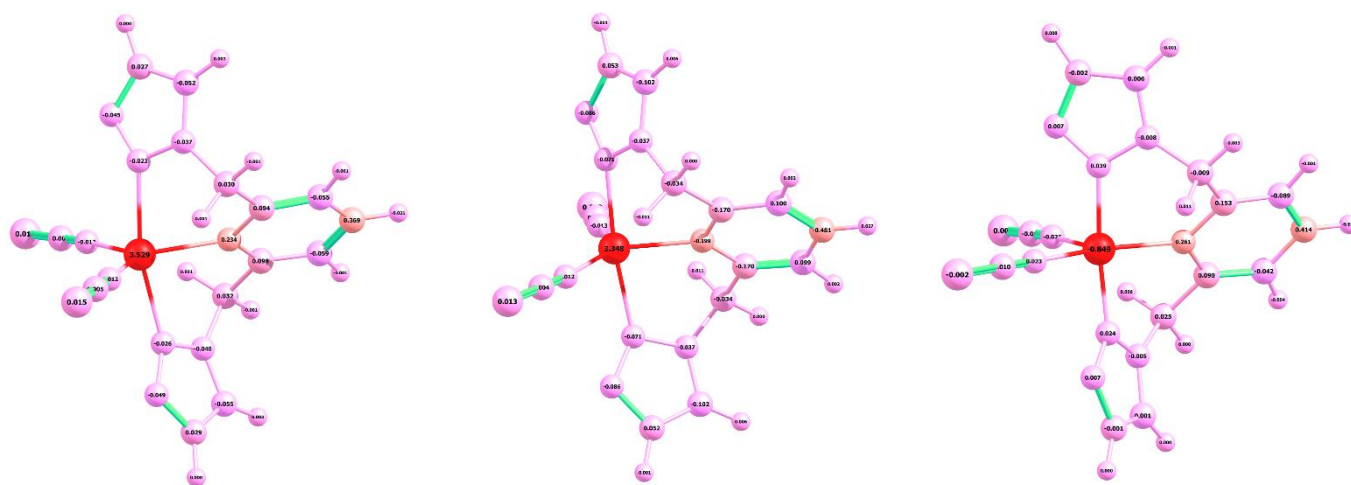


**Figure 4.2. 2** Mulliken spin populations on atoms for quintet (left), triplet (middle) and singlet states(right) of the dianion A<sup>2-</sup> of complex **1**, using r<sup>2</sup>SCAN-3c method.

It is important to note at this point that the quintet and the triplet are distinct from one another in terms of the coupling between the spins on ligand and Fe, but that their energies are extremely comparable, as shown in Table 4.2.1. Because of this, the quintet state will not be addressed again in the following sections.

The spin density plots for complex **1** for the different charges of complex (0,1-, and 2-) are shown in Figure 4.2.3. Plots of the most stable multiplicities for each charge have been created, and these plots show that the spin on the Fe atom is localized, whereas the spin on the ligand portion is only partly diffused.

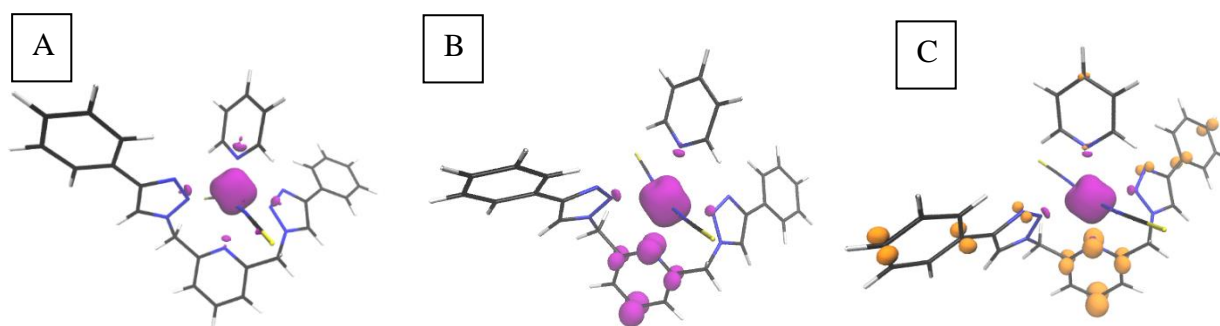


**Figure 4.2. 3** Spin density of Complex **1** (A)  $[\text{FeL}(\text{NCS})_2\text{Py}]^0$ , quintet state and (B)  $[\text{FeL}(\text{NCS})_2\text{Py}]^{1-}$ , sextet state, (C)  $[\text{FeL}(\text{NCS})_2\text{Py}]^{2-}$ , triplet state. Basis set: def2-TZVP, functional: B3LYP; isovalue:  $\pm 0.01$

Table 4.2.2 is a demonstration of Mulliken charges and spin populations over the atoms for various multiplicities for complexes 1 and 3 at various charge levels. When electrons are added to complexes 1 and 3, Mulliken charges demonstrate that these electrons do not proceed to the iron atom; rather, the ligand is reduced as a result of the addition of these electrons.

## Application (II)

**Table 4.2. 2** Electronic energy (a.u.), Mulliken spin population and charges of different spin multiplicities for complex 1 and 3. Basis set: def2-TZVP; functional: B3LYP

Complex	Complex Charge	Spin Multiplicity	Electronic energy(a.u.)	Mulliken spin populations		Mulliken charges		
				Fe	Ligands	Fe	Ligands	
<b>1</b>	0	Quintet	-3764.820576	3.77	0.20	0.59	-0.59	
		Singlet	-3764.804392	1.74	-1.71	-0.10	0.10	
	1-	Sextet	-3764.856755	3.78	1.17	0.56	-1.56	
		Doublet	-3764.837246	1.85	-0.82	0.208	-1.21	
	2-	Triplet	-3764.790273	3.69	-1.73	0.55	-2.55	
		Singlet	-3764.790202	1.73	-1.72	0.10	-2.10	
	<b>3</b>	2+	Singlet-Closed shell	-3804.905301			-0.15	2.15
		1+	Quartet	-3805.140961	3.40	-0.38	0.61	0.38
Doublet			-3805.121208	1.18	-0.16	0.16	0.83	
0		Triplet	-3805.259678	3.53	-1.48	0.61	-0.61	
		Singlet	-3805.239401	1.68	-1.64	0.20	-0.20	

As we discussed above, in electrochemical processes, the charge of the catalytic complex can easily change. Concerning CO<sub>2</sub> reduction, it is known that CO<sub>2</sub> can be adsorbed only on reduced

complexes for similar types of complexes.<sup>126, 127</sup> First, the energetics of charge changes of both complexes were studied, and the findings are presented in Figure 4.2.4.

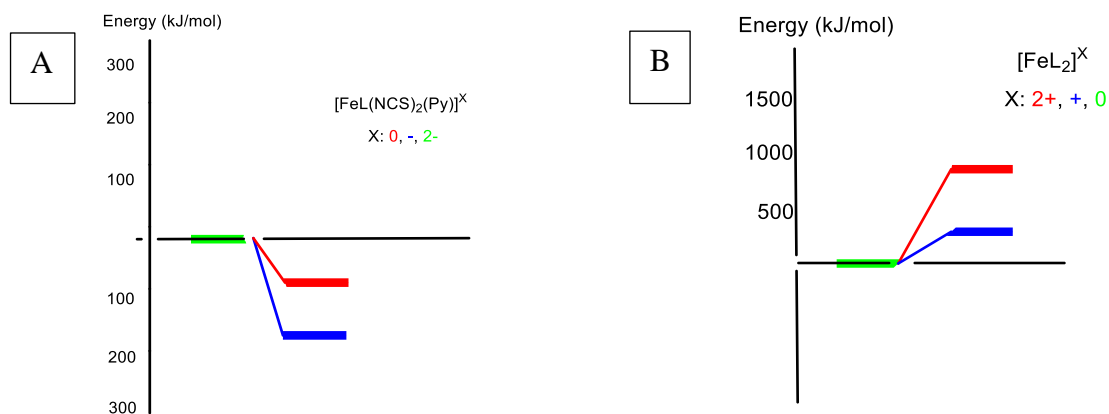


**Figure 4.2. 4** The relative energies of different oxidation states for (A) complex **1**, (B) complex **3**. Basis set: def2-TZVP; functional: B3LYP

In Table 4.2.3, Bizzarri et al. displayed the redox characteristics of the complexes in comparison to the internal reference Fc<sup>+</sup>/Fc pair. The initial reduction, which is essentially reversible, occurs at -1.01 V for complex **1** and at -0.91 V for complex **3**. This process involves the reduction of  $[\text{FeL}(\text{NCS})_2\text{Py}]$  to  $[\text{FeL}(\text{NCS})_2\text{Py}]^{1-}$ . At potentials of -1.76 V (complex **1**) and -1.63 V (complex **3**), the second irreversible reduction happens. The additional reduction procedure from  $[\text{FeL}(\text{NCS})_2\text{Py}]^{1-}$  to  $[\text{FeL}(\text{NCS})_2\text{Py}]^{2-}$  is responsible for this. It has already been shown that, computationally, that the complex is reducing and not Fe atom, and therefore the outcomes of the experiment strongly support this. Consequently, we talk about the complex's overall charge.

**Table 4.2. 3** Redox Potentials of the catalysts and their reduction states reacting with CO<sub>2</sub>

Sample	$E_{red}/V$	CO <sub>2</sub> catalytic current onset	Catalytic oxidation state
1	-1.01; -1.76	- 1.67	[FeL(NCS) <sub>2</sub> Py] <sup>2-</sup>
3	-0.91; -1.63	- 1.9	[FeL <sub>2</sub> ] <sup>0</sup>

We have already indicated that, in accordance with data from the literature,<sup>127</sup> it was observed that even when coordination on the metal center is geometrically allowed, CO<sub>2</sub> is only stable with two times reduced complexes. Figure 4.2.5 depicts the desorption of CO<sub>2</sub> in its oxidation states of 0 and 1- for complex **1**, and in its oxidation states of 2+ and 1+ for complex **3**.

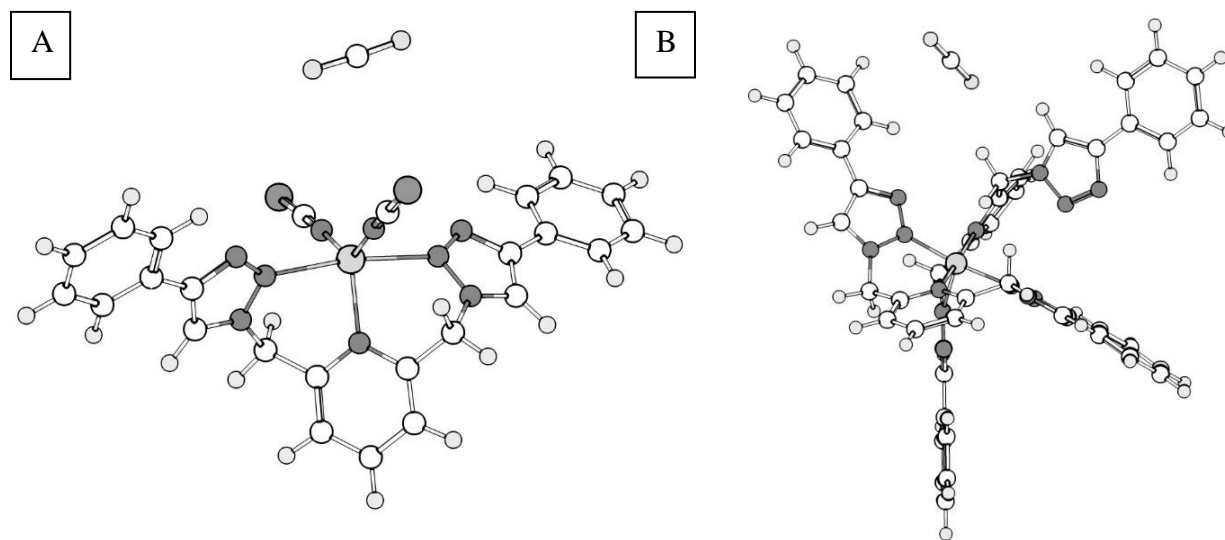


**Figure 4.2. 5** Desorption of CO<sub>2</sub> in Oxidation states of 0 and 1- for (A) Complex **1**, and Oxidation states of 2+ and 1+ for (B) Complex **3**. Basis set: def2-TZVP; functional: B3LYP

All of the complexes can only adopt an octahedral shape and undergo CO<sub>2</sub> adsorption after the release of a coordinating ligand. As can be seen in Figure 4.2.6, there are two main phases involved: first, pyridine ligand detachment, and then, CO<sub>2</sub> adsorption. It is contrasted how the

## Application (II)

complex behaves in its various oxidation states ( $x=0, -, \text{ and } 2-$ ). Adsorption of  $\text{CO}_2$  was possible only for  $[\text{FeL}(\text{NCS})_2\text{Py}]^{2-}$ . Dissociation of pyridine from  $[\text{FeL}(\text{NCS})_2\text{Py}]^{2-}$  requires 49 kJ/mol.

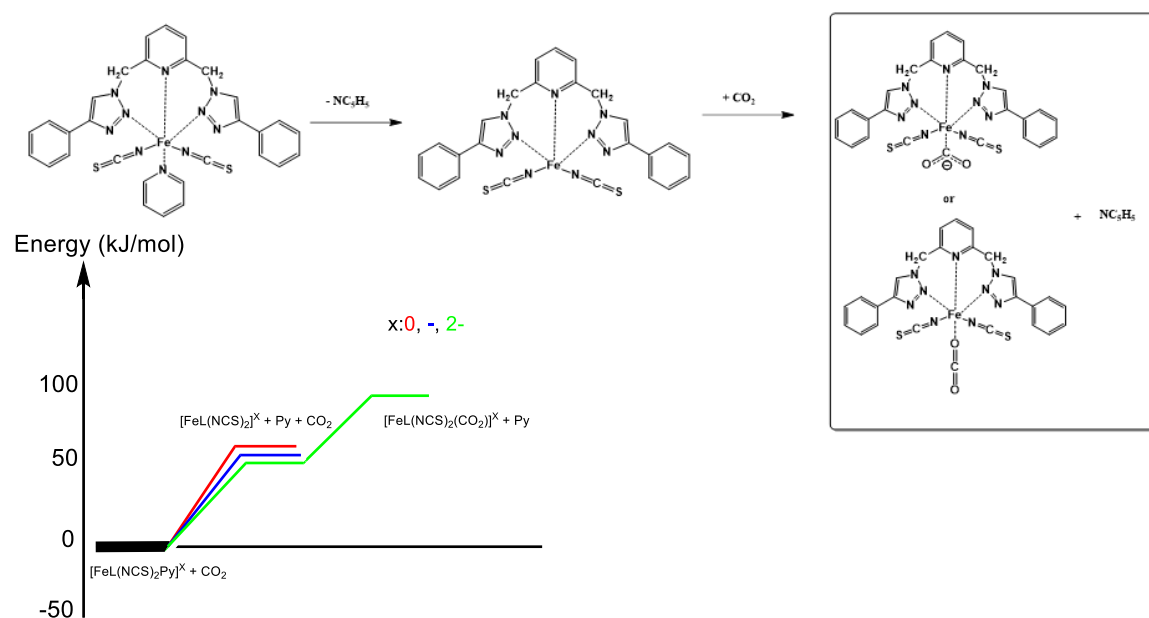


**Figure 4.2. 6** Complex 1: First step: Detachment of the pyridine ligand, Second step: Adsorption of  $\text{CO}_2$ . Different oxidation states ( $x=0, -, 2-$ ) of the complex are compared. Only for  $[\text{FeL}(\text{NCS})_2\text{Py}]^{2-}$ ,  $\text{CO}_2$  could be adsorbed. For all attempts (different starting structures) to adsorb  $\text{CO}_2$  for other oxidation states,  $\text{CO}_2$  moved away. Basis set: def2-TZVP; functional: B3LYP

The removal of NCS has been looked into in several charges involving complex 1. Figure 4.2.7 illustrates how much simpler dissociating NCS anion is now after the complex has been reduced twice.

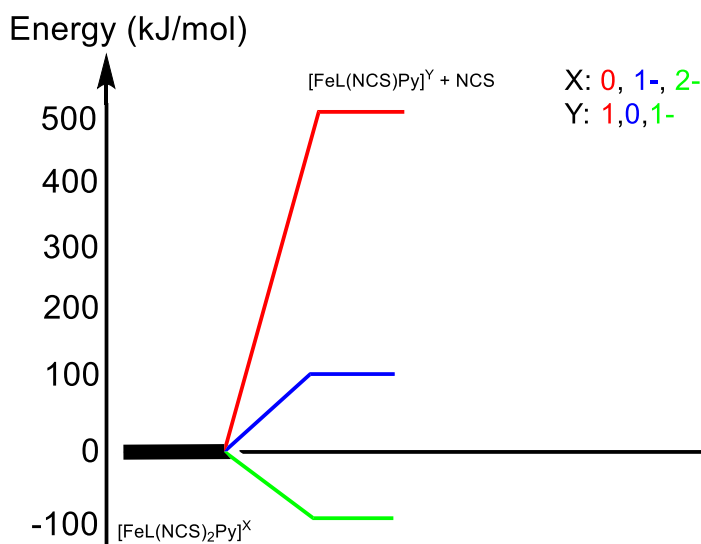


**Figure 4.2. 7** Binding energy of NCS on complex **1** (kJ/mol). Basis set: def2-TZVP, functional: B3LYP

We determined the binding energy of these ligands on complex **1** while taking into account various charges of the complex in order to compare the possibility of the removal of NCS anion in comparison to the removal of pyridine. Table 4.2.4 provides a summary of the findings.

**Table 4.2. 4** Binding energy of different ligands on complex **1** (kJ/mol). Basis set: def2-TZVP, functional: B3LYP

Charge of complex <b>1</b>	Binding energy (kJ/mol)	
	Py	NCS
0	52.56	596.46
1-	51.87	154.73
2-	49.12	-67.00

The charge of the complex logically has a significant impact on the binding energy of the NCS anion (while for neutral pyridine, it is almost independent and approx. 49 kJ mol). Although such desorption is thermodynamically advantageous for dianion, it is important to remember that the vast majority of polyanions in the gas phase are unstable due to this.

Similar to complex **1**, Figure 4.2.8 shows two phases for complex **3**, the first phase involves releasing one of the triazole rings to make the Fe center accessible. This transformation requires less energy (17 kJ/mol). The second phase is CO<sub>2</sub> adsorption, which can start right after two reduction complexes.

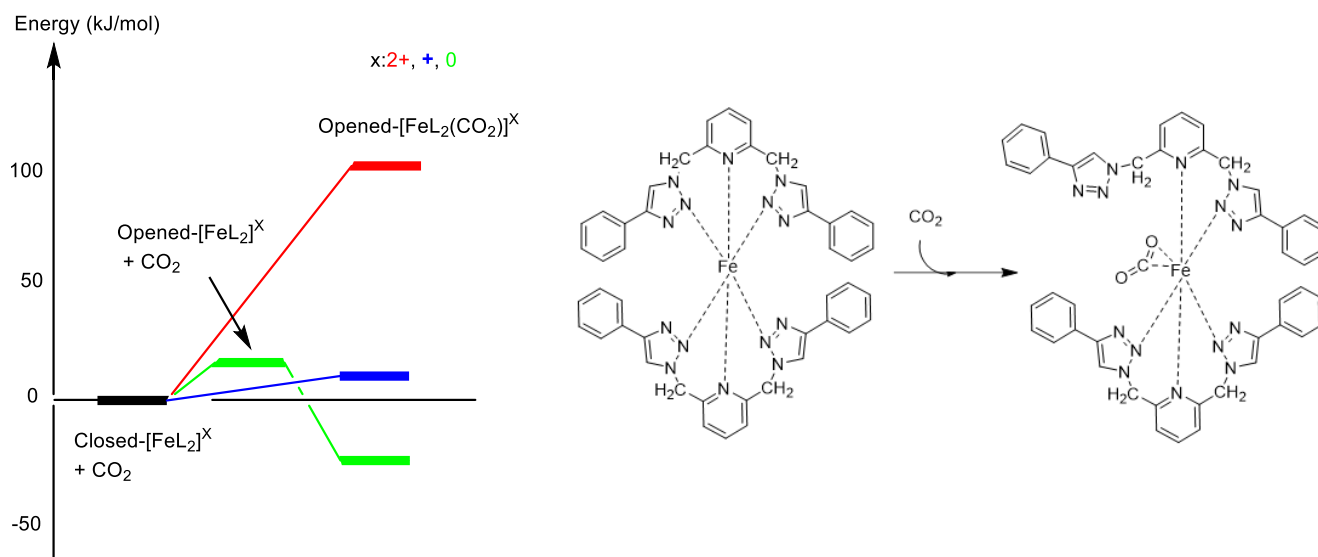


**Figure 4.2. 8** Complex **3**: First step: Detachment of the triazole ligand, Second step: Adsorption of CO<sub>2</sub>. Different oxidation states ( $x=2+$ ,  $1+$ ,  $0$ ) of the complex are compared. Only for  $[\text{FeL}_2]^0$  CO<sub>2</sub> could be adsorbed. For all attempts (different starting structures) to adsorb CO<sub>2</sub> for other oxidation states, CO<sub>2</sub> moved away. Basis set: def2-TZVP; functional: B3LYP

Furthermore, the adsorption of CO<sub>2</sub> on the iron centers of **1** and **3** was investigated. Figure 4.2.9 shows that CO<sub>2</sub> can be adsorbed on the metal centers in different ways, and the four most common, namely linear-O-“end-on” ( $\eta^1 \text{ o}$ ), “side-on” ( $\eta^2 \text{ c,o}$ ), C-bound “Y-on” ( $\eta^1 \text{ c}$ ) and bent-O-“end-on” ( $\eta^1 \text{ o bent}$ ) were tested.<sup>128, 129</sup>

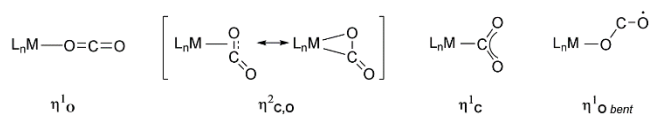


**Figure 4.2. 9** Mode of coordination of CO<sub>2</sub>.

The C-bound ( $\eta^1 \text{ c}$ ) “Y-on” configuration was found the most stable in a singlet state for complex **1** while CO<sub>2</sub> binds most preferably “side-on” ( $\eta^2 \text{ c, o}$ ) in a triplet state in complex **3**. The results are summarized in Table 4.2.5.

**Table 4.2. 5** Relative energy (kJ/mol) of different patterns for adsorption of CO<sub>2</sub> in different spin multiplicities, singlet and triplet for complex **1** and **3**.

Complex	Patterns	Spin multiplicity	Relative energy (kJ/mol)
<b>1</b>	$\eta^1 \text{ c}$	Singlet	0.00
		Triplet	0.48
	$\eta^1 \text{ o}$	Singlet	32.99
		Triplet	26.73
	$\eta^2 \text{ c,o}$	Singlet	0.19
		Triplet	0.96
<b>3</b>	$\eta^1 \text{ c}$	Singlet	19.29
		Triplet	16.41
	$\eta^1 \text{ o}$	Singlet	91.66
		Triplet	94.56
	$\eta^2 \text{ c,o}$	Singlet	15.44
		Triplet	0.00

Moreover, Figure 4.2.10 presents the spin density of complex **1** and **3** concerning the most favourable multiplicity. One can see that with adsorption of CO<sub>2</sub>, the unpaired electrons are mainly localized on the iron centers and to a lower extent on the adsorbed CO<sub>2</sub> as well as the ligand system.

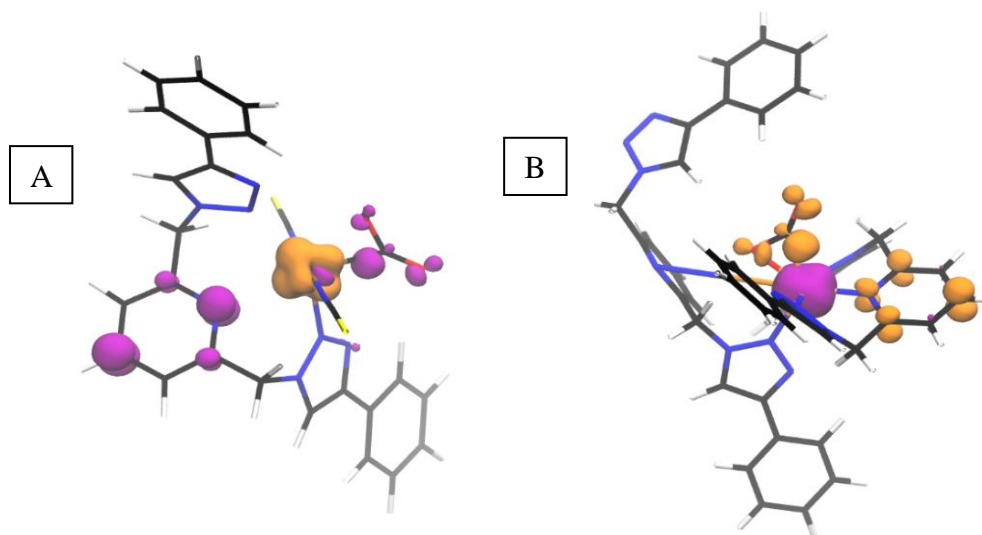


**Figure 4.2. 10** Spin density of (A) Complex **1**,  $[\text{FeL}(\text{NCS})_2\text{Py}]^{2-}$ , singlet state and (B) Complex **3**,  $[\text{FeL}_2]^0$ , triplet state.  $S^2$  for complex **1**: 1.2 and for complex **3**: 3.03. Basis set: def2-TZVP, functional: B3LYP; isovalue:  $\pm 0.01$

Table 4.2.6 provides the Mulliken charge and spin population values for Fe and  $\text{CO}_2$  of complex **1** and **3** in two times reduced form. In complex **1**, coupling these two spins antiferromagnetically results in a singlet state, and in complex **3**, three unpaired electrons are located on the Fe atom while one spin is on the  $\text{CO}_2$  in the opposite direction, giving us a triplet state, as can be seen from the Figure 4.2.10 where spin is located on Fe and to some extent on  $\text{CO}_2$ .

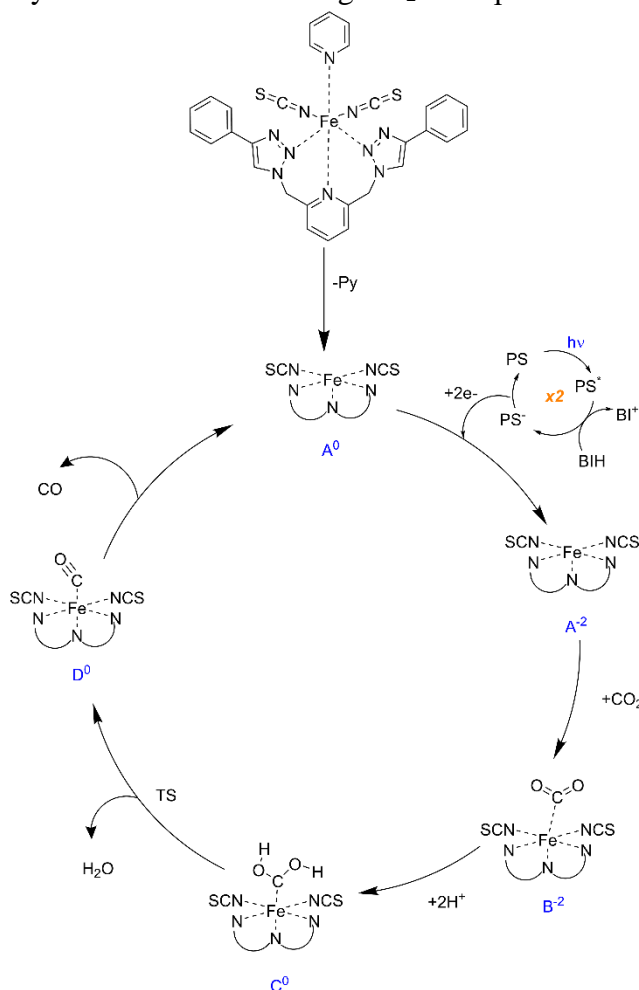
## Application (II)

---

**Table 4.2. 6** Mulliken charge and spin density of Fe and CO<sub>2</sub>; Basis set: def2-TZVP; functional: B3LYP

<b>Complex</b>	<b>Oxidation state of the complex</b>	<b>Atoms</b>	<b>Mulliken charge</b>	<b>Mulliken spin population</b>
<b>1</b>	<b>2-</b>	Fe	0.21	-1.21
		C	0.20	0.11
		O	-0.29	0.02
		O	-0.35	0.05
<b>3</b>	<b>0</b>	Fe	0.39	3.17
		C	0.17	-0.32
		O	-0.36	-0.06
		O	-0.34	-0.12

The proposed mechanism of CO<sub>2</sub> reduction with **1** as catalyst is shown on Scheme 4.2.1. The first step consists of the loss of the pyridine to reach the complex A<sup>0</sup>. In the next step, A<sup>0</sup> is photoinductively reduced by two PS<sup>-</sup> to A<sup>2-</sup> enabling CO<sub>2</sub> adsorption in “Y-on” conformation.



**Scheme 4.2. 1** Proposed mechanism for the photocatalytic CO<sub>2</sub> reduction with **1**.

The CO<sub>2</sub>-complex B<sup>2-</sup> formed is then doubly protonated to form the complex C<sup>0</sup>.<sup>130</sup> The weaker C-O bond can then break to free a molecule of water by overcoming the barrier of 160 kJ/mol in the singlet state (200+ kJ/mol for the triplet state), reaching D<sup>0</sup>. The desorption of CO as the last step was investigated, and the detachment energies are given in Table 4.2.7. This step is crucial because the CO-metal bond can be very stable,<sup>131</sup> causing overstabilization of this complex and thus, degradation of the active catalyst, limiting the reaction.

## Application (II)

The table 4.2.7 demonstrates that in order to recover  $A^0$  from complex **1**, CO must be released from the iron center. This process requires 137 kJ/mol of energy.

**Table 4.2. 7** Desorption energies in kJ/mol for CO from CAT **1** and **3**.

	CAT <b>1</b> (0, 1) [kJ/mol]	CAT <b>3</b> (0, 1) [kJ/mol]
Electronic energy	197.61	182.75
Thermal energy (ZPE)	187.44	168.82
Gibbs free energy	137.74	120.79

The reaction profiles obtained for **1** in different multiplicities are shown in Figure 4.2.11. The most favourable pathway is found to be in the singlet state, showing the lowest barriers. The most energy-demanding step is the proton transfer to form coordinated water (160 kJ/mol). The release of CO makes the reaction exothermic (-40 kJ/mol).

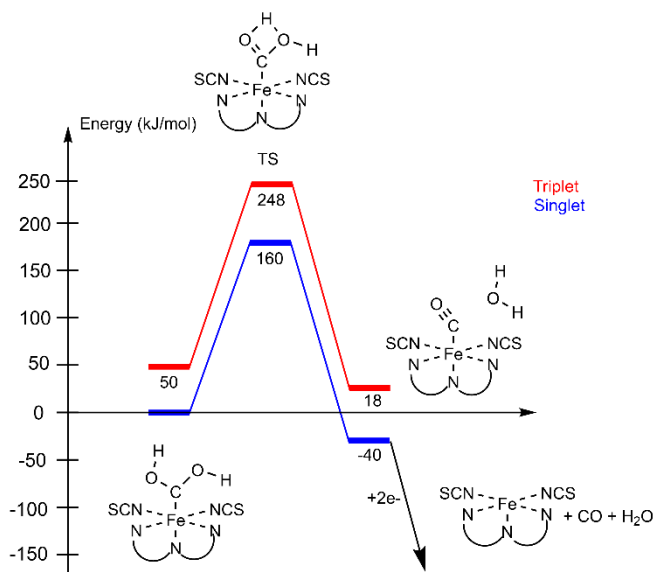
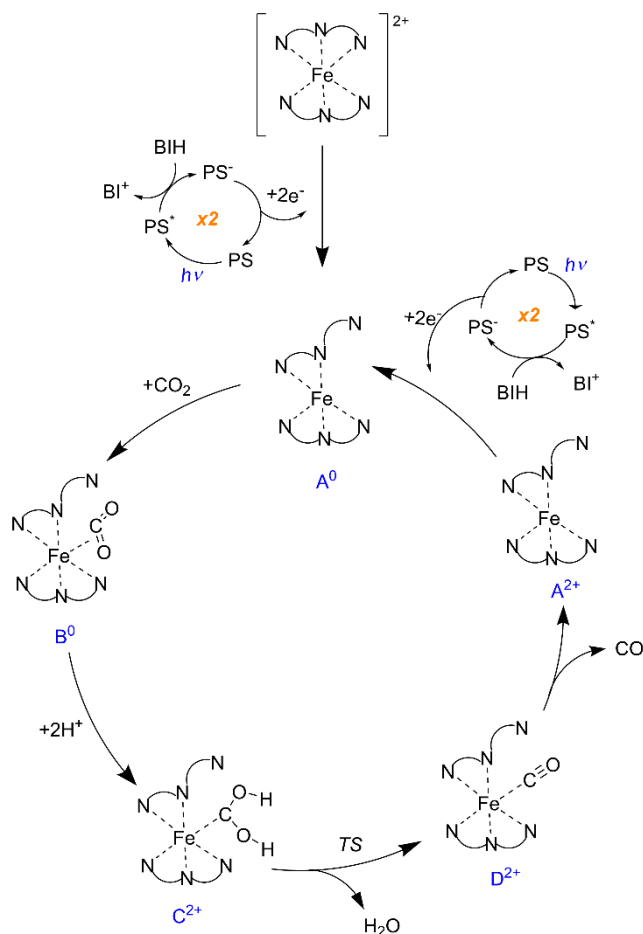


**Figure 4.2. 11** Energy diagram for CAT **1** in different multiplicities.

## Application (II)

---

Scheme 4.2.2 shows a similar mechanism for the reduction of CO<sub>2</sub> with **3** as the catalyst. Because of the neutral charge of the ligands, the charge of the different intermediates in the reaction with complex **3** is always higher (by a factor of 2) compared to complex **1**. The precursor **3** has a charge of 2+ that is reduced by the uptake of two electrons and opening the ligand to form A<sup>0</sup>. While active center of complex **3** is more hindered in comparison to one of the complex **1**, adsorption of CO<sub>2</sub> on it can be expected to be less probable. Even with slightly lower energy gained by the ligand-to-CO<sub>2</sub> exchange at the most reduced state, the equilibrium in the reaction conditions might be significantly shifted to “closed” unreactive forms. Contrary to complex **1** where CO<sub>2</sub> binds “Y-on” ( $\eta^1 \text{ c}$ ), CO<sub>2</sub> binds “side-on” ( $\eta^2 \text{ c, o}$ ) to the metal center.



**Scheme 4.2. 2** Proposed mechanism for the photocatalytic CO<sub>2</sub> reduction with **3**.

Finally, the catalytic cycle involving **3** follows the same last steps as for complex **1**. In the final stage, which is similar to the mechanism involving **1**, releasing CO requires 120 kJ/mol to regenerate A<sup>0</sup>, as indicated in table 4.2.7. The desorption of CO is slightly easier with **3** because of the sterically hindered structure of the molecule.

The reaction profiles obtained for **3** in different multiplicities are shown in Figure 4.2.12. As for **1**, the protonation pathway is more favourable in the singlet state with the lowest barriers. The most energy demanding step is also in this case, the proton transfer to form coordinated water (165 kJ/mol). The release of CO makes the reaction exothermic but releases less energy than with **1** (-20 kJ/mol).

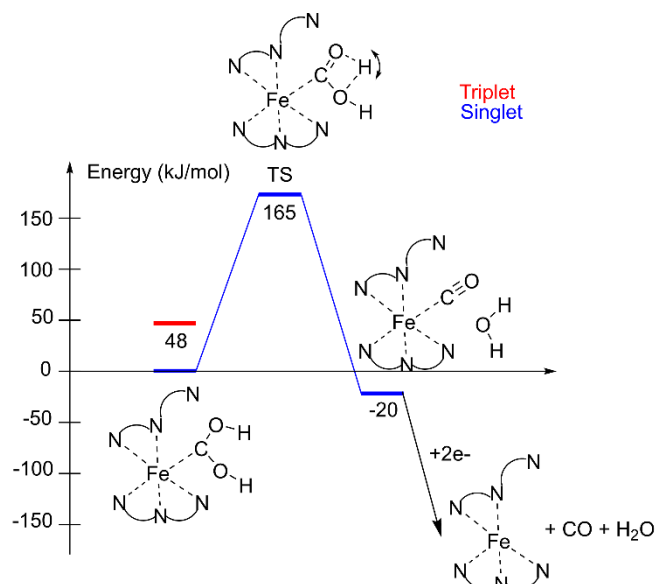


**Figure 4.2. 12** Energy diagram for CAT **3** for different multiplicities.

For complex **3** a second pathway has been investigated involving simultaneous proton and electron transfers.<sup>127, 132</sup> The charge of the complex remains unchanged during the whole cycle. The proposed mechanism and the energy profile for the photocatalytic reduction of CO<sub>2</sub> are depicted in Figure 4.2.13.

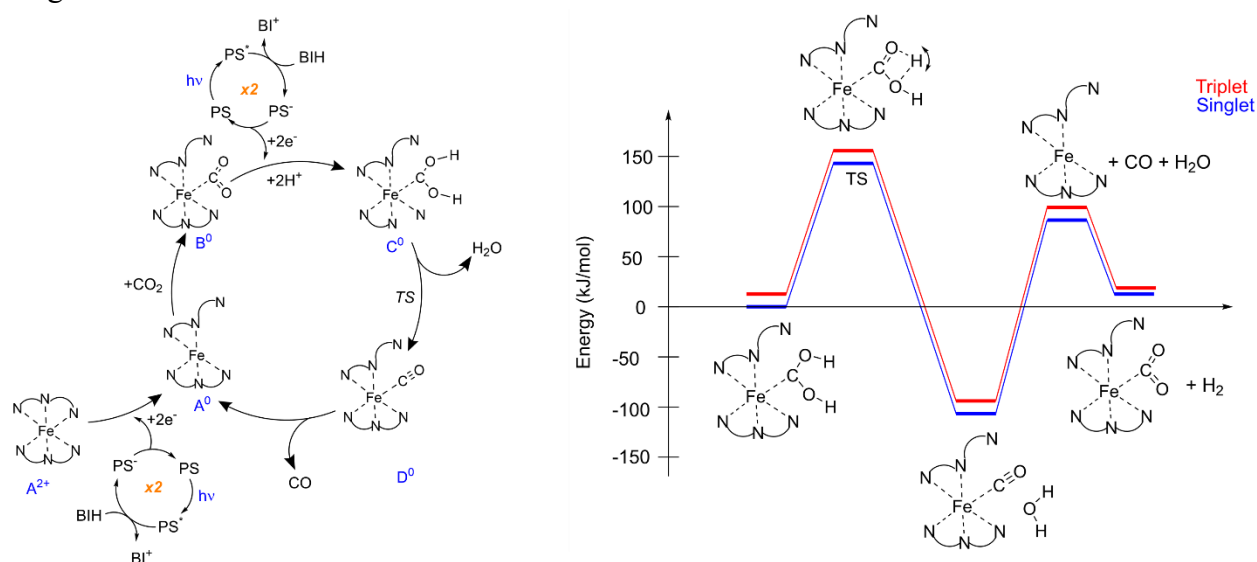


**Figure 4.2. 13** Proposed mechanism for the photocatalytic CO<sub>2</sub> reduction with complex **3**; hydrogenation and reduction in the same step (lhs) and energy diagram for complex **3** in different multiplicities (rhs), using r<sup>2</sup>SCAN-3c method.

## Application (II)

The energies of the transition states (TS) and of the intermediates in Schemes 4.2.1 and 4.2.2 for different spin states are shown in Figures 4.2.11 and 4.2.12 and their electronic and relative energies are shown in Table 4.2.8.

**Table 4.2. 8** Electronic energy (a.u.) and relative energy (kJ/mol) for different reaction paths in different multiplicities using r<sup>2</sup>SCAN-3c method.

Complex	Charge of complex	Species	Electronic energy (a.u.)		Relative energy (kJ/mol)	
			Triplet	Singlet	Triplet	Singlet
<b>1</b>	0	C <sup>0</sup>	-3244.380963	-3244.401698	54.43	0.00
		TS	-3244.310852	-3244.333154	238.53	179.95
		D <sup>0</sup>	-3244.388996	-3244.412573	33.35	-28.53
<b>3</b>	0	C <sup>0</sup>	-2543.764848	-2543.76969	12.72	0.00
		TS	-2543.705905	-2543.714017	167.49	146.19
		D <sup>0</sup>	-2543.806601	-2543.812244	-96.90	-111.71
	2+	C <sup>2+</sup>	-2543.322151	-2543.339358	45.19	0.00
		TS		-2543.271812		177.36
		D <sup>2+</sup>		-2543.346892		-19.79

The quintet states were omitted because of their approximately 40 kJ/mol higher energies than the singlet states for C and D. As it is shown in Table 4.2.8, the energy barrier for second pathway of complex **3** considering singlet state is lower than in first pathway by 31 kJ/mol.

### 4.2.4 Conclusion

The calculations back up the findings of the experiment that the newly synthesized iron heteroleptic complex, which is based on the N,N,N-pincer ligand 2,6-bis(4'-phenyl-1',2',3'-triazol-1-yl-methyl)pyridine, demonstrates high activity in the photo-driven reduction of carbon dioxide when combined with a heteroleptic copper complex that functions as a photosensitizer when exposed to visible light.

## Application (II)

---

We identified plausible mechanisms and the stability of possibly relevant intermediates, i.e., the CO-desorption energy, using DFT methods. We also identified the main transition states and determined reaction barriers. The activity of **1** is among the greatest that has been observed when using monometallic iron-based catalysts in a system that contains all earth-abundant components. In addition, the simultaneous synthesis of molecular hydrogen motivates additional research into the capability of this system to generate syngas from CO<sub>2</sub> in the presence of solar light.

### 4.3 Cooperativity-driven reactivity of a dinuclear copper dimethylglyoxime complex

#### 4.3.1 Introduction

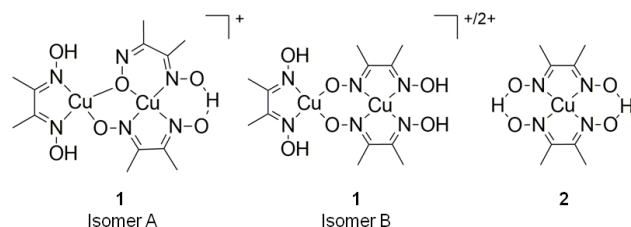
The term "cooperative effect" refers to the modification of a property of a system that is brought about by the interaction of the system's individual components. This effect can take place either intermolecularly or intramolecularly, and it can result in a variety of different types of cooperativity. Cooperativity of this kind is taken to significant use in the field of chemistry, for example in catalysis, the assembly of compounds on surfaces, and supramolecular polymerization, in order to produce and/or control the behavior that is desired.<sup>133-137</sup> Cooperativity can arise on the molecular level, for example in a complex, as a result of interactions between metal and ligand, ligand and ligand, or metal and metal. The coupling of metal centers in multinuclear complexes can influence the magnetic, catalytic, and optical characteristics, which leads to a clear contrast in comparison to their mononuclear analogues. This is because the latter factor is taken into consideration.<sup>136, 138-140</sup> According to the findings of the collaborative research center known as 3MET,<sup>141</sup> the nature of this cooperative behavior can either be useful, enthalpic, or entropic. Copper(II) dimethylglyoxime (H<sub>2</sub>dmg) complexes are a useful example to explore the cooperative effect because a variety of complexes that differ in their composition are known. This makes the complexes an ideal subject for this type of investigation.

These complexes include mono-,<sup>142-144</sup> di-,<sup>145, 146</sup> and tetranuclear<sup>147</sup> complexes, all of which have been characterized by crystal structure analysis,<sup>146</sup> infrared spectroscopy,<sup>148</sup> UV/Vis spectroscopy,<sup>149</sup> electron paramagnetic resonance [EPR],<sup>150</sup> and other magnetic methods.<sup>145</sup> Furthermore, copper dimethylglyoxime complexes have been utilized as catalysts in processes such as the N-arylation of imidazole derivatives<sup>151</sup> and the decomposition of hydrogen peroxide followed by the oxidation of benzyl alcohol and ethylbenzene (zeolite encapsulated).<sup>152</sup> Because the catalytically active complex was produced in situ in both instances by adding the copper(II) salt and H<sub>2</sub>dmg to the reaction mixture, the nature of the complex that was formed is a mystery.

Because we were interested in the reactivity of multinuclear copper complexes,<sup>153</sup> we decided to focus our attention on the dinuclear complex [Cu<sub>2</sub>(H<sub>2</sub>dmg)(Hdmg)(dmg)(EtOH)]ClO<sub>4</sub> (**1**) and its mononuclear analogue [Cu(Hdmg)<sub>2</sub>] (**2**) as a comparison (Scheme 4.3.1). There have been two different isomers described for **1**, however most of the research has focused on isomer A.<sup>145, 147</sup>

## Application (III)

The creation of the various isomers is dependent on the pH value, with the formation of isomer A being favored as the pH value increases.<sup>145</sup> In spite of the spectroscopic characterization, very little is known about **1**.



**Scheme 4.3. 1** Structures of **1** and its two isomers A (left) and B (middle) and structure of **2** (right). Cation and coordinating ethanol solvent molecule not shown for clarity. The charge of isomer B as well as the positions of the protons are not clarified, depending on the deprotonation state, the charge can be 1+ or 2+.

In this study, we report the cooperativity-driven and solvent-dependent degradation of copper-bound H<sub>2</sub>dmg to either NH<sub>4</sub><sup>+</sup> or N<sub>2</sub>O. Both of these products can be found in nature.

### 4.3.2 Computational Details

All calculations were performed with the program package Turbomole<sup>154</sup> using density functional theory (DFT). All calculations were performed with the B3LYP functional,<sup>120</sup> def2-TZVP basis set,<sup>86, 87</sup> and RI-approximation.<sup>155, 156</sup> UV/Vis spectra were calculated with time dependent DFT (TDDFT).<sup>157</sup> Transition states were preoptimized by a reaction path search from Plessow<sup>82</sup> and then determined by trust region image optimizations.<sup>83</sup> All calculations were carried out in the gas phase. Additionally, computations using the state average complete active space self-consistent field (CASSCF) were done.<sup>39</sup> With a program created in Karlsruhe and Kaiserslautern,<sup>47, 158</sup> spin orbit configuration interaction (SOC) calculations were carried out on the basis of the CASSCF orbitals using a spin orbit mean field technique for the 2-electron-spin-orbit integrals.<sup>159, 160</sup> The Abragam–Bleaney tensor, as described by Gerloch and McMeeking,<sup>161</sup> was used to generate the

g-tensors and magnetic susceptibilities were determined via Boltzman averaging using the derivatives of the energy with respect to the magnetic field.

### 4.3.3 Results and Discussion

$\text{Cu}(\text{ClO}_4)_2 \cdot 6\text{H}_2\text{O}$  and  $\text{H}_2\text{dmg}$  reacted in ethanol to produce **1**, which Becker et al. then crystallized using pentane diffusion. Similarly, **2** was produced when  $\text{Cu}(\text{OAc})_2 \cdot 2\text{H}_2\text{O}$  and  $\text{H}_2\text{dmg}$  reacted in methanol. A crystalline product resulted from the solvent's gradual evaporation. Both compounds' molecular structures, which can be seen in Figure 4.3.1, have been determined and are similar to those previously reported in the literature.<sup>144, 145</sup>

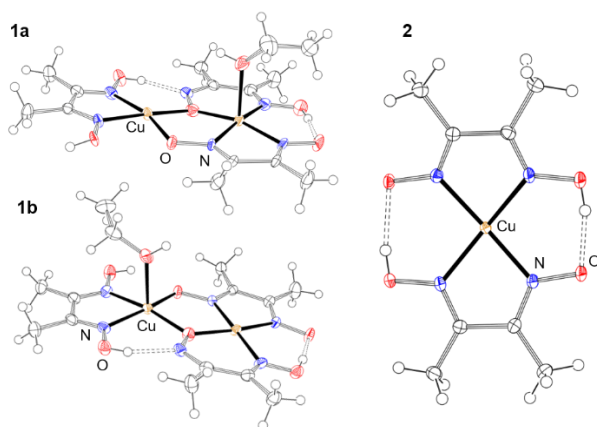


**Figure 4.3. 1** Molecular structures of **1a**, **1b**, and **2**. **1a**:  $d(\text{Cu}-\text{Cu})$ : 3.293(8) Å, **1b**: 3.32(1) Å. Ellipsoids are set at the 50 % probability level. The counter ions of **1a** and **1b** are omitted for clarity.

We also performed structural optimization at the B3LYP/def2-TZVP level; the results are shown in figure 4.3.2. As can be seen, the distances between the two copper centers in **1a** and **1b** are 3.300 and 3.319 respectively, demonstrating strong geometric agreement with the experimental results. The copper charge in both structures is 2+, producing cationic structures.

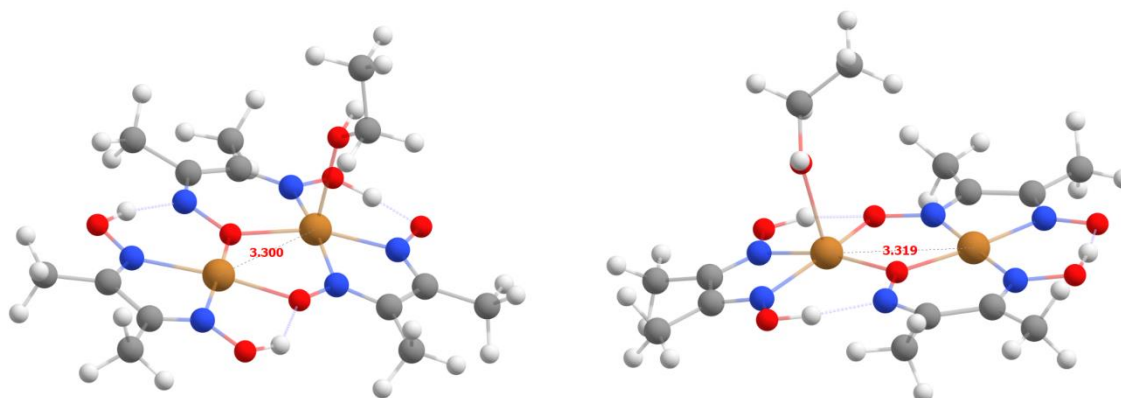


**Figure 4.3. 2** Molecular structures of 1a(left), 1b(right) in case of Cu(II)Cu(II) and singlet state. 1a: d(Cu-Cu): 3.300 Å, 1b: 3.319 Å. Functional: B3LYP, Basis set: def2-TZVP.

**Table 4.3. 1** Electronic energy (a.u.) of different optimized structures for different multiplicities and functionals. Basis set: def2-TZVP.

Structure	Multiplicity	Energy (a.u.)			
		<b>B3LYP</b>	<b>PBE0</b>	<b>M06</b>	<b>PBE</b>
A	<b>Singlet</b>	-4530.1491	-4529.0719	-4530.0787	-4529.1089
	<b>Triplet</b>	-4530.1435	-4529.0670	-4529.0670	-4529.0897
B	<b>Singlet</b>	-4530.1471	-4529.0684	-4530.0791	-4529.1017
	<b>Triplet</b>	-4530.1438	-4529.0658	-4530.0751	-4529.0880
1a	<b>Singlet</b>	-4685.1759			
	<b>Triplet</b>	-4685.1706			
1b	<b>Singlet</b>	-4685.1776			
	<b>Triplet</b>	-4685.1726			

According to table 4.3.1, which compares the electronic energies of isomer A and B, as well as **1a** and **1b**, for Cu(II)Cu(II) in a variety of functionals and multiplicities, the singlet state is approximately 10–14 kJ/mol more stable than triplet.

One ethanol solvent molecule, as seen in figure 4.3.1, coordinates one of the copper centers, resulting in the two distinct isomers **1a** and **1b**, which have the [N<sub>3</sub>O<sub>2</sub>]/[N<sub>2</sub>O<sub>2</sub>] and [N<sub>3</sub>O]/[N<sub>2</sub>O<sub>3</sub>] motifs, respectively. The ratio of each isomer in the crystal structure is the same. Only isomer A could be achieved despite numerous attempts to prepare isomer B solely (Scheme 4.3.1). The results are compiled in Table 4.3.2 and are consistent with DFT calculations, which demonstrate that isomer A is the lower energy isomer.

Additional DFT calculations show an antiferromagnetic exchange coupling of two S=1/2 states for the two isomers of **1**, which results in a singlet (broken symmetry state) and a triplet state. In Figure 4.3.3, the spin densities of the two isomers are displayed.

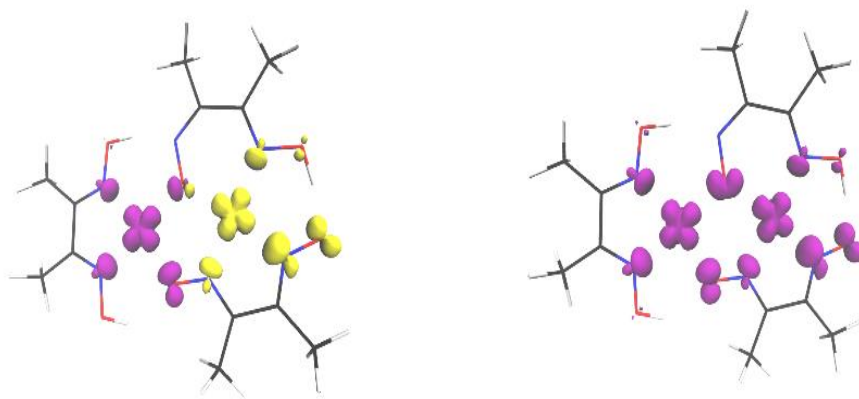


**Figure 4.3. 2** Spin density for singlet states (left) and triplet states (right) of isomer A of **1**. Isovalue:  $\pm 0.01$ ,  $S^2$  for singlet is 0.86 (indicating broken-spin solution), for triplet is 2.

## Application (III)

According to the findings presented in Table 4.3.2, the energy of the singlet state of isomer A is 5.24 kJ/mol lower than the energy level of the singlet state of isomer B.

**Table 4.3. 2** Electronic energy (a. u.) and relative energy (kJ/mol) for isomer A and B of **1** in different multiplicities using B3LYP/def2-TZVP.

Isomer	Electronic energy (a. u.)		Relative energy (kJ/mol)	
	Singlet	Triplet	Singlet	Triplet
<b>A</b>	-4530.149107	-4530.143495	0.00	14.73
<b>B</b>	-4530.147111	-4530.143776	5.24	9.055

Isomer A, which has a shorter Cu-Cu distance than isomer B (Figure 4.3.4), has a stronger exchange coupling than isomer B, which results in a 10 kJ/mol energy difference between the singlet and triplet states of isomer A in comparison to isomer B. This shorter Cu-Cu distance is due to the fact that isomer A has a shorter Cu-Cu distance than isomer B.

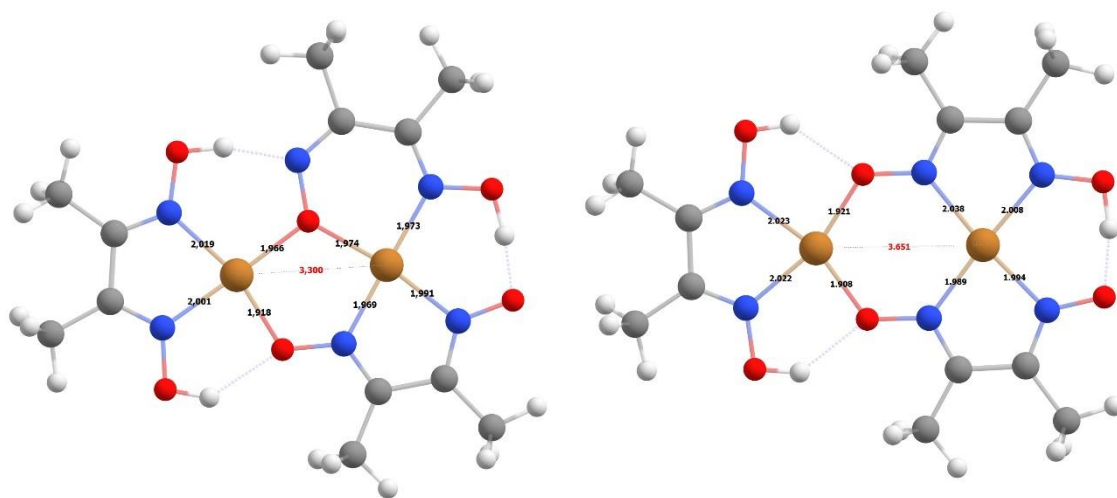


**Figure 4.3. 3** Molecular structures of isomer A (left) and B(right) of **1** after optimization. Bond lengths are in Å. Basis set: def2-TZVP; functional: B3LYP.

The equimolar mixture of **1a** and **1b**, known as **1**, has been used in all subsequent investigations because it is not possible to experimentally separate **1a** and **1b**. Together with Becker et al., we used UV/Vis, IR, MS, EPR, and DFT techniques to describe **1** and **2**. According to their research, the experimental UV/Vis spectrum of **1** (Figure 4.3.5) shows two strong transitions into LC (ligand-centered) states at 229 nm and 271 nm, where transitions into MLCT (metal-to-ligand charge transfer) states primarily contribute to the band at 271 nm.

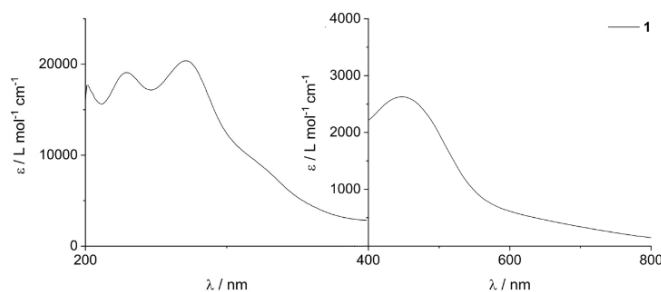


**Figure 4.3. 4** UV/Vis spectra of **1** in methanol (left:  $c = 3.56 \cdot 10^{-5}$  mol/L, right:  $c = 1.94 \cdot 10^{-4}$  mol/L).

The time-dependent (TD) DFT predicted UV/Vis-spectrum anticipated two transitions into LC states at 230 nm and 270 nm, which are composed of numerous transitions of equivalent intensity. The experimental results are in great agreement with the projected TD-DFT UV/Vis-spectrum, as shown in Figure 4.3.6, which directly compares the simulated and observed spectra. The peak at 270nm consists of transitions into LC and MLCT states. At 345 nm, 490 nm, and 650 nm, maxima of lesser intensity that were caused by transitions into MLCT states were expected, these transition densities are shown in Figure 4.3.7.

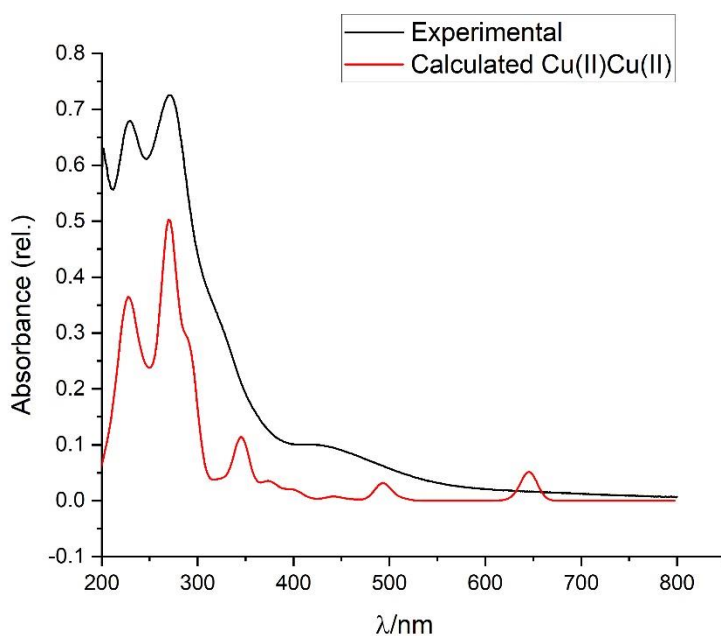


**Figure 4.3. 5** Comparison between Calculated UV/Vis spectrum (Cu(II)/Cu(II)) and the experimental spectrum of **1**.

The peak at 270nm consists of transitions into LC and MLCT states. At 345 nm, 490 nm, and 650 nm, maxima of lesser intensity that were caused by transitions into MLCT states were expected, these transition densities are shown in Figure 4.3.7.

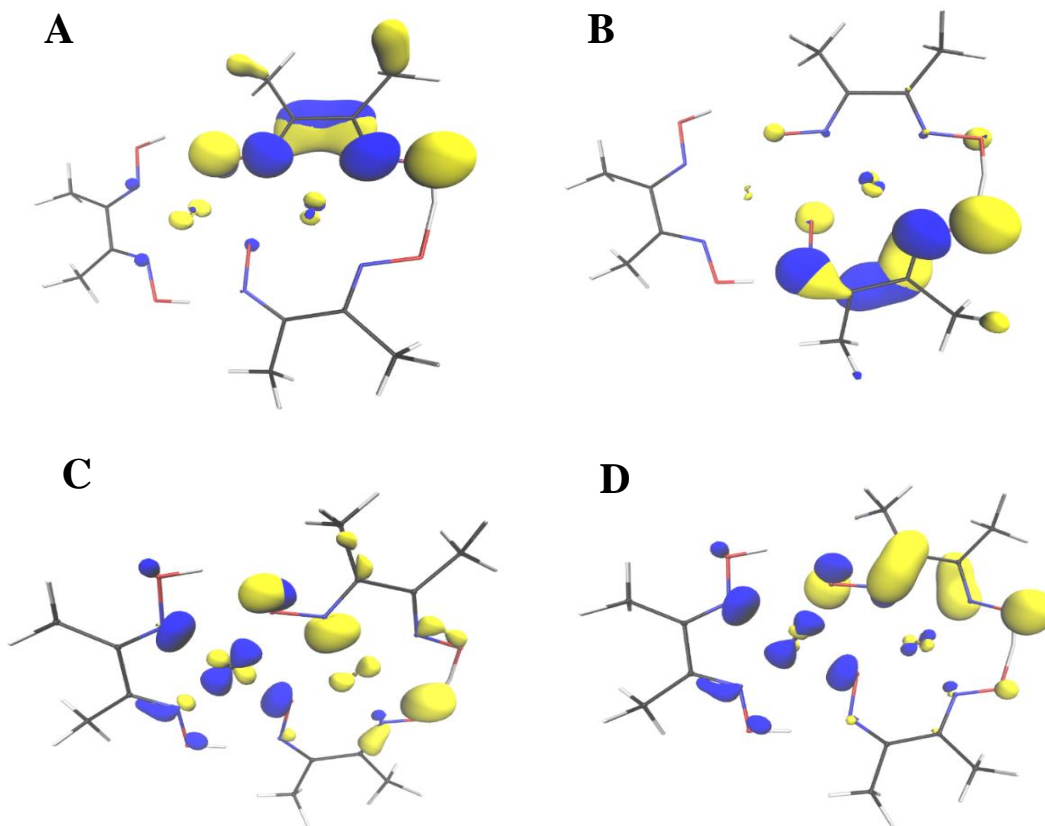


**Figure 4.3. 6** Calculated transition densities at 230 nm (A), 270 nm (B), 345 nm (C), and 490 nm (D) for **1** (Cu(II)/Cu(II)). Basis set: def2-TZVP; functional: B3LYP, isovalue:  $\pm 0.05$

To get information about the electronic states and the magnetic anisotropy, complete-active-space self-consistent field (CASSCF) and spin-orbit configuration interaction (SOC) calculations were performed for **1** and **2**, using the program developed by Meier and Staemmler<sup>39</sup> and utilizing code that was optimized for magnetic systems by T. Bodenstern.<sup>47</sup> When doing CASSCF calculations, the active space CAS(18, 10) was taken into consideration. This corresponds to 18 valence electrons located in 10 d orbitals of two copper centers. The outcomes of the CASSCF and SOC calculations are presented in Table 4.3.3. The lowest triplet state has an energy that is 62  $\text{cm}^{-1}$  higher than the ground singlet.

## Application (III)

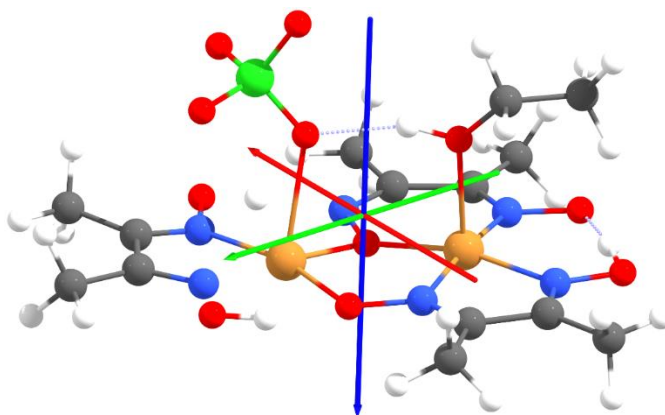
**Table 4.3. 3** Energies (in  $\text{cm}^{-1}$ ) of the lowest electronic states for **1** with inclusion of Spin–Orbit Coupling, CAS (18,10) SCF/CI.

CASSCF (18, 10)			SOC	
Spin= 1	States		States	
<b>1</b>	$^1A_1$	0	$^1A_1$	0
<b>2</b>	$^3A_1$	62	$^3A_1$	62.429
<b>3</b>	$^3A_1$	11273	$^3A_1$	62.435
<b>4</b>	$^1A_1$	11274	$^3A_1$	62.615

Additionally, the g tensor values are listed in Table 4.3.4. The g tensors were estimated for triplet states by using the lowest three energies from SOCI calculations with pseudospin  $S = 1.0$ , for which g is rather anisotropic.

**Table 4.3. 4** g-tensors of the lowest states(triplet) for **1** with two ligands, spin  $S=1.0$ . In the figure directions show g-tensors, g1 (red), g2 (green) g3 (blue).

S=1.0	g1	g2	g3
	2.08	2.09	2.47
Magnetic main axes			
X	-0.83	-0.53	-0.13
Y	0.42	-0.48	-0.76
Z	-0.34	0.69	-0.63



Magnetic susceptibility was also done for **1**, and the results are presented in Figure 4.3.8. This computed magnetic susceptibility of triplet and singlet states reveals gradually increases to 0.85  $\text{cm}^3\text{K/mol}$  as the temperature is raised.

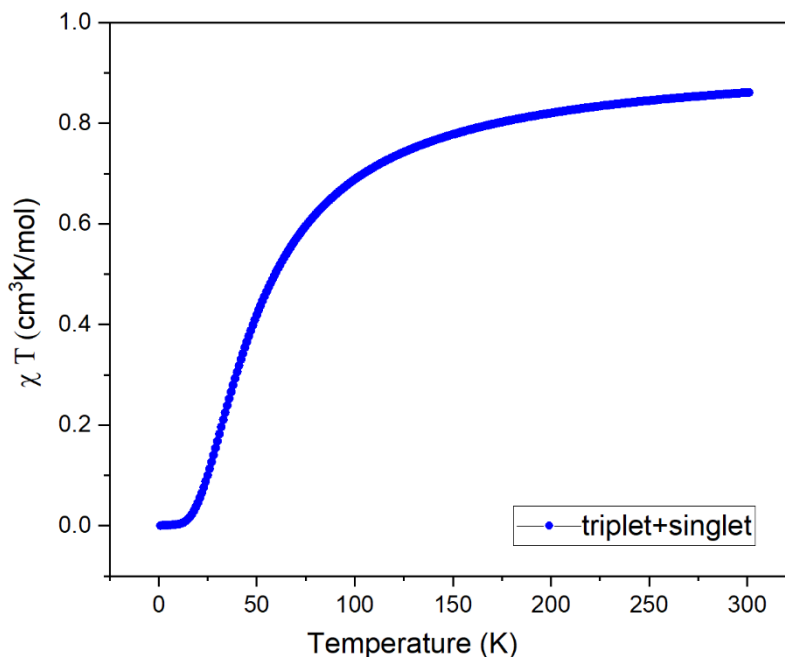


**Figure 4.3. 7** Magnetic Susceptibility of triplet and singlet states of **1** with Magnetic field  $B = 1.0$

Calculations using the active space CAS(9, 5) in CASSCF were used for **2** with and without ethanol. This is equivalent to the copper center having 9 valence electrons distributed in 5 d orbitals. Table 4.3.5 displays the results of the CASSCF and SOCI computations. The zero-field splitting of the Kramer's doublets is approximately  $13000 \text{ cm}^{-1}$ , while the next excited state has an energy that is  $13,000 \text{ cm}^{-1}$  greater than the ground state, demonstrating that spin orbit coupling is not a significant factor.

## Application (III)

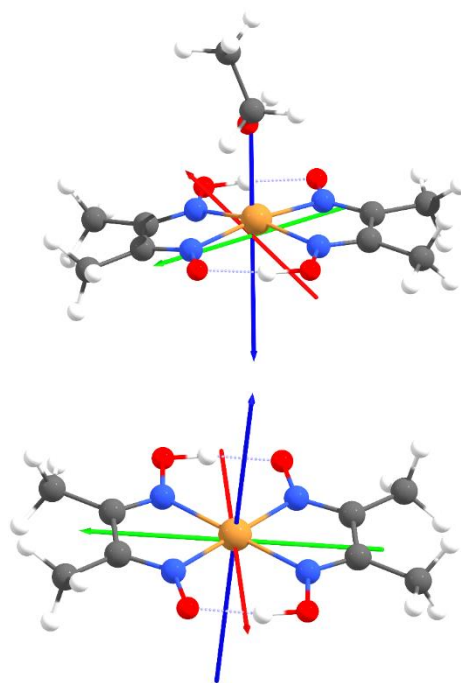
**Table 4.3. 5** Energies (in  $\text{cm}^{-1}$ ) of the lowest electronic states of **2** with and without ethanol and inclusion of Spin–Orbit Coupling, CAS (9,5) SCF/CI.

	CASSCF (9,5)			SOC1		
	<b>2</b>	<b>2 with ethanol</b>	KD	<b>2</b>	<b>2 with ethanol</b>	
<b>Spin= 1/2</b>						
<b>1</b>	0	0	K1	0	0	
<b>2</b>	13337	12265	K2	13233	11953	
<b>3</b>	14994	12810	K3	14484	12411	
<b>4</b>	15314	13416	K4	15106	13662	
<b>5</b>	15332	13715	K5	16511	14560	

Additionally, the g tensor values are listed in Table 4.3.6. The g tensors were estimated for lowest Kramer’s doublet from SOCI calculations with pseudospin  $S = 1/2$ , for which g is rather anisotropic.

**Table 4.3. 6** g-tensors of the lowest Kramer’s doublet for **2** with and without ethanol, spin  $S=1/2$ . In the figure directions show g-tensors, g1 (red), g2 (green) g3 (blue) for **2** without ethanol (down) and **2** with ethanol (up).

<b>S=1/2</b>	<b>2</b>			<b>2with Ethanol</b>		
	<b>g1</b>	<b>g2</b>	<b>g3</b>	<b>g1</b>	<b>g2</b>	<b>g3</b>
	2.09	2.09	2.43	2.10	2.09	2.45
	<b>Magnetic main axes</b>					
<b>X</b>	0.04	0.99	-0.01	-0.65	-0.76	0.06
<b>Y</b>	-0.88	0.03	-0.47	-0.62	0.57	0.53
<b>Z</b>	0.47	-0.03	-0.88	0.43	-0.31	0.84



For **1b** and isomer A, calculations were performed in CASSCF utilizing the active space CAS(18, 10). This is the same as two copper centers both having 10 d orbitals with 18 valence electrons. The outcomes of the CASSCF and SOCI computations are shown in Table 4.3.7. As one can see, the energy of the following excited state is 68 cm<sup>-1</sup> higher than the ground state and the energy difference between the ground state and the next excited states is considerably larger. The following state, which is located at 68 cm<sup>-1</sup>, is well separated from the ground state in both complexes according to SOCI calculations.

**Table 4.3. 7** Energies (in cm<sup>-1</sup>) of the lowest electronic states for **1b** and isomer A with inclusion of Spin–Orbit Coupling, CAS (18,10) SCF/CI.

CASSCF (18, 10)					SOC1		
Spin= 1	States	Isomer A	States	1b	States	Isomer A	1b
1	<sup>1</sup> A <sub>1</sub>	0	<sup>1</sup> A <sub>1</sub>	0	<sup>1</sup> A <sub>1</sub>	0	0
2	<sup>3</sup> A <sub>1</sub>	68	<sup>3</sup> A <sub>1</sub>	14	<sup>3</sup> A <sub>1</sub>	68.534	13.659
3	<sup>1</sup> A <sub>1</sub>	10424	<sup>3</sup> A <sub>1</sub>	5870	<sup>3</sup> A <sub>1</sub>	68.538	13.665
4	<sup>3</sup> A <sub>1</sub>	10441	<sup>1</sup> A <sub>1</sub>	5870	<sup>3</sup> A <sub>1</sub>	68.664	13.764

In the instance of **1b** or isomer A, splitting diagrams for the d levels in a square planar and square pyramidal ligand field are displayed in Figure 4.3.9. The energy difference in Table 4.3.7 demonstrates that dz<sup>2</sup> experiences repulsion from the additional ligand when the ligand field is changed, and a new ligand is added. As a result, the energy is pushed upward, and the energy gap between dx<sup>2</sup>-y<sup>2</sup> and dz<sup>2</sup> becomes significantly less.

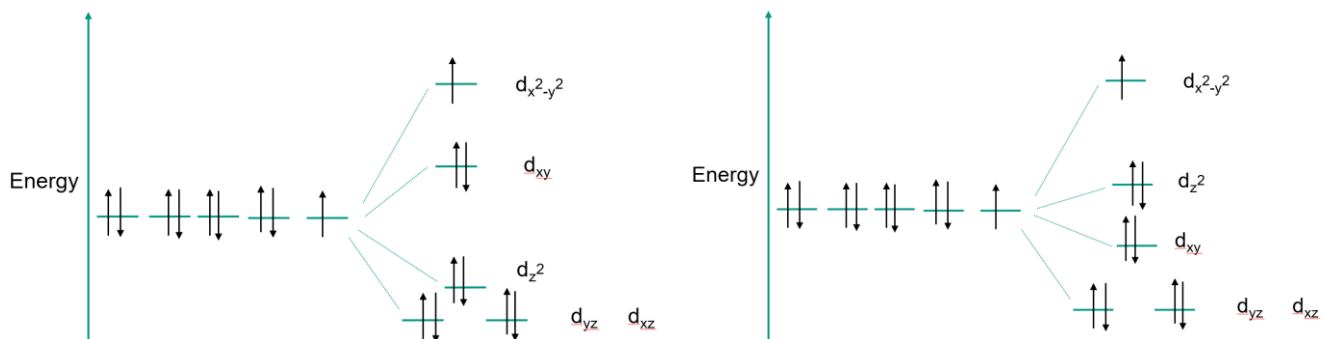


**Figure 4.3. 8** Splitting diagrams of the d levels in a square planar (left) and square pyramidal (right) ligand field.

The values of the g tensor are additionally provided in Table 4.3.8. The g tensors were calculated using SOCI computations with pseudospin  $S = 1$  for the lowest states of the triplet, where g is relatively anisotropic.

**Table 4.3. 8** g-tensors of the lowest states (triplet) for isomer A and **1b**, spin  $S=1.0$

Method	Isomer A /SOCI	1b /SOCI
<b>g1</b>	2.08	2.04
<b>g2</b>	2.09	2.21
<b>g3</b>	2.51	2.67

The results of the magnetic susceptibility tests of isomer A and **1b** for singlet and triplet states are shown in Figure 4.3.10. When we first begin antiferromagnetically coupling, the susceptibility is almost zero. As we continue to occupy excited triplets more and more, our susceptibility increases. When we begin to get an average over all three components of the triplet, it then continues to drop.

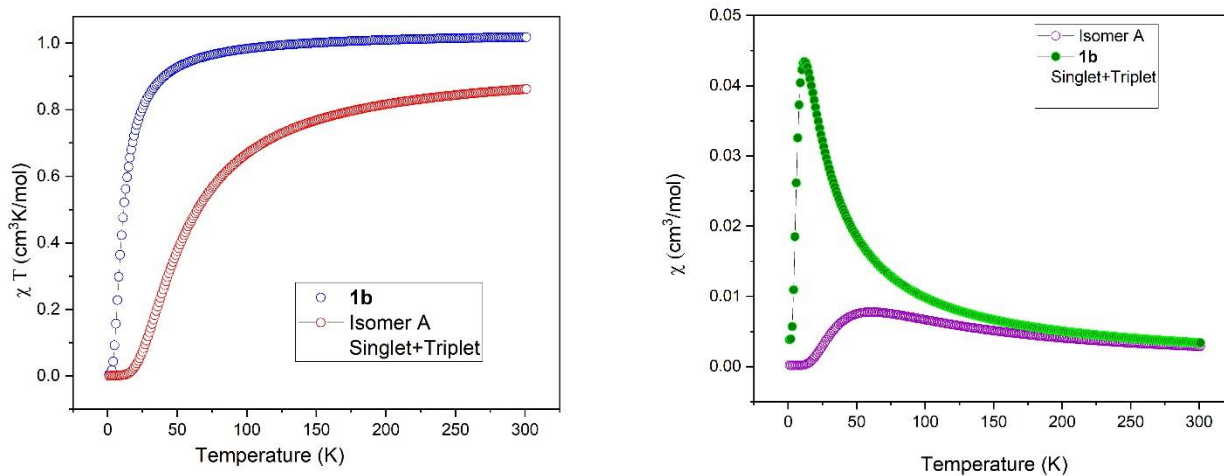
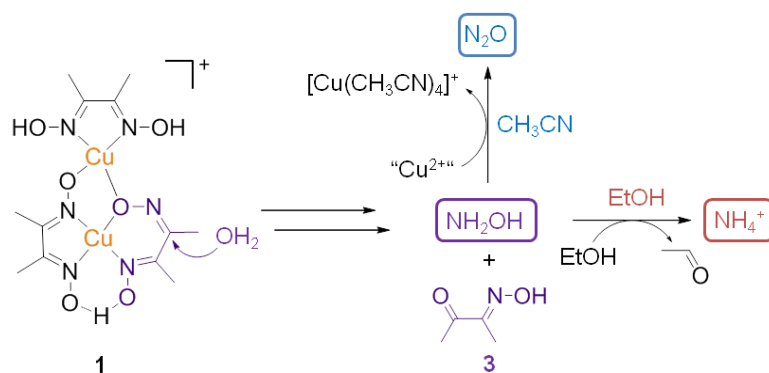


**Figure 4.3. 9** Magnetic Susceptibility of triplet and singlet states with Magnetic field  $B = 1.0$ , left:  $\chi T$  (cm<sup>3</sup>K/mol), right:  $\chi$  (cm<sup>3</sup>/mol)

Using ethanol as the solvent caused substantial amounts of  $\text{NH}_4\text{ClO}_4$  to crystallize, while using acetonitrile as the solvent caused significant amounts of  $[\text{Cu}(\text{MeCN})_4]\text{ClO}_4$  to crystallize, according to studies conducted by Becker and colleagues.

Because of these data, we hypothesize the same first reaction step: the nucleophilic attack of  $\text{H}_2\text{O}$  at the glyoxime carbon atom results in the hydrolysis of the  $\text{Hdmg}^-/\text{dmg}^{2-}$  ligand, which produces 2,3-butanedione monoxime (**3**) and intermediate  $\text{NH}_2\text{OH}$ .  $\text{NH}_2\text{OH}$  was either reduced to  $\text{NH}_4^+$  or oxidized to  $\text{N}_2\text{O}$ , giving  $\text{Cu}^+$  as a reduced species, depending on the reaction conditions (yielding acetaldehyde as oxidized species, Scheme 4.3.2).



**Scheme 4.3. 2** Postulated nucleophilic attack of  $\text{H}_2\text{O}$  at the glyoxime carbon atom to form intermediate  $\text{NH}_2\text{OH}$  and 2,3-butanedione monoxime (**3**). Subsequently and depending on the solvent,  $\text{NH}_2\text{OH}$  will either be oxidized to  $\text{N}_2\text{O}$  or be reduced to  $\text{NH}_4^+$ .

Several spectroscopic and theoretical methods were employed to support this hypothesis. We were able to provide reasonable insight into the reactivity of **1**; however, because of the complexity of the system and the high volatility of diverse reaction products, only a generalized mechanism could be proposed. As a first step, we propose the nucleophilic attack of  $\text{H}_2\text{O}$  at the glyoxime carbon atom of the bridging  $\mu_2\text{-O-N=C}$ -group. This  $\text{Hdmg}^-/\text{dmg}^{2-}$  molecule is the only one, whose oxygen atom coordinates both copper centers in a bridged fashion. Due to the coordination of two Lewis acidic centers, it is reasonable to assume that the electron density distribution in comparison to the other  $\text{O-N=C}$  motifs differs and thus, the electrophilicity at the carbon atom of this glyoxime group is higher than that of the other carbon atoms, which facilitates the nucleophilic attack of  $\text{H}_2\text{O}$ . As shown by DFT calculations and depicted in Figure 4.3.11, indeed, this carbon atom has a much higher Mulliken charge in comparison to any other carbon atom of the  $\text{O-N=C}$  motifs and thus, a nucleophilic attack at this carbon atom is favored. Notably, the Mulliken charge for C6 in isomer A of **1** is significantly higher than for the carbon atoms in **2** (see Figure 4.3.12).

Atoms	Mulliken charges
C1	-0.37779
C2	-0.36744
C3	0.12118
C4	0.10261
C5	-0.41054
C6	0.21212
C7	-0.38240
C8	0.18775
C9	0.10364
C10	0.06000
C11	-0.33945
C12	-0.41424

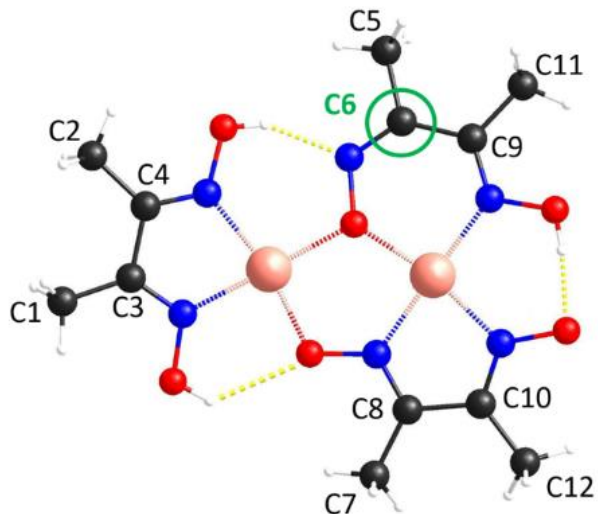


**Figure 4.3. 10** Mulliken charges of isomer A of **1** using B3LYP/def2-TZVP.

Atoms	Mulliken charges
C1	-0.35800
C2	-0.38370
C3	0.15971
C4	0.06139
C5	-0.36958
C6	0.06115
C7	0.16113
C8	-0.38892

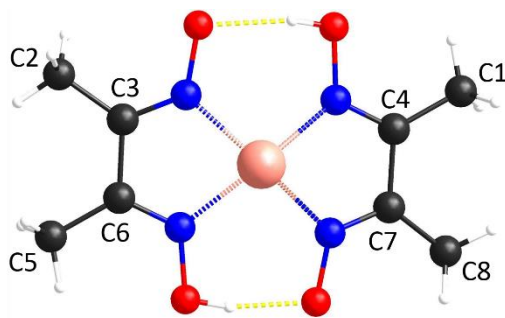


**Figure 4.3. 11** Mulliken charges of **2** using B3LYP/def2-TZVP.

A nucleophilic attack by water was thus discouraged in **1** due to the existence of this unique Cu-O-Cu coordination motif, which is mirrored by the stability of **2** against moisture and water. As a result, it is possible to explain the preferred hydrolysis of the  $\text{Hdmg}^-/\text{dmg}^{2-}$  molecule in terms of

the cooperation of the two Cu(II) ions in facilitating the nucleophilic attack of H<sub>2</sub>O. The reaction solutions contained NH<sub>2</sub>OH and **3**, which were produced by this hydrolysis (vide infra).

To prove this initial step, we carried out DFT calculations that focused on the formation of NH<sub>2</sub>OH. The mechanism proposed generally represents an oxime hydrolysis (Figure 4.3.13). We observed that the energy barrier of the reaction is strongly dependent on the number of water molecules involved in the process, i.e. when just one water molecule is involved, the barrier is much higher. This is consistent with results of *Rzepa* obtained by using a model system.<sup>162</sup> The first stage is a nucleophilic attack of H<sub>2</sub>O on the most electrophilic carbon, which is in the  $\mu_2$ -O-N=C-group (Figure 4.3.11, C6). Simultaneously, proton reorganization mediated by a second H<sub>2</sub>O molecule takes place at a neighboring oxime group (see TS1 in Figure 4.3.13).

It is important to note that this proton transfer takes part not from the water molecule, but from the N-OH group of the coordinating oxime (that is reprotonated from the water chain by Grotthuss mechanism).<sup>163</sup> This results in Intermediate 1 that easily turns into a zwitter-ionic tautomer (Intermediate 2). The latter tautomerizes with N-C bond splitting into the product, which is a coordinated 2,3-butanedione monoxime (**3**). Thus, the role of the second H<sub>2</sub>O molecule (not spent in the hydrolysis process) is the proton transfer during the reaction. Here, one can expect that this can be significantly influenced by solvent and its pH value. The first barrier (159 kJ/mol) is noticeably higher than the second one (117 kJ/mol) and thus is rate-controlling.

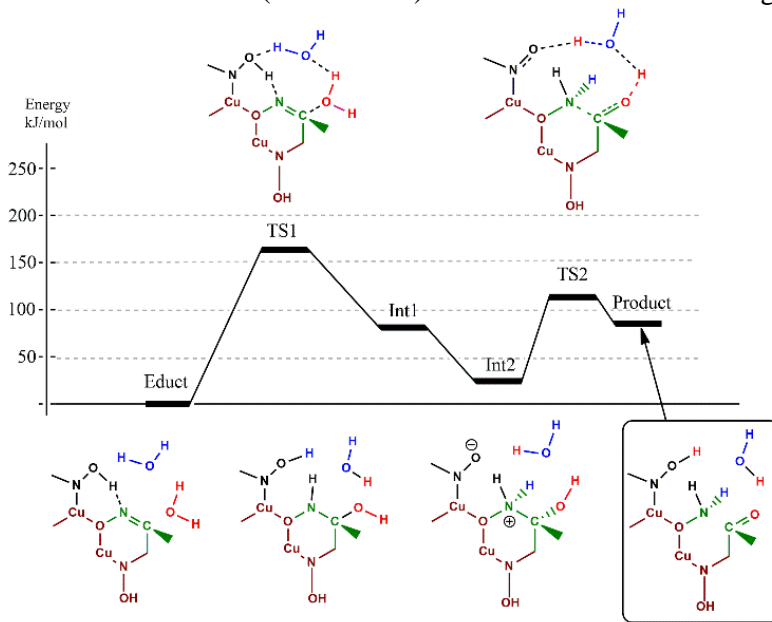


**Figure 4.3. 12** Proposed mechanism and energy diagram for isomer A of **1** using B3LYP/def2-TZVP.

Maxima at 262 nm, which are depicted in Figure 4.3.14, may signify coordinated 2,3-butanedione monoxime, supporting the proposed mechanism based on TDDFT calculations.

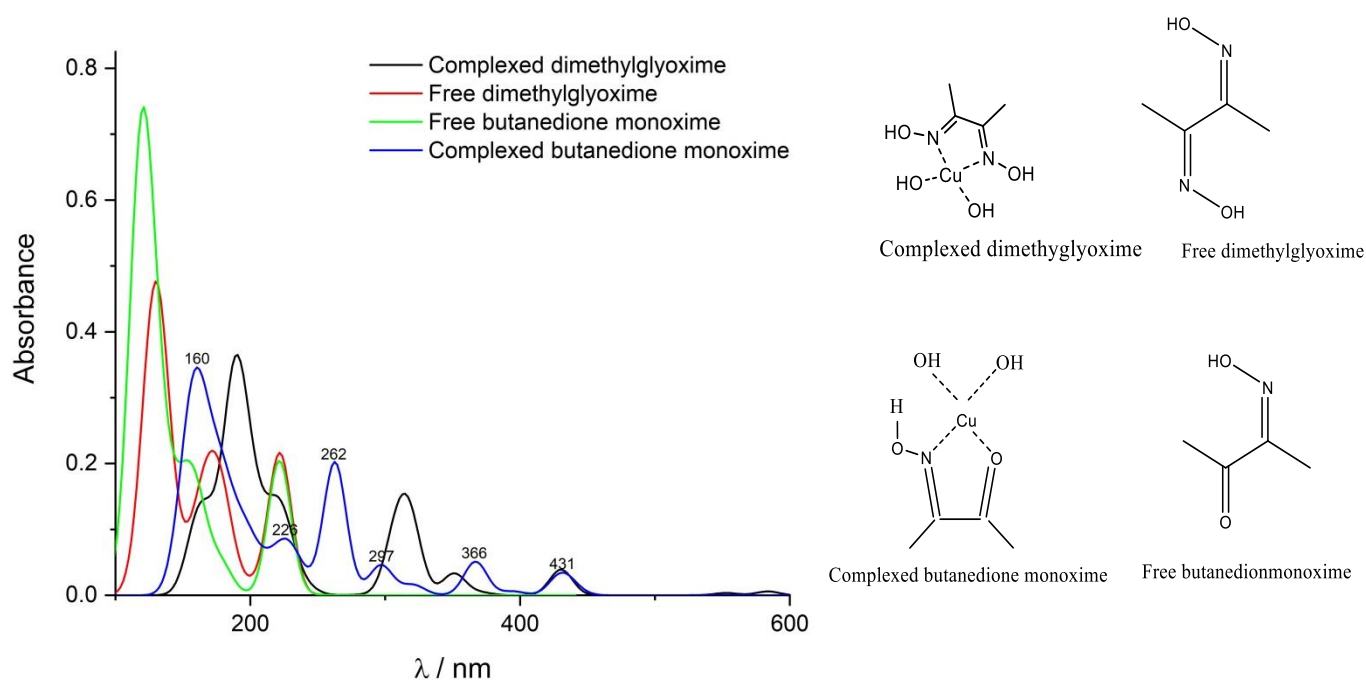


**Figure 4.3. 13** Calculated UV/Vis spectra for H<sub>2</sub>dmg and 2,3-butanedione monoxime.

#### 4.3.4 Conclusion

DFT calculations were performed on the dinuclear copper(II) complex [Cu<sub>2</sub>(H<sub>2</sub>dmg)(Hdmg)(dmg)]ClO<sub>4</sub> (**1**) and its mononuclear analogue [Cu(Hdmg)<sub>2</sub>] (**2**) which have been produced and comprehensively described in the group of Sabine Becker (TUK). In the calculations, the electronic structures of the complexes were determined, and their spectra simulated and compared to experiment. Furthermore, the experimental data indicates hydrolysis that leads to the formation of NH<sub>2</sub>OH and 2,3-butanedione monoxime (**3**). In this thesis, a feasible reaction mechanism based on DFT simulations is proposed, which is essentially the hydrolysis of

the glyoxime to produce **3** and  $\text{NH}_2\text{OH}$ . Notably, two  $\text{H}_2\text{O}$  molecules take part, one of which attacks the carbon atom nucleophilically and the other of which is involved in proton transfer.

According to DFT calculations, the carbon atom at which nucleophilic attack takes place has a much higher Mulliken charge in comparison to any other carbon atom in complex **1**. This  $\text{Hdmg}^-/\text{H}_2\text{dmg}$  ligand is therefore more favorable to the nucleophilic attack of  $\text{H}_2\text{O}$ , which results in the hydrolysis products 2,3-butanedione monoxime (**3**) and  $\text{NH}_2\text{OH}$ . As a result, the cooperativity of the two  $\text{Cu(II)}$  ions working together to boost the electrophilicity of the glyoxime carbon atom of the bridging  $\mu_2\text{-O-N=C}$ -group enables the formation of  $\text{NH}_2\text{OH}$ , which reacts to  $\text{N}_2\text{O}$  in  $\text{CH}_3\text{CN}$  and  $\text{NH}_4^+$  in ethanol.

### 5 SUMMARY

This thesis extensively examined three challenging topics that are the characterization of transition metal complexes and their reactions. The chosen systems are related to redox catalysis, photocatalysis and electrochemical catalysis, respectively.

The first project concentrated on Ni-based transition metal complexes with a ferrocene-based ligand. I have looked into the variations in the ionization potential of Ni(II) and Fe(II), and analyzed where in the molecule the ionization takes place, in order to support the electrochemical results of experiments on the one hand, and to find an explanation for the inactivity of the bimetallic complexes in catalytic cross-coupling on the other. The results were compared to those obtained from calculations on model systems in which Fe was substituted by an all-electron pseudopotential, restricting ionization to Ni. Based on spin density and ionization potential, the ionization occurs mainly at Ni(II). The results of various functionals were compared. For hybrid functionals, the spin density is entirely localized on Ni while there is a considerable contribution on Fe for GGA (general gradient approximation) functionals. The quasi particle energies derived by GW calculations, which enable differentiation between the lowest ionization from a Ni- and a Fe-dominated orbital, support these findings. In the reactivity investigations, Ni(II)/Fe(II), Ni(II)/Fe(III), Ni(III)/Fe(II), and Ni(III)/Fe(II) with an extra Br<sup>-</sup> coordinating the Ni site were considered. Only a Ni(III) center seems to be suitable for the reductive elimination. Additionally, the extra coordination of a Br<sup>-</sup> anion, which is freely accessible in solution, towards the nickel unit greatly increases the activation energies for both oxidative addition and reductive elimination. This self-poisoning of the active catalytic site offers a potential justification for why only stoichiometric turnover was detected experimentally and not catalytic turnover.

The second project looked on photocatalytic systems for reducing carbon dioxide. The 2,6-bis(1',2',3'-triazolyl-methyl)pyridine-based homogeneous Fe(II) catalyst has been investigated and compared to analogs which is homoleptic Fe complex. It is well known that CO<sub>2</sub> can only be adsorbed on reduced complexes when it comes to CO<sub>2</sub> reduction. Firstly, the energetics of charge changes of both complexes were studied, it was found that even when coordination on the metal center is geometrically allowed, CO<sub>2</sub> is only stable with two times reduced complexes. The electronic structure of these complexes was first investigated. Unpaired electrons are primarily

localized on the iron centers and to a lesser extent on the adsorbed CO<sub>2</sub> as well as the ligand system. Additionally, all of the complexes can only adsorb CO<sub>2</sub> after the release of a coordinating ligand that helps to keep the octahedral shape. Following that, the CO<sub>2</sub> adsorption on the iron center was examined while taking into account various patterns of CO<sub>2</sub> adsorption. Principle transition states, estimated reaction barriers, various possible mechanisms, and stability of potentially relevant intermediates, i.e., CO-dissociation energy, have all been found using DFT approaches.

In the third project, the cooperative effects of dinuclear copper(II) dimethylglyoxime (H<sub>2</sub>dmg) and its mononuclear analogue [Cu(Hdmg)<sub>2</sub>] complexes are investigated. DFT and CASSCF calculations on the electronic structure were performed. The two Cu(II) centers in the binuclear complex are antiferromagnetically coupled to a singlet state. The magnetic susceptibility was simulated and the g-tensors of the individual Cu centers as well as for the excited triplet state were obtained. Analyzing Mulliken charges, it could be confirmed that the electrophilicity of the carbon atom in the bridging  $\mu_2$ -O-N=C-group of H<sub>2</sub>dmg is increased due to the combined Lewis acidity of the two copper centers, which enhances the nucleophilic attack of H<sub>2</sub>O. Based on DFT calculations a reaction mechanism was proposed which essentially involves an oxime hydrolysis. The energy barrier of the reaction is highly influenced by the quantity of water molecules participating; the barrier is much higher when only one water molecule is involved. The result of this hydrolysis is 2,3-butanedione monoxime and NH<sub>2</sub>OH, which can subsequently be either oxidized or reduced depending on the solvent.

### 6 ACKNOWLEDGEMENTS

It gave me great pleasure to work at KIT for these three wonderful years. Prior to anything else, I want to express my gratitude to my supervisor, Prof. Dr. Karin Fink, for all of her help, inspiration, and patience.

Without Prof. Dr. Willem Klopper, who allowed me to work in his group, I would almost certainly not be able to complete this PhD thesis. He always went above and above to assist and promoted a vibrant scientific environment.

I would like to extend my sincere gratitude to my former and current colleagues, in particular Dr. Juana Vázquez Quesada, Dr. Michael Harding, Patrick Bügel, Chengyu Jin, and Siddhi Dinkar Gojare, whose corrections and comments significantly improved this work. A special thank you goes to my officemate, Christian Franz Pachtl, with whom I enjoyed many highly motivating conversations in the final months of my PhD.

I want to thank Dr. Dmitry Sharapa for the scientific discussion that he facilitated and for making my time in Karlsruhe unforgettable.

I want to express my gratitude to all the theoretical chemistry group members—past and present—who have supported me over these thrilling recent years. A friendlier and more accommodating work environment is difficult to imagine.

I would also want to thank all of my scientific collaborators, including Prof. Dr. Frank Breher, Prof. Dr. Markus Gerhards, Prof. Dr. Sabine Becker, Dr. Claudia Bizzarri, and their groups, for bringing my interests to the fascinating chemical challenges that are, in part, discussed in this work.

My mother, who has always loved and cared for me and serves as my ultimate role model, deserves a special thank you. I appreciate your continued faith in me!

For all his love and support throughout these trying years, I sincerely thank my loving husband Andreas.

Last but not least, I want to thank my brothers, and my sisters for their spiritual support while I was writing this thesis and living my life in general.

## 7 COPYRIGHT PERMISSIONS

A portion of the information presented in Chapter 4 has previously been published in journals that are reviewed by experts in the field. The copyright permits for published work are issued by the right owners, and the following is information regarding those licenses:

- The results, tables, and figures from the preceding section 4.1 have been republished in part with permission from the following sources:

- Wagner, H.E., Frank, N., Barani, E., Anson, C.E., Bayer, L., Powell, A.K., Fink, K. and Breher, F., 2022. Asymmetrically Difunctionalized 1, 1'-Ferrocenyl Metalloligands and Their Transition Metal Complexes. *European Journal of Inorganic Chemistry*, 2022(4), p.e202100898.

- The results, tables, and figures from the preceding section 4.2 have been republished in part with permission from the following sources:

- Gracia, L.L., Barani, E., Braun, J., Carter, A.B., Fuhr, O., Powell, A.K., Fink, K. and Bizzarri, C., Photocatalytic reduction of CO<sub>2</sub> by highly efficient homogeneous Fe<sup>II</sup> catalyst based on 2,6-bis(1',2',3'-triazolyl-methyl)pyridine. Comparison with analogues. *ChemCatChem*.

- The results, tables, and figures from the preceding section 4.3 have been republished in part with permission from the following sources:

- Petrikat, R.I., Steiger, S.T., Barani, E., Boden, P.J., Huber, M.E., Ringenberg, M., Niedner-Schatteburg, G., Fink, K. and Becker, S., 2023. Cooperativity-driven reactivity of a dinuclear copper dimethylglyoxime complex. *Chemistry–A European Journal*, p.e202203438.

## 8 LIST OF SCIENTIFIC PUBLICATIONS

- Wagner, H.E., Frank, N., Barani, E., Anson, C.E., Bayer, L., Powell, A.K., Fink, K. and Breher, F., 2022. Asymmetrically Difunctionalized 1, 1'-Ferrocenyl Metalloligands and Their Transition Metal Complexes. *European Journal of Inorganic Chemistry*, 2022(4), p.e202100898.  
DOI: [10.1002/ejic.202100898](https://doi.org/10.1002/ejic.202100898)
- Gracia, L.L., Barani, E., Braun, J., Carter, A.B., Fuhr, O., Powell, A.K., Fink, K. and Bizzarri, C., Photocatalytic reduction of CO<sub>2</sub> by highly efficient homogeneous Fe<sup>II</sup> catalyst based on 2,6-bis(1',2',3'-triazolyl-methyl)pyridine. Comparison with analogues. *ChemCatChem*, 2022.  
DOI: [10.1002/cctc.202201163](https://doi.org/10.1002/cctc.202201163)
- Petrikat, R.I., Steiger, S.T., Barani, E., Boden, P.J., Huber, M.E., Ringenberg, M., Niedner-Schatteburg, G., Fink, K. and Becker, S., 2023. Cooperativity-driven reactivity of a dinuclear copper dimethylglyoxime complex. *Chemistry–A European Journal*, p.e202203438.  
DOI: [10.1002/chem.202203438](https://doi.org/10.1002/chem.202203438)

## 9 LIST OF FIGURES

<b>Figure 4.1. 1</b> Overview about the employed catalyst models for 5D, proposed by Nils Frank. ...	30
<b>Figure 4.1. 2</b> Proposed mechanism by Breher et al., $\pm\text{Br}^-$ indicates the possibility binding of a bromide to the cationic complex.(Reused from <sup>80</sup> with permission) .....	33
<b>Figure 4.1. 3</b> Ionization potential (B3LYP) with respect to the calculated values for ferrocene (6.363 eV vertical and 6.228 eV adiabatic) .....	35
<b>Figure 4.1. 4</b> Spin density of vertical ionized <b>5A</b> , <b>5D</b> , and <b>6D</b> , basis set: def2-TZVP , isovalue= 0.01. lhs: B3LYP; rhs: BP86. Other hybrid functionals behave similar to B3LYP, other GGAs similar to BP86. ....	36
<b>Figure 4.1. 5</b> Gibbs free energy profile for a catalyst in oxidation states Ni(II)/Fe(II) and Ni(II)/Fe(III). All potentials include the energy of Mes-OMe and Mes-Br (one interacting with the catalyst, the other one infinitely separated) in order to limit changes in the interaction energy between substrate and catalyst. Separate species means that Mes-OMe and Mes-Br are both at infinite distance.....	42
<b>Figure 4.2. 1</b> (Left) Chemical structures of the Fe <sup>II</sup> and Co <sup>II</sup> complexes investigated as CO <sub>2</sub> reduction CAT. (Right) Synthetic pathways of the heteroleptic ( <b>1</b> and <b>2</b> ) and homoleptic ( <b>3</b> and <b>4</b> ) complexes in methanol at room temperature. ....	50
<b>Figure 4.2. 2</b> Mulliken spin populations on atoms for quintet (left), triplet (middle) and singlet states(right) of the dianion A <sup>2-</sup> of complex <b>1</b> , using r <sup>2</sup> SCAN-3c method.....	52
<b>Figure 4.2. 3</b> Spin density of Complex <b>1</b> (A) [FeL(NCS) <sub>2</sub> Py] <sup>0</sup> , quintet state and (B) [FeL(NCS) <sub>2</sub> Py] <sup>1-</sup> , sextet state, (C) [FeL(NCS) <sub>2</sub> Py] <sup>2-</sup> , triplet state. Basis set: def2-TZVP, functional: B3LYP; isovalue: $\pm 0.01$ .....	53

## List of figures

---

<b>Figure 4.2. 4</b> The relative energies of different oxidation states for (A) complex <b>1</b> , (B) complex <b>3</b> . Basis set: def2-TZVP; functional: B3LYP .....	55
<b>Figure 4.2. 5</b> Desorption of CO <sub>2</sub> in Oxidation states of 0 and 1- for (A) Complex <b>1</b> , and Oxidation states of 2+ and 1+ for (B) Complex <b>3</b> . Basis set: def2-TZVP; functional: B3LYP .....	56
<b>Figure 4.2. 6</b> Complex <b>1</b> : First step: Detachment of the pyridine ligand, Second step: Adsorption of CO <sub>2</sub> . Different oxidation states (x=0, -, 2-) of the complex are compared. Only for [FeL(NCS) <sub>2</sub> Py] <sup>2-</sup> , CO <sub>2</sub> could be adsorbed. For all attempts (different starting structures) to adsorb CO <sub>2</sub> for other oxidation states, CO <sub>2</sub> moved away. Basis set: def2-TZVP; functional: B3LYP ...	57
<b>Figure 4.2. 7</b> Binding energy of NCS on complex <b>1</b> (kJ/mol). Basis set: def2-TZVP, functional: B3LYP .....	58
<b>Figure 4.2. 8</b> Complex <b>3</b> : First step: Detachment of the triazole ligand, Second step: Adsorption of CO <sub>2</sub> . Different oxidation states (x=2+, 1+, 0) of the complex are compared. Only for [FeL <sub>2</sub> ] <sup>0</sup> CO <sub>2</sub> could be adsorbed. For all attempts (different starting structures) to adsorb CO <sub>2</sub> for other oxidation states, CO <sub>2</sub> moved away. Basis set: def2-TZVP; functional: B3LYP.....	59
<b>Figure 4.2. 9</b> Mode of coordination of CO <sub>2</sub> .....	59
<b>Figure 4.2. 10</b> Spin density of (A) Complex <b>1</b> , [FeL(NCS) <sub>2</sub> Py] <sup>2-</sup> , singlet state and (B) Complex <b>3</b> , [FeL <sub>2</sub> ] <sup>0</sup> , triplet state. S <sup>2</sup> for complex <b>1</b> : 1.2 and for complex <b>3</b> : 3.03. Basis set: def2-TZVP, functional: B3LYP; isovalue: ± 0.01 .....	61
<b>Figure 4.2. 11</b> Energy diagram for CAT <b>1</b> in different multiplicities.....	64
<b>Figure 4.2. 12</b> Energy diagram for CAT <b>3</b> for different multiplicities. ....	67
<b>Figure 4.2. 13</b> Proposed mechanism for the photocatalytic CO <sub>2</sub> reduction with complex <b>3</b> ; hydrogenation and reduction in the same step (lhs) and energy diagram for complex <b>3</b> in different multiplicities (rhs), using r <sup>2</sup> SCAN-3c method.....	67

## List of figures

---

<b>Figure 4.3. 1</b> Molecular structures of <b>1a</b> , <b>1b</b> , and <b>2</b> . <b>1a</b> : d(Cu-Cu): 3.293(8) Å, <b>1b</b> : 3.32(1) Å. Ellipsoids are set at the 50 % probability level. The counter ions of <b>1a</b> and <b>1b</b> are omitted for clarity. ....	72
<b>Figure 4.3. 2</b> Spin density for singlet states (left) and triplet states (right) of isomer A of <b>1</b> . Isovalue: $\pm 0.01$ , $S^2$ for singlet is 0.86 (indicating broken-spin solution), for triplet is 2.....	74
<b>Figure 4.3. 3</b> Molecular structures of isomer A (left) and B(right) of <b>1</b> after optimization. Bond lengths are in Å. Basis set: def2-TZVP; functional: B3LYP.....	75
<b>Figure 4.3. 4</b> UV/Vis spectra of <b>1</b> in methanol (left: $c = 3.56 \cdot 10^{-5}$ mol/L, right: $c = 1.94 \cdot 10^{-4}$ mol/L). ....	76
<b>Figure 4.3. 5</b> Comparison between Calculated UV/Vis spectrum (Cu(II)/Cu(II)) and the experimental spectrum of <b>1</b> .....	77
<b>Figure 4.3. 6</b> Calculated transition densities at 230 nm (A), 270 nm (B), 345 nm (C), and 490 nm (D) for <b>1</b> (Cu(II)/Cu(II)). Basis set: def2-TZVP; functional: B3LYP, isovalue: $\pm 0.05$ .....	78
<b>Figure 4.3. 7</b> Magnetic Susceptibility of triplet and singlet states of <b>1</b> with Magnetic field $B = 1.0$ .....	80
<b>Figure 4.3. 8</b> Splitting diagrams of the d levels in a square planar (left) and square pyramidal (right) ligand field. ....	83
<b>Figure 4.3. 9</b> Magnetic Susceptibility of triplet and singlet states with Magnetic field $B = 1.0$ , left: $\chi T$ ( $\text{cm}^3\text{K/mol}$ ), right: $\chi$ ( $\text{cm}^3/\text{mol}$ ).....	84
<b>Figure 4.3. 10</b> Mulliken charges of isomer A of <b>1</b> using B3LYP/def2-TZVP. ....	86
<b>Figure 4.3. 11</b> Mulliken charges of <b>2</b> using B3LYP/def2-TZVP.....	86
<b>Figure 4.3. 12</b> Proposed mechanism and energy diagram for isomer A of <b>1</b> using B3LYP/def2-TZVP.....	87

## List of figures

---

**Figure 4.3. 13** Calculated UV/Vis spectra for H<sub>2</sub>dmg and 2,3-butanedione monoxime..... 88

## 10 LIST OF TABLES

<b>Table 4.1. 1</b> Comparison of the vertical ionization potential and quasi particle energies of the highest Ni and Fe dominated orbital, respectively, for <b>5D</b> ( <b>5A</b> for comparison) and <b>6D</b> (def2-TZVP basis set). The Mulliken populations refer to the Ni and Fe contributions in the respective orbitals. ....	37
<b>Table 4.1. 2</b> Vertical and adiabatic IPs for different complexes and density functionals. Mulliken contributions of Ni and Fe to the spin density. Basis set: def2-TZVP .....	38
<b>Table 4.1. 3</b> IPs based on KS orbital energies and evGW quasi partical energies as well as Mulliken populations for the lowest orbitals of <b>5D</b> .....	39
<b>Table 4.1. 4</b> IPs based on KS orbital energies and evGW quasi partical energies as well as Mulliken populations for the lowest orbitals of <b>6D</b> .....	40
<b>Table 4.1. 5</b> IPs based on KS orbital energies and evGW quasi partical energies as well as Mulliken populations for the lowest orbitals of <b>5A</b> .....	41
<b>Table 4.1. 6</b> Electronic energies and thermodynamic properties for reductive elimination. ....	44
<b>Table 4.1. 7</b> Electronic energies and thermodynamic properties for oxidative addition. ....	45
<b>Table 4.1. 8</b> Electronic energies and thermodynamic properties for single species (used in calculation of the Gibbs free reaction energy above). ....	46
<b>Table 4.2. 1</b> Calculation of electronic energy (a.u.) and relative energy (kJ/mol) of linkage isomerism concerning spin states in complex <b>1</b> using r <sup>2</sup> SCAN-3c method. The initial structure is the dianion A <sup>2-</sup> .....	52
<b>Table 4.2. 2</b> Electronic energy (a.u.), Mulliken spin population and charges of different spin multiplicities for complex 1 and 3. Basis set: def2-TZVP; functional: B3LYP.....	54
<b>Table 4.2. 3</b> Redox Potentials of the catalysts and their reduction states reacting with CO <sub>2</sub> .....	56

## List of tables

---

<b>Table 4.2. 4</b> Binding energy of different ligands on complex <b>1</b> (kJ/mol). Basis set: def2-TZVP, functional: B3LYP .....	58
<b>Table 4.2. 5</b> Relative energy (kJ/mol) of different patterns for adsorption of CO <sub>2</sub> in different spin multiplicities, singlet and triplet for complex <b>1</b> and <b>3</b> . .....	60
<b>Table 4.2. 6</b> Mulliken charge and spin density of Fe and CO <sub>2</sub> ; Basis set: def2-TZVP; functional: B3LYP .....	62
<b>Table 4.2. 7</b> Desorption energies in kJ/mol for CO from CAT <b>1</b> and <b>3</b> . .....	64
<b>Table 4.2. 8</b> Electronic energy (a.u.) and relative energy (kJ/mol) for different reaction paths in different multiplicities using r <sup>2</sup> SCAN-3c method.....	68
<b>Table 4.3. 1</b> Electronic energy (a.u.) of different optimized structures for different multiplicities and functionals. Basis set: def2-TZVP. ....	73
<b>Table 4.3. 2</b> Electronic energy (a. u.) and relative energy (kJ/mol) for isomer A and B of <b>1</b> in different multiplicities using B3LYP/def2-TZVP. ....	75
<b>Table 4.3. 3</b> Energies (in cm <sup>-1</sup> ) of the lowest electronic states for <b>1</b> with inclusion of Spin–Orbit Coupling, CAS (18,10) SCF/CI.....	79
<b>Table 4.3. 4</b> g-tensors of the lowest states(triplet) for <b>1</b> with two ligands, spin S=1.0. In the figure directions show g-tensors, g1 (red), g2 (green) g3 (blue).....	79
<b>Table 4.3. 5</b> Energies (in cm <sup>-1</sup> ) of the lowest electronic states of <b>2</b> with and without ethanol and inclusion of Spin–Orbit Coupling, CAS (9,5) SCF/CI. ....	81
<b>Table 4.3. 6</b> g-tensors of the lowest Kramer’s doublet for <b>2</b> with and without ethanol, spin S=1/2. In the figure directions show g-tensors, g1 (red), g2 (green) g3 (blue) for <b>2</b> without ethanol (down) and <b>2</b> with ethanol (up). ....	81

## List of tables

---

**Table 4.3. 7** Energies (in  $\text{cm}^{-1}$ ) of the lowest electronic states for **1b** and isomer A with inclusion of Spin–Orbit Coupling, CAS (18,10) SCF/CI..... 82

**Table 4.3. 8** g-tensors of the lowest states (triplet) for isomer A and **1b**, spin  $S=1.0$ ..... 83

## 11 LIST OF SCHEMES

<b>Scheme 4.1. 1</b> Synthesis of the Pd, Cu and Ni complexes of the metalloligands <b>2A-D</b> . .....	31
<b>Scheme 4.1. 2</b> Synthesis of the methoxides <b>6A</b> , <b>6B</b> and <b>6D</b> . .....	32
<b>Scheme 4.2. 1</b> Proposed mechanism for the photocatalytic CO <sub>2</sub> reduction with <b>1</b> . .....	63
<b>Scheme 4.2. 2</b> Proposed mechanism for the photocatalytic CO <sub>2</sub> reduction with <b>3</b> . .....	66
<b>Scheme 4.3. 1</b> Structures of <b>1</b> and its two isomers A (left) and B (middle) and structure of <b>2</b> (right). Cation and coordinating ethanol solvent molecule not shown for clarity. The charge of isomer B as well as the positions of the protons are not clarified, depending on the deprotonation state, the charge can be 1+ or 2+. .....	71
<b>Scheme 4.3. 2</b> Postulated nucleophilic attack of H <sub>2</sub> O at the glyoxime carbon atom to form intermediate NH <sub>2</sub> OH and 2,3-butanedione monoxime ( <b>3</b> ). Subsequently and depending on the solvent, NH <sub>2</sub> OH will either be oxidized to N <sub>2</sub> O or be reduced to NH <sub>4</sub> <sup>+</sup> . .....	85

## 12 BIBLIOGRAPHY

1. Keim, W., *Die homogene Übergangsmetallkatalyse und ihre industrielle Anwendung*. Chem. Ind.(Düsseldorf), 1984. **107**: p. 397.
2. Maugh, T.H., *Homogeneous Catalysis: Ultimate Selectivity: By using single metal atoms in solution, it is often possible to carry out specific reactions to the exclusion of all others*. Science, 1983. **220**(4601): p. 1032-1035.
3. Styring, S., *Artificial photosynthesis for solar fuels*. Faraday discussions, 2012. **155**: p. 357-376.
4. Astruc, D., *Transition-metal nanoparticles in catalysis: from historical background to the state-of-the art*. Nanoparticles and catalysis, 2008. **1**: p. 1-48.
5. Kohn, W. and L.J. Sham, *Self-consistent equations including exchange and correlation effects*. Physical review, 1965. **140**(4A): p. A1133.
6. Perdew, J.P. and K. Schmidt, *Density functional theory and its application to materials*. Van Doren, V, 2001: p. 1-20.
7. Schultz, N.E., Y. Zhao, and D.G. Truhlar, *Density functionals for inorganometallic and organometallic chemistry*. The Journal of Physical Chemistry A, 2005. **109**(49): p. 11127-11143.
8. Niu, S. and M.B. Hall, *Theoretical studies on reactions of transition-metal complexes*. Chemical reviews, 2000. **100**(2): p. 353-406.
9. Sameera, W. and F. Maseras, *Transition metal catalysis by density functional theory and density functional theory/molecular mechanics*. WIREs Comput Mol Sci 2: 375–385. 2012.
10. Harvey, J.N., *On the accuracy of density functional theory in transition metal chemistry*. Annual Reports Section "C"(Physical Chemistry), 2006. **102**: p. 203-226.
11. Bursch, M., et al., *Best-Practice DFT Protocols for Basic Molecular Computational Chemistry*. Angewandte Chemie, 2022: p. e202205735.
12. Husch, T., A.C. Vaucher, and M. Reiher, *Semiempirical molecular orbital models based on the neglect of diatomic differential overlap approximation*. International journal of quantum chemistry, 2018. **118**(24): p. e25799.
13. Elstner, M. and G. Seifert, *Density functional tight binding*. Philosophical Transactions of the Royal Society A: Mathematical, Physical and Engineering Sciences, 2014. **372**(2011): p. 20120483.
14. Hohenberg, P. and W. Kohn, *Density functional theory (DFT)*. Phys. Rev, 1964. **136**: p. B864.
15. Perdew, J.P., et al., *Prescription for the design and selection of density functional approximations: More constraint satisfaction with fewer fits*. The Journal of chemical physics, 2005. **123**(6): p. 062201.
16. Kurth, S., J.P. Perdew, and P. Blaha, *Molecular and solid-state tests of density functional approximations: LSD, GGAs, and meta-GGAs*. International journal of quantum chemistry, 1999. **75**(4-5): p. 889-909.
17. Zhang, I.Y. and X. Xu, *On the top rung of Jacob's ladder of density functional theory: Toward resolving the dilemma of SIE and NCE*. Wiley Interdisciplinary Reviews: Computational Molecular Science, 2021. **11**(1): p. e1490.
18. Perdew, J.P., K. Burke, and M. Ernzerhof, *Generalized gradient approximation made simple*. Physical review letters, 1996. **77**(18): p. 3865.

## Bibliography

---

19. Tao, J., et al., *Climbing the density functional ladder: Nonempirical meta-generalized gradient approximation designed for molecules and solids*. Physical Review Letters, 2003. **91**(14): p. 146401.
20. Staroverov, V.N., et al., *Comparative assessment of a new nonempirical density functional: Molecules and hydrogen-bonded complexes*. The Journal of chemical physics, 2003. **119**(23): p. 12129-12137.
21. Becke, A.D., *A new mixing of Hartree-Fock and local density-functional theories*. The Journal of chemical physics, 1993. **98**(2): p. 1372-1377.
22. Stephens, P.J., et al., *Ab initio calculation of vibrational absorption and circular dichroism spectra using density functional force fields*. The Journal of physical chemistry, 1994. **98**(45): p. 11623-11627.
23. Ernzerhof, M. and G.E. Scuseria, *Assessment of the Perdew-Burke-Ernzerhof exchange-correlation functional*. The Journal of chemical physics, 1999. **110**(11): p. 5029-5036.
24. Grimme, S., et al., *r(2)SCAN-3c: A "Swiss army knife" composite electronic-structure method*. Journal of Chemical Physics, 2021. **154**(6).
25. Ehlert, S., et al., *r2SCAN-D4: Dispersion corrected meta-generalized gradient approximation for general chemical applications*. The Journal of Chemical Physics, 2021. **154**(6): p. 061101.
26. Kruse, H. and S. Grimme, *A geometrical correction for the inter-and intra-molecular basis set superposition error in Hartree-Fock and density functional theory calculations for large systems*. The Journal of chemical physics, 2012. **136**(15): p. 04B613.
27. Gasevic, T., et al., *Optimization of the r2SCAN-3c Composite Electronic-Structure Method for Use with Slater-Type Orbital Basis Sets*. The Journal of Physical Chemistry A, 2022.
28. Runge, E. and E.K. Gross, *Density-functional theory for time-dependent systems*. Physical review letters, 1984. **52**(12): p. 997.
29. Casida, M., et al., *Theoretical and Computational modeling of NLO and Electronic Materials*. Recent Advances in Density Functional Methods, 1996. **628**: p. 145.
30. Petersilka, M., U. Gossmann, and E. Gross, *Excitation energies from time-dependent density-functional theory*. Physical review letters, 1996. **76**(8): p. 1212.
31. Hedin, L., *New method for calculating the one-particle Green's function with application to the electron-gas problem*. Physical Review, 1965. **139**(3A): p. A796.
32. Hedin, L., *On correlation effects in electron spectroscopies and the GW approximation*. Journal of Physics: Condensed Matter, 1999. **11**(42): p. R489.
33. Aryasetiawan, F. and O. Gunnarsson, *The GW method*. Reports on Progress in Physics, 1998. **61**(3): p. 237.
34. van Setten, M.J., F. Weigend, and F. Evers, *The GW-method for quantum chemistry applications: Theory and implementation*. Journal of chemical theory and computation, 2013. **9**(1): p. 232-246.
35. Onida, G., L. Reining, and A. Rubio, *Electronic excitations: density-functional versus many-body Green's-function approaches*. Reviews of modern physics, 2002. **74**(2): p. 601.
36. Galitskii, V.M. and A.B. Migdal, *Application of quantum field theory methods to the many body problem*. Sov. Phys. JETP, 1958. **7**(96): p. 18.
37. Roos, B.O., P.R. Taylor, and P.E. Sigbahn, *A complete active space SCF method (CASSCF) using a density matrix formulated super-CI approach*. Chemical Physics, 1980. **48**(2): p. 157-173.

## Bibliography

---

38. Parlett, B.N., *The Rayleigh quotient iteration and some generalizations for nonnormal matrices*. Mathematics of Computation, 1974. **28**(127): p. 679-693.
39. Meier, U. and V. Staemmler, *An efficient first-order CASSCF method based on the renormalized Fock-operator technique*. Theoretica chimica acta, 1989. **76**(2): p. 95-111.
40. Maurice, R., et al., *Universal theoretical approach to extract anisotropic spin hamiltonians*. Journal of Chemical Theory and Computation, 2009. **5**(11): p. 2977-2984.
41. Taratiel, D., et al., *Magnetic coupling in oxalato-bridged hetero-bimetallic compounds: an ab initio study*. Polyhedron, 2003. **22**(14-17): p. 2409-2414.
42. Anderson, P.W., *Antiferromagnetism. Theory of superexchange interaction*. Physical Review, 1950. **79**(2): p. 350.
43. Szalay, P.G., et al., *Multiconfiguration self-consistent field and multireference configuration interaction methods and applications*. Chemical reviews, 2012. **112**(1): p. 108-181.
44. Fink, K., R. Fink, and V. Staemmler, *Ab initio calculation of the magnetic exchange coupling in linear oxo-bridged binuclear complexes of titanium (III), vanadium (III), and chromium (III)*. Inorganic Chemistry, 1994. **33**(26): p. 6219-6229.
45. Fink, K. and V. Staemmler, *A modified CAS-CI approach for an efficient calculation of magnetic exchange coupling constants*. Molecular Physics, 2013. **111**(16-17): p. 2594-2605.
46. Fink, K., C. Wang, and V. Staemmler, *Superexchange and Spin-Orbit Coupling in Chlorine-Bridged Binuclear Cobalt (II) Complexes*. Inorganic Chemistry, 1999. **38**(17): p. 3847-3856.
47. Bodenstern, T., et al., *Development and Application of a Complete Active Space Spin-Orbit Configuration Interaction Program Designed for Single Molecule Magnets*. ChemPhysChem, 2022. **23**(1): p. e202100648.
48. Augustine, R., et al., *Anchored homogeneous catalysts: high turnover number applications*. Journal of Molecular Catalysis A: Chemical, 2004. **216**(2): p. 189-197.
49. Rothenberg, G., *Catalysis: concepts and green applications*. 2017: John Wiley & Sons.
50. Berzelius, J., *Sur un force jusqu'ici peu remarqu e qui est probablement active dans la formation des compos es organiques, Section on Vegetable Chemistry*. Jahres-Bericht, 1835. **14**: p. 237.
51. Ostwald, W., *Referate Zeit*. Phys. Chem, 1894. **15**: p. 705-706.
52. Ittel, S.D., *Homogeneous catalysis: the applications and chemistry of catalysis by soluble transition metal complexes*. 1992: Wiley.
53. Misono, M. and N. Nojiri, *Recent progress in catalytic technology in Japan*. Applied catalysis, 1990. **64**: p. 1-30.
54. Pagire, S.K., N. Kumagai, and M. Shibasaki, *The Different Faces of [Ru (bpy) 3Cl2] and fac [Ir (ppy) 3] Photocatalysts: Redox Potential Controlled Synthesis of Sulfonylated Fluorenes and Pyrroloindoles from Unactivated Olefins and Sulfonyl Chlorides*. Organic Letters, 2020. **22**(20): p. 7853-7858.
55. Kang, D., et al., *Electrochemical synthesis of photoelectrodes and catalysts for use in solar water splitting*. Chemical reviews, 2015. **115**(23): p. 12839-12887.
56. Gao, C., et al., *Coordination chemistry in the design of heterogeneous photocatalysts*. Chemical Society Reviews, 2017. **46**(10): p. 2799-2823.
57. Zhang, B. and L. Sun, *Artificial photosynthesis: opportunities and challenges of molecular catalysts*. Chemical Society Reviews, 2019. **48**(7): p. 2216-2264.

## Bibliography

---

58. Kotrel, S. and S. Bräuninger, *Industrial electrocatalysis*. Handbook of Heterogeneous Catalysis: Online, 2008: p. 1936-1958.
59. Dau, H., et al., *ChemCatChem*, 2010, 2, 724–761;(b) V. Artero, M. Chavarot-Kerlidou and M. Fontecave. *Angew. Chem., Int. Ed*, 2011. **50**: p. 7238-7266.
60. Kinzel, N.W., C. Werlé, and W. Leitner, *Transition Metal Complexes as Catalysts for the Electroconversion of CO<sub>2</sub>: An Organometallic Perspective*. *Angewandte Chemie International Edition*, 2021. **60**(21): p. 11628-11686.
61. Roduner, E., *Selected fundamentals of catalysis and electrocatalysis in energy conversion reactions—a tutorial*. *Catalysis Today*, 2018. **309**: p. 263-268.
62. Savéant, J.-M. and C. Costentin, *Elements of Molecular and Biomolecular Electrochemistry: An Electrochemical Approach to Electron Transfer Chemistry*. 2019: John Wiley & Sons.
63. Zhang, B.A., C. Costentin, and D.G. Nocera, *Driving force dependence of inner-sphere electron transfer for the reduction of CO<sub>2</sub> on a gold electrode*. *The Journal of Chemical Physics*, 2020. **153**(9): p. 094701.
64. Kaeffer, N. and W. Leitner, *Electrocatalysis with Molecular Transition-Metal Complexes for Reductive Organic Synthesis*. *JACS Au*, 2022. **2**(6): p. 1266-1289.
65. Blanco, V., D.A. Leigh, and V. Marcos, *Artificial switchable catalysts*. *Chemical Society Reviews*, 2015. **44**(15): p. 5341-5370.
66. Wei, J. and P.L. Diaconescu, *Redox-switchable ring-opening polymerization with ferrocene derivatives*. *Accounts of Chemical Research*, 2019. **52**(2): p. 415-424.
67. Ryu, Y., G. Ahumada, and C.W. Bielawski, *Redox-and light-switchable N-heterocyclic carbenes: a “soup-to-nuts” course on contemporary structure–activity relationships*. *Chemical Communications*, 2019. **55**(31): p. 4451-4466.
68. Maity, R., et al., *Cooperative Effects in Multimetallic Complexes Applied in Catalysis*. *ChemCatChem*, 2021. **13**(10): p. 2337-2370.
69. Feyrer, A., et al., *Metal Complexes of a Redox-Active [1] Phosphaferrocenophane: Structures, Electrochemistry and Redox-Induced Catalysis*. *Chemistry—A European Journal*, 2017. **23**(31): p. 7402-7408.
70. Siemeling, U., *Singlet carbenes derived from ferrocene and closely related sandwich complexes*. *European Journal of Inorganic Chemistry*, 2012. **2012**(22): p. 3523-3536.
71. Bildstein, B., *Carbenes with ferrocenyl substituents*. *Journal of Organometallic Chemistry*, 2001. **617**: p. 28-38.
72. Lorkovic, I.M., R.R. Duff, and M.S. Wrighton, *Use of the Redox-Active Ligand 1,1'-Bis(diphenylphosphino)cobaltocene To Reversibly Alter the Rate of the Rhodium(I)-Catalyzed Reduction and Isomerization of Ketones and Alkenes*. *Journal of the American Chemical Society*, 1995. **117**(12): p. 3617-3618.
73. Braga, D., et al., *Novel hetero-bimetallic metalla-macrocycles based on the bis-1-pyridyl ferrocene [Fe( $\eta$ 5-C<sub>5</sub>H<sub>4</sub>-1-C<sub>5</sub>H<sub>4</sub>N)<sub>2</sub>] ligand. Design, synthesis and structural characterization of the complexes [Fe( $\eta$ 5-C<sub>5</sub>H<sub>4</sub>-1-C<sub>5</sub>H<sub>4</sub>N)<sub>2</sub>](Ag)<sup>2+</sup>/(Cu)<sup>2+</sup>/(Zn)<sup>2+</sup>*. *Chemical Communications*, 2002(10): p. 1080-1081.
74. Braga, D., et al., *Mechanically Induced Expeditious and Selective Preparation of Disubstituted Pyridine/Pyrimidine Ferrocenyl Complexes*. *Organometallics*, 2004. **23**(11): p. 2810-2812.
75. Braga, D., et al., *Novel Organometallic Building Blocks for Molecular Crystal Engineering. 2. Synthesis and Characterization of Pyridyl and Pyrimidyl Derivatives of*

## Bibliography

---

- Diboronic Acid, [Fe( $\eta^5$ -C<sub>5</sub>H<sub>4</sub>-B(OH)<sub>2</sub>)<sub>2</sub>], and of Pyridyl Boronic Acid, [Fe( $\eta^5$ -C<sub>5</sub>H<sub>4</sub>-4-C<sub>5</sub>H<sub>4</sub>N)( $\eta^5$ -C<sub>5</sub>H<sub>4</sub>-B(OH)<sub>2</sub>)].* Organometallics, 2003. **22**(10): p. 2142-2150.
76. Hua, D.H., et al., *Short syntheses of 8-substituted 8'-[1-(1'-phenylthio)ferrocenyl]-1,1'-binaphthyls from Suzuki coupling reactions. A strategy for generating new chiral ligands and charge-transfer complexes.* Journal of Organometallic Chemistry, 2001. **637-639**: p. 832-836.
77. Beagley, P., et al., *Synthesis and antiplasmodial activity in vitro of new ferrocene-chloroquine analogues.* Dalton Transactions, 2003(15): p. 3046-3051.
78. Balavoine, G.G.A., et al., *Selective synthesis of ferrocenes.* Journal of Organometallic Chemistry, 1998. **567**(1): p. 191-198.
79. Wagner, H.E., et al., *Asymmetrically Difunctionalized 1, 1'-Ferrocenyl Metalloligands and Their Transition Metal Complexes.* European Journal of Inorganic Chemistry, 2022.
80. Frank, N., *Quantenchemische Untersuchungen zur Veretherung von Arylhalogeniden an einem Nickelmodellkomplex, in Fakultät für Chemie und Biowissenschaften.* 2020, Karlsruher Institut für Technologie. p. 55.
81. Balasubramani, S.G., et al., *TURBOMOLE: Modular program suite for ab initio quantum-chemical and condensed-matter simulations.* J Chem Phys, 2020. **152**(18): p. 184107.
82. Plessow, P., *Reaction Path Optimization without NEB Springs or Interpolation Algorithms.* J Chem Theory Comput, 2013. **9**(3): p. 1305-10.
83. Helgaker, T., *Transition-State Optimizations by Trust-Region Image Minimization.* Chemical Physics Letters, 1991. **182**(5): p. 503-510.
84. Schautz, F., H.-J. Flad, and M. Dolg, *Quantum Monte Carlo study of Be<sub>2</sub> and group 12 dimers M<sub>2</sub> (M= Zn, Cd, Hg).* Theoretical Chemistry Accounts, 1998. **99**(4): p. 231-240.
85. Igel-Mann, G., H. Stoll, and H. Preuss, *Pseudopotentials for main group elements (IIIa through VIIa).* Molecular Physics, 1988. **65**(6): p. 1321-1328.
86. Schäfer, A., H. Horn, and R. Ahlrichs, *Fully optimized contracted Gaussian basis sets for atoms Li to Kr.* The Journal of Chemical Physics, 1992. **97**(4): p. 2571-2577.
87. Schäfer, A., C. Huber, and R. Ahlrichs, *Fully optimized contracted Gaussian basis sets of triple zeta valence quality for atoms Li to Kr.* The Journal of Chemical Physics, 1994. **100**(8): p. 5829-5835.
88. Grimme, S., et al., *A consistent and accurate ab initio parametrization of density functional dispersion correction (DFT-D) for the 94 elements H-Pu.* J Chem Phys, 2010. **132**(15): p. 154104.
89. S. Grimme, S.E.a.L.G., *Effect of the damping function in dispersion corrected density functional theory.* J. Comput. Chem., 2011(32): p. 1456-1465.
90. Becke, A.D., *Density-functional thermochemistry. III. The role of exact exchange.* The Journal of Chemical Physics, 1993. **98**(7): p. 5648-5652.
91. Becke, A.D., *Density-functional exchange-energy approximation with correct asymptotic behavior.* Phys Rev A Gen Phys, 1988. **38**(6): p. 3098-3100.
92. Terrett, J.A., et al., *Switching on elusive organometallic mechanisms with photoredox catalysis.* Nature, 2015. **524**(7565): p. 330-4.
93. Kaufmann, S., et al., *Rhodium (I) and Iridium (I) Complexes of Ferrocenyl-Functionalized Amidinates and Bis (amidinates):  $\kappa^2$  N-Coordination Versus Ferrocenyl Ortho-Metalation.* Organometallics, 2019. **38**(8): p. 1721-1732.
94. Kühn, M. and F. Weigend, *One-electron energies from the two-component GW method.* Journal of Chemical Theory and Computation, 2015. **11**(3): p. 969-979.

## Bibliography

---

95. Feyrer, A., et al., *Metal Complexes of a Redox-Active [1]Phosphaferrocenophane: Structures, Electrochemistry and Redox-Induced Catalysis*. Chemistry – A European Journal, 2017. **23**(31): p. 7402-7408.
96. Diccianni, J.B. and T. Diao, *Mechanisms of Nickel-Catalyzed Cross-Coupling Reactions*. Trends in Chemistry, 2019. **1**(9): p. 830-844.
97. Hayashida, T., et al., *Trifluoromethanesulfonate (triflate) as a moderately coordinating anion: Studies from chemistry of the cationic coordinatively unsaturated mono- and diruthenium amidinates*. Journal of Organometallic Chemistry, 2007. **692**(1-3): p. 382-394.
98. Dau, H., E. Fujita, and L. Sun, *Artificial Photosynthesis: Beyond Mimicking Nature*. ChemSusChem, 2017. **10**(22): p. 4228-4235.
99. Gust, D., *Chapter One - An Illustrative History of Artificial Photosynthesis*, in *Advances in Botanical Research*, B. Robert, Editor. 2016, Academic Press. p. 1-42.
100. Centi, G. and S. Perathoner, *Towards Solar Fuels from Water and CO<sub>2</sub>*. ChemSusChem, 2010. **3**(2): p. 195-208.
101. Whang, D.R. and D.H. Apaydin, *Artificial Photosynthesis: Learning from Nature*. ChemPhotoChem, 2018. **2**(3): p. 148-160.
102. Laitar, D.S., P. Müller, and J.P. Sadighi, *Efficient Homogeneous Catalysis in the Reduction of CO<sub>2</sub> to CO*. Journal of the American Chemical Society, 2005. **127**(49): p. 17196-17197.
103. Leung, C.-F. and T.-C. Lau, *Organic Photosensitizers for Catalytic Solar Fuel Generation*. Energy & Fuels, 2021. **35**(23): p. 18888-18899.
104. Jiang, C., A.W. Nichols, and C.W. Machan, *A look at periodic trends in d-block molecular electrocatalysts for CO<sub>2</sub> reduction*. Dalton Transactions, 2019. **48**(26): p. 9454-9468.
105. Takeda, H., et al., *Highly Efficient and Robust Photocatalytic Systems for CO<sub>2</sub> Reduction Consisting of a Cu(I) Photosensitizer and Mn(I) Catalysts*. Journal of the American Chemical Society, 2018. **140**(49): p. 17241-17254.
106. Chen, L., et al., *A molecular noble metal-free system for efficient visible light-driven reduction of CO<sub>2</sub> to CO*. Dalton Transactions, 2019. **48**(26): p. 9596-9602.
107. Feller, M., et al., *Reductive Cleavage of CO<sub>2</sub> by Metal–Ligand-Cooperation Mediated by an Iridium Pincer Complex*. Journal of the American Chemical Society, 2016. **138**(20): p. 6445-6454.
108. Windle, C.D. and R.N. Perutz, *Advances in molecular photocatalytic and electrocatalytic CO<sub>2</sub> reduction*. Coordination Chemistry Reviews, 2012. **256**(21): p. 2562-2570.
109. Lee, S.K., et al., *Function-Integrated Ru Catalyst for Photochemical CO<sub>2</sub> Reduction*. Journal of the American Chemical Society, 2018. **140**(49): p. 16899-16903.
110. Rønne, M.H., et al., *Ligand-Controlled Product Selectivity in Electrochemical Carbon Dioxide Reduction Using Manganese Bipyridine Catalysts*. Journal of the American Chemical Society, 2020. **142**(9): p. 4265-4275.
111. Chauhan, D.K., N. Sharma, and K. Kailasam, *A critical review on emerging photocatalysts for syngas generation via CO<sub>2</sub> reduction under aqueous media: a sustainable paradigm*. Materials Advances, 2022. **3**(13): p. 5274-5298.
112. Ghenai, C., *Combustion of Syngas Fuel in Gas Turbine Can Combustor*. Advances in Mechanical Engineering, 2010. **2**: p. 342357.
113. Foit, S.R., et al., *Power-to-Syngas: An Enabling Technology for the Transition of the Energy System?* Angewandte Chemie International Edition, 2017. **56**(20): p. 5402-5411.

## Bibliography

---

114. Rao, H., J. Bonin, and M. Robert, *Visible-light Homogeneous Photocatalytic Conversion of CO<sub>2</sub> into CO in Aqueous Solutions with an Iron Catalyst*. *ChemSusChem*, 2017. **10**(22): p. 4447-4450.
115. Zhang, X., et al., *Photochemical CO<sub>2</sub> Reduction Driven by Water-Soluble Copper(I) Photosensitizer with the Catalysis Accelerated by Multi-Electron Chargeable Cobalt Porphyrin*. *ACS Catalysis*, 2019. **9**(12): p. 11263-11273.
116. Wang, Y., et al., *Water-Assisted Highly Efficient Photocatalytic Reduction of CO<sub>2</sub> to CO with Noble Metal-Free Bis(terpyridine)iron(II) Complexes and an Organic Photosensitizer*. *Inorganic Chemistry*, 2021. **60**(8): p. 5590-5597.
117. Rosas-Hernández, A., et al., *Earth-abundant photocatalytic systems for the visible-light-driven reduction of CO<sub>2</sub> to CO*. *Green Chemistry*, 2017. **19**(10): p. 2356-2360.
118. *Handbook of Chemistry and physics - Abundance of elements in the earth's crust and in the sea*.
119. Cuttell, D.G., et al., *Simple Cu(I) Complexes with Unprecedented Excited-State Lifetimes*. *Journal of the American Chemical Society*, 2002. **124**(1): p. 6-7.
120. Becke, A., *Density-functional thermochemistry. III. The role of exact exchange (1993)* *J. Chem. Phys.* **98**: p. 5648.
121. Caldeweyher, E., et al., *A generally applicable atomic-charge dependent London dispersion correction*. *The Journal of chemical physics*, 2019. **150**(15): p. 154122.
122. Weigend, F. and R. Ahlrichs, *Balanced basis sets of split valence, triple zeta valence and quadruple zeta valence quality for H to Rn: Design and assessment of accuracy*. *Physical Chemistry Chemical Physics*, 2005. **7**(18): p. 3297-3305.
123. Frank, N., *The ORCA program system*. *Wiley Interdiscip Rev Comput Mol Sci*, 2012. **2**: p. 73-78.
124. Neese, F., *Software update: The ORCA program system—Version 5.0*. *Wiley Interdisciplinary Reviews: Computational Molecular Science*, 2017: p. e1606.
125. Burmeister, J.L. and F. Basolo, *Inorganic linkage isomerism of the thiocyanate ion*. *Inorganic Chemistry*, 1964. **3**(11): p. 1587-1593.
126. Masdeu-Bultó, A.M., M. Reguero, and C. Claver, *Mechanistic Insights of Photocatalytic CO<sub>2</sub> Reduction: Experimental versus Computational Studies*. *European Journal of Inorganic Chemistry*, 2022: p. e202100975.
127. Dai, G. and J. Liu, *Fe-quaterpyridine complex: a comprehensive DFT study on the mechanism of CO<sub>2</sub>-to-CO conversion*. *Journal of Materials Science*, 2020. **55**(29): p. 14301-14314.
128. Straub, S., et al., *An Iron Complex with a Bent, O-Coordinated CO<sub>2</sub> Ligand Discovered by Femtosecond Mid-Infrared Spectroscopy*. *Angew Chem Int Ed Engl*, 2018. **57**(18): p. 5000-5005.
129. Straub, S. and P. Vohringer, *Spin-Controlled Binding of Carbon Dioxide by an Iron Center: Insights from Ultrafast Mid-Infrared Spectroscopy*. *Angew Chem Int Ed Engl*, 2021. **60**(5): p. 2519-2525.
130. Chapovetsky, A., et al., *Pendant hydrogen-bond donors in cobalt catalysts independently enhance CO<sub>2</sub> reduction*. *ACS central science*, 2018. **4**(3): p. 397-404.
131. Frenking, G., et al., *Metal–CO bonding in mononuclear transition metal carbonyl complexes*. *JACS Au*, 2021. **1**(5): p. 623-645.

## Bibliography

---

132. Loipersberger, M., et al., *Mechanistic insights into Co and Fe quaterpyridine-based CO<sub>2</sub> reduction catalysts: Metal–ligand orbital interaction as the key driving force for distinct pathways*. Journal of the American Chemical Society, 2021. **143**(2): p. 744-763.
133. Sträter, N., et al., *Two-metal ion catalysis in enzymatic Acyl- and phosphoryl-transfer reactions*. Angewandte Chemie International Edition in English, 1996. **35**(18): p. 2024-2055.
134. Bosnich, B., *Cooperative bimetallic redox reactivity*. Inorganic Chemistry, 1999. **38**(11): p. 2554-2562.
135. van der Vlugt, J.I., *Cooperative catalysis with first-row late transition metals*. European Journal of Inorganic Chemistry, 2012. **2012**(3): p. 363-375.
136. Buchwalter, P., J. Rose, and P. Braunstein, *Multimetallic catalysis based on heterometallic complexes and clusters*. Chemical reviews, 2015. **115**(1): p. 28-126.
137. Tebben, L., et al., *From Additivity to Cooperativity in Chemistry: Can Cooperativity Be Measured?* Chemistry—A European Journal, 2017. **23**(25): p. 5864-5873.
138. Prosenc, M.H., M.M. Kappes, and G. Niedner-Schatteburg, *Cooperative Effects in Heterometallic Complexes*. 2021, Wiley Online Library. p. 15019-15020.
139. Wall, T., et al., *Quantification of Cooperativity between Metal Sites in Dinuclear Transition Metal Complexes Containing the (2-Dimethylamino)-4-(2-pyrimidinyl) pyrimidine Ligand*. ChemPlusChem, 2021. **86**(4): p. 622-628.
140. Grupe, M., et al., *Time-Resolved Spectroscopy and Electronic Structure of Mono- and Dinuclear Pyridyl-Triazole/DPEPhos-Based Cu (I) Complexes*. Chemistry—A European Journal, 2021. **27**(61): p. 15252-15271.
141. *Transregional collaborative research center located at the TU Kaiserslautern (TUK) and Karlsruhe Institute of Technology (KIT), 2009-2022*.
142. Frasson, E., R. Bardi, and S. Bezzi, *Structure of copper-dimethylglyoxime at low temperature*. Acta Crystallographica, 1959. **12**(3): p. 201-205.
143. Svedung, D., *The crystal structure of copper dimethylglyoxime dichloride*. Acta Chem. Scand, 1969. **23**: p. 2865-2878.
144. Petrikat, R.I. and S. Becker, *BF<sub>4</sub><sup>-</sup> as source for the preparation of BF<sub>2</sub> bridged copper (II) dimethylglyoxime complexes*. Zeitschrift für anorganische und allgemeine Chemie, 2022. **648**(16): p. e202200150.
145. Ruiz, R., et al., *Oximate complexes. Part I. Solution study, synthesis, structure, spectroscopic and magnetic properties of polynuclear copper (II) complexes containing dimethylglyoxime*. Journal of the Chemical Society, Dalton Transactions, 1993(10): p. 1623-1628.
146. Chen, X.-Y., et al., *Binuclear and tetranuclear copper (II) complexes bridged by dimethylglyoxime*. Chemistry letters, 2003. **32**(2): p. 118-119.
147. Li, C.-H., et al., *Unexpected assembly of a tetranuclear copper (II) complex bridged by glyoximate groups*. Inorganic Chemistry Communications, 2002. **5**(6): p. 403-406.
148. Panja, P.K., et al., *Infrared spectroscopic studies of dimethylglyoxime chelates of nickel, cobalt, copper, palladium and platinum*. Journal of molecular structure, 1991. **249**(2-4): p. 277-283.
149. Caton Jr, J.E. and C.V. Banks, *Studies of the spectra of copper dimethyl-glyoxime, nickel dimethylglyoxime and nickel ethylmethylglyoxime in various solvents*. Talanta, 1966. **13**(7): p. 967-977.

## Bibliography

---

150. Falk, K.E., et al., *Electron paramagnetic resonance study of copper (II) dimethylglyoxime. I. Theoretical and experimental study of the effect of axial ligands*. Inorganic Chemistry, 1970. **9**(3): p. 556-562.
151. Wu, X. and W. Hu, *Copper-catalyzed N-Arylation of Imidazoles with Aryl or Heteroaryl Halides Facilitated by Dimethylglyoxime in Water*. Chinese Journal of Chemistry, 2011. **29**(10): p. 2124-2128.
152. Xavier, K., J. Chacko, and K.M. Yusuff, *Zeolite-encapsulated Co (II), Ni (II) and Cu (II) complexes as catalysts for partial oxidation of benzyl alcohol and ethylbenzene*. Applied Catalysis A: General, 2004. **258**(2): p. 251-259.
153. Gawlig, C., S. Schindler, and S. Becker, *One-Pot Conversion of Cyclohexane to Adipic Acid Using a  $\mu$ 4-Oxido-Copper Cluster as Catalyst Together with Hydrogen Peroxide*. European Journal of Inorganic Chemistry, 2020. **2020**(3): p. 248-252.
154. Ahlrichs, R., et al., *TURBOMOLE V7. 5 2020, a development of University of Karlsruhe and Forschungszentrum Karlsruhe GmbH, 1989–2007, TURBOMOLE GmbH, since 2007; available from*
  
155. Whitten, J.L., *Coulombic potential energy integrals and approximations*. The Journal of Chemical Physics, 1973. **58**(10): p. 4496-4501.
156. Baerends, E., D. Ellis, and P. Ros, *Self-consistent molecular Hartree—Fock—Slater calculations I. The computational procedure*. Chemical Physics, 1973. **2**(1): p. 41-51.
157. Heinze, H.H., A. Görling, and N. Rösch, *An efficient method for calculating molecular excitation energies by time-dependent density-functional theory*. The Journal of Chemical Physics, 2000. **113**(6): p. 2088-2099.
158. *Software developed in Kaiserslautern and Karlsruhe in the collaborative research center TRR88 '3MET'*.
159. Neese, F., *Efficient and accurate approximations to the molecular spin-orbit coupling operator and their use in molecular g-tensor calculations*. The Journal of chemical physics, 2005. **122**(3): p. 034107.
160. Helmich-Paris, B., C. Hattig, and C. van Wüllen, *Spin-free CC2 implementation of induced transitions between singlet ground and triplet excited states*. Journal of Chemical Theory and Computation, 2016. **12**(4): p. 1892-1904.
161. Gerloch, M. and R.F. McMeeking, *Paramagnetic properties of unsymmetrical transition-metal complexes*. Journal of the Chemical Society, Dalton Transactions, 1975(22): p. 2443-2451.
162. Rzepa, H.S. *Oxime formation from hydroxylamine and ketone: a (computational) reality check on stage one of the mechanism*. 2012 [cited 2022; Available from: <https://www.ch.imperial.ac.uk/rzepa/blog/?p=7779>].
163. Agmon, N., *The grotthuss mechanism*. Chemical Physics Letters, 1995. **244**(5-6): p. 456-462.